DEVELOPMENT OF GRAPHITIC CARBON NITRIDE BASED ASSEMBLIES FOR SUNLIGHT DRIVEN PHOTOCATALYSIS

By

HAK CHEN HONG

A dissertation submitted to the Department of Environmental Engineering
Faculty of Engineering and Green Technology
Universiti Tunku Abdul Rahman,
in partial fulfillment of the requirements for the degree of
Master of Engineering Science
October 2018

ABSTRACT

DEVELOPMENT OF GRAPHITIC CARBON NITRIDE BASED ASSEMBLIES FOR SUNLIGHT DRIVEN PHOTOCATALYSIS

Hak Chen Hong

This present work focused on the development of binary graphitic carbon nitride (g-C_3N_4) composite for sunlight driven photocatalysis. In the 1st project, the binary composite was achieved by doping noble metals such as gold (Au), silver (Ag) and palladium (Pd) with g-C_3N_4 through sunlight photodeposition. The deposition of Ag nanoparticles (NPs) (7.5 nm) resulted in the degradation of Bisphenol A (BPA) which was 2.15 fold higher than that of g-C_3N_4. For 2nd project, carbon dots (CDs) were successfully derived from water hyacinth leaves and the binary composite was achieved by incorporating CDs with g-C_3N_4 through hydrothermal treatment. The average particle size of CDs was found to be 3.1 nm and a blue-green fluorescence was emitted under the UV light irradiation. Both of 20CDs/g-C_3N_4 and 40CDs/g-C_3N_4 achieved the highest degradation efficiency of 2,4-dichlorophenol (2,4-DCP) with 1.7 times higher than that of pure g-C_3N_4. Both projects successfully improved the properties of g-C_3N_4 by elongating the lifetime of photogenerated electrons and widening the visible light response. The M/g-C_3N_4 (M=Au, Ag and Pd) in 1st project fully degraded BPA within 70 min while CDs/g-C_3N_4 (2nd project) degraded 94% of 2,4-DCP within 120 min. Despite of higher photocatalytic efficiency in the 1st project, CDs/g-C_3N_4 was recommended for further exploration from the aspect of low production cost and high sustainability.

ACKNOWLEDGEMENT

I would like to express my appreciations to everyone who had contributed to the successful completion of this project. I would thank my research supervisor, Dr. Sim Lan Ching. She is a great mentor who gave me lots of freedom to work on the study in my way and fully committed whenever I need his guidance and supports on paper writing and experimental works. I appreciate your positive problem solving skills, clear minded and open minded for giving me chances to attend international conference in Kuala Lumpur. I wish her all the best and may her blossom in where she is planted. Next, I would like to express my gratitude to my co-supervisor, Dr. Leong Kah Hon for his support and encouragements.

I would also like to thanks to lab assistants, Cik Noor Hazreena Binti Noor Izahar, Mr. Voon Kah Loon, Ms. Ng Suk Ting and Mr. Chin Kah Seng for providing technical and administrative supports throughout the project. Special thanks are given to all of my labmates and friends: Wong Kok Ann, Lim Ping Feng, Chin Ying Hui, Tai Jun Yan, Wong Jin Ling and Khor Jia Min who make my life enjoyable in laboratory.

Lastly, I would like to deliver the most important appreciation to my loving parents who support me during the research period. Sincerest thanks to my girlfriend, Ghee Li Ching for your unconditional love and cares gave me strength to continue this journey. Appreciate all people that helping me finish the project and accomplish my master.

APPROVAL SHEET

This dissertation entitled "**DEVELOPMENT OF GRAPHITIC CARBON NITRIDE BASED ASSEMBLIES FOR SUNLIGHT DRIVEN PHOTOCATALYSIS**" was prepared by HAK CHEN HONG and submitted as partial fulfillment of the requirements for the degree of Master of Engineering Science at Universiti Tunku Abdul Rahman.

Approved by:

(Dr. SIM LAN CHING) Date:
Supervisor
Department of Chemical Engineering
Lee Kong Chian Faculty of Engineering and Science
Universiti Tunku Abdul Rahman

(Dr. LEONG KAH HON) Date:
Co-supervisor
Department of Environmental Engineering
Faculty of Engineering and Green Technology
Universiti Tunku Abdul Rahman

FACULTY OF ENGINEERING AND GREEN TECHNOLOGY

UNIVERSITI TUNKU ABDUL RAHMAN

Date:

SUBMISSION OF DISSERTATION

It is hereby certified that **Hak Chen Hong** (ID No: **16AGM06578**) has completed this dissertation entitled "DEVELOPMENT OF GRAPHITIC CARBON NITRIDE BASED ASSEMBLIES FOR SUNLIGHT DRIVEN PHOTOCATALYSIS" under the supervision of Dr. Sim Lan Ching (Supervisor) from the Department of Chemical Engineering, Lee Kong Chian Faculty of Engineering and Science, and Dr. Leong Kah Hon (Co-Supervisor) from the Department of Environmental Engineering, Faculty of Engineering and Green Technology.

I understand that University will upload softcopy of my dissertation in pdf format into UTAR Institutional Repository, which may be made accessible to UTAR community and public.

Yours truly,

____
(Hak Chen Hong)

DECLARATION

I hereby declare that the dissertation is based on my original work except for citations and quotations which have been duly acknowledged. I also declare that it has not been previously or concurrently submitted for any other degree at UTAR or other institutions.

____

(HAK CHEN HONG)

Date ____________________

TABLE OF CONTENTS

Page

CHAPTER

LIST OF TABLES

LIST OF FIGURES

LIST OF SYMBOLS AND ABBREVIATIONS

Symbols/Abbreviation	**Meanings**
$^{\bullet}O_2^{-}$	Superoxide Radical
$^{\bullet}OH$	Hydroxyl Radical
2,4-DCP	2,4-dicholorophenol
Ag	Silver
AOP	Advanced Oxidation Process
Au	Gold
BPA	Bisphenol A
CB	Conduction Band
CDs	Carbon Dots
CO_2	Carbon Dioxide
e^-	Electron
EDCs	Endocrine Disrupting Compounds
Eg	Band Gap Energy
g-C_3N_4	Graphitic Carbon Nitride
H_2O	Water
H_2O_2	Hydrogen Peroxide
hv	Photons
LSPR	Localized Surface Plasmon Resonance
NHE	Normal Hydrogen Electrode
NIR	Near Infrared
NP	Nonylphenol
NPs	Nanoparticles
O_2	Oxygen
O_3	Ozone

Pd	Palladium
PPCPs	Pharmaceuticals and Personal Care Products
ReOH	Resorcinol
SC	Semiconductor
TiO_2	Titanium Dioxide
UCPL	Upconverted Photoluminescence
UV	Ultraviolet
VB	Valence Band
WH	Water Hyacinth
h^+	Holes

CHAPTER 1

INTRODUCTION

1.1 Background of Research

With the betterment of technology, quick growth of industry and rise in population, the environment pollution caused by organic pollutant is considering as a significant problem for the global. Endocrine disrupting chemicals (EDCs) are kind of organic pollutants that have the ability to interfere with natural hormonal mechanisms and modify the role of the endocrine system, thus significantly affect health in a living being (Sin et al., 2012). Some of the EDCs have the ability to mimic oestrogens also known as xenoestrogen, such as resorcinol (ReOH), 2,4-dichlorophenol (2,4-DCP) and bisphenol A (BPA) (Coleman et al., 2005). BPA is widely utilized as a monomeric material for the fabrication of epoxy-phenolic resins and polycarbonate and as antioxidant or a stabilizer for numerous types of plastics such as polyvinyl chloride (Imai et al., 2007).

EDCs are extremely resistant to degradation due to its high degree of chemical and biological stability properties (Kamaz, 2017). Consequently, direct discharge of EDCs into water sources will be harmful to the aquatic life, humans, animals and whole ecosystems. Human direct expose to EDCs through food ingestion, skin contact, inhalation of dust and smoke in leading interruption of hormone secretion, cancer development, metabolism, and infertility (Soto and Sonnenschein, 2010; Yeung et al., 2011). There are numerous inventions treatment technologies have been sped up to distinctive degrees of success, for example the membrane filtration, reverse osmosis, adsorption, biological reactions, coagulation, sedimentation, chemical processes and ion exchange (Lam et al., 2016). However, these traditional treatment methods are non-devastating and simply turn the pollutant to another stage, producing secondary pollutant and requiring further treatment (Rosenfeldt and Linden, 2004).

Photocatalysis is a classification of advanced oxidation process (AOPs) has go through a noteworthy development since the first revelation of photocatalytic water splitting with titanium dioxide (TiO_2) electrodes by Fujishima and Honda (Fujishima and Honda, 1972). Extensive researches have undergone to comprehend the principles of photocatalysis and enhance the photocatalytic performance. Photocatalysis is categorized into homogeneous and heterogeneous photocatalysis according to the different phases of reactants and photocatalysts employed. Semiconductor is commonly used in heterogeneous photocatalysis to mediate the photoreaction between the reactant and charge transfer due to their special electronic structure. Their structure consists of a filled valence band (VB) and an empty conduction band (CB). An electron (e^-) will excite from the VB to the CB, leaving a hole (h^+) in the VB when a photon strikes the photocatalyst with energy greater than band gap energy (E_g) of photocatalyst (Colmenares and Luque, 2014). The photogenerated charges will reduce oxygen (O_2) to form superoxide radicals anion ($^\bullet O_2^-$) and the holes will oxidize water (H_2O) to form hydroxyl radicals ($^\bullet OH$) as shown in Figure 1.1. These strong oxidizing agents ($^\bullet O_2^-$ and $^\bullet OH$) will further oxidize the organic substances to almost water and carbon dioxide

(CO_2) which are almost harmless to environment (Gupta et al., 2007). The photoactivity occurs when oxidation-reduction reactions are triggered by the generated charges at the surface of the photocatalyst, producing strong radicals like superoxide radical anions ($^{\bullet}O_2^{-}$) and hydroxyl radicals ($^{\bullet}OH$). Nevertheless, the photocatalysis is usually confined by its rapid recombination rate of photogenerated electron and hole pairs since the excited electron tends to recombine with holes, leading to low photocatalytic efficiency (Ong et al., 2016).

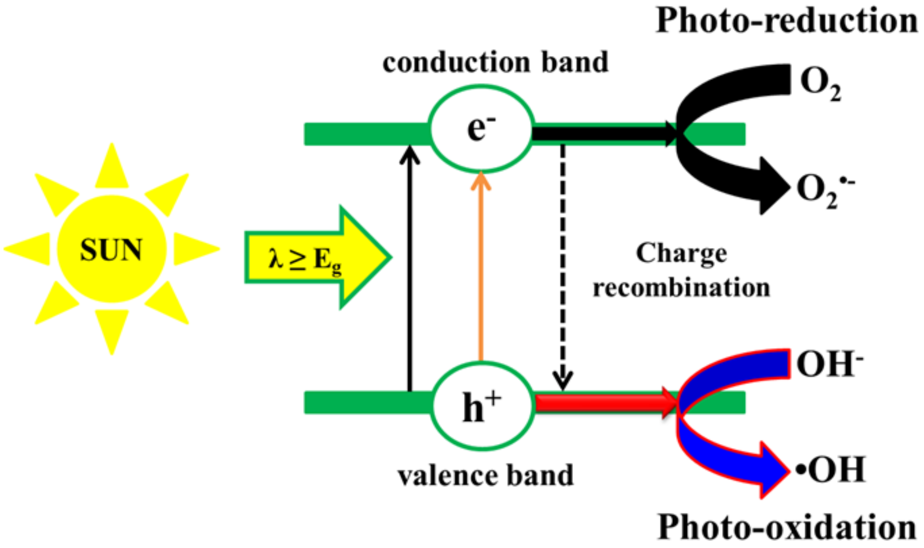

Figure 1.1: Electronic Structure of Photocatalyst (Colmenares and Luque, 2014)

Heterogeneous photocatalysis is an environment friendly and low cost approach for water splitting or water remediation under natural sunlight radiation. Natural sunlight which is abundant and sustainable can be used as energy input to drive heterogeneous photocatalysis. The sun transmits about 3×10^{24} J/year of energy to the earth surface which is approximately 104 times higher than the annual energy demand for the humans globally (Malekshoar, 2016). Photocatalyst can operate under ambient pressure and temperature, thus low operational cost is required for initiation. The used photocatalyst can be recycled and reused where no secondary disposal treatment is required (Bagheri and Julkapli, 2016). Another advantage of heterogeneous photocatalysis over other AOPs such as electrochemical oxidation, Fenton process, ozonation is that oxygen is used as oxidant instead of strong oxidants such as ozone (O_3) and hydrogen peroxide (H_2O_2).

In the exploration for powerful and stable visible light responded semiconductor photocatalysts, graphitic carbon nitride (g-C_3N_4), a polymeric semiconductor newly engrossed tremendous attention due to its attractive physicochemical properties (Yang et al., 2013). The g-C_3N_4 possesses unique properties like electronic and optical versatility, tribological and catalytic properties, high chemical and thermal stability, water resistivity, biocompatibility, super hardness and low density (Yan et al., 2012; Dong et al., 2014). In addition, g-C_3N_4 is the most sustainable and environmental friendly inorganic semiconductor compare to others due to it made up of carbon (C) and nitrogen (N) which are the most plentiful elements in our earth (Liu et al., 2016). The g-C_3N_4 has similar two-dimensional (2D) π-conjugated planar layers like graphite, which makes it retain a very high thermal and chemical stability (He, 2015). The π conjugated structure has an excellent electronic conductivity property which assists to enhance the electron transfer processes (Lam et al., 2016).

The g-C_3N_4 had been proved effective in photodegradation of a numerous of organic pollutants under visible light irradiation. The narrower band gap of g-C_3N_4 (2.7eV) enables its harvesting properties in visible wavelengths. Furthermore, the preparation method of g-C_3N_4 is very simple which is by thermal condensation of single source nitrogen-rich precursors such as urea, melamine, cyanamide or dicyandiamide (Sun et al., 2016). Recently, urea had being a low cost, non-toxic and common precursor in chemical industry and ends up being the promising starting material for producing g-C_3N_4. These outstanding features of g-C_3N_4 make it become a promising possibility for visible light enhancement.

1.2 Problem Statements

Bulk g-C_3N_4 suffers from limitations such as small specific surface area and rapid recombination rate of photoexcited electron-hole pairs (Mamba and Mishra 2016). Even though g-C_3N_4 has band gap of 2.7 eV which can absorb visible region (<460 nm) to perform photoactivity, the photocatalytic efficiency is still low because of the poor separation of electron-hole pairs (Pawar et al., 2015a). Thus, it is essential to develop g-C_3N_4 based composite which can suppress the recombination of electrons-hole pairs. Numerous approaches are available to increase the performance of g-C_3N_4, such as metal or non-metal doping (Liang et al., 2015; Chang et al., 2014; Liu et al., 2010; Leong et al., 2015a), coupling with other semiconductors (Ge et al., 2011a; Fagan et al., 2016) and carbon materials (Liu et al., 2016; Yuan et al., 2015). Among these attempts, doping with a noble metal is identified as one of the most promising alternatives to suppress the photoinduced charge carrier recombination as it acts as trapping sites for electrons (Fu et al., 2015; Pawar et al., 2015a). Recently, doping the noble metal nanoparticles (NPs) onto the surface of g-C_3N_4 such as gold (Au) (Tonda et al., 2016; Xie et al., 2016), palladium (Pd) (Konda et al., 2016), and silver (Ag) (Yang et al., 2013; Zhang et al., 2016; Li et al., 2015) become a promising strategy to minimize the electron loss and extend the visible-light response range.

It is well known that noble metals such as Au and Ag NPs can highly respond to visible light due to the localized surface plasmon resonance (LSPR) that arises from the resonant photo-induced coherent oscillation of charge (Ge et al., 2011b). Furthermore, the mixing semiconductor-metal is usually used to form a space-charge separation state (Schottky barrier). At the edge of two components, electrons transmit from one component to another to align the Fermi energy level thus improving the electron-hole pair's separation and boosting the photocatalysis efficiency. However, most of the researches focused on utilizing harmful ultraviolet (UV) light to drive the photodeposition of noble metal onto the surface of g-C_3N_4. Since the successful findings by Leong et al. (2014), limited attempts have been performed using natural sunlight to deposit the noble metals onto the surface of g-C_3N_4. Collectively all the stated problems above, prompt us to utilize natural sunlight as energy source from synthesis route to application to promote green energy and sustainability.

Compared to high cost noble metal NPs, carbon dots (CDs) may also act as the electron transfer/reservoir due to the conjugated π structure and considerable lower cost. Besides, CDs will act as light absorbers when coupled with other photocatalysts such as g-C_3N_4 (Ge et al., 2012), Bi_2WO_6 (Qian et al., 2016), TiO_2 (Yu et al., 2014), the upconverted photoluminescence (UCPL) properties of CDs enable it absorb a longer wavelength in visible light and then emit a shorter wavelength ultraviolet light (Li et al., 2010). Consequently, CDs can broaden the light absorption range of the photocatalysts and excite more charges and thus enhance the photocatalysis efficiency. Therefore, it is believed that the sunlight driven degradation of EDCs using CDs is achievable. In addition, CDs coupled with semiconductors like g-C_3N_4 to reinforce its nanostructure can overcome its high solubility problem. CDs are hydrophilic substances which are highly soluble in aqueous medium. Hence, it is hard to detach the CDs from the treated water and leading to secondary pollution.

It is always exciting to discover the green starting materials for CDs because these are easily accessible, inexpensive, non-toxic and clean. Recently, some achievements have been accomplished by utilizing natural green sources as CDs precursor, such as aloe (Xu et al., 2015), pericarp (Du et al., 2015), orange juice (Sahu et al., 2012), egg shell (Bhaisare et al., 2015) and plant leaves (Zhu et al., 2013) and sugarcane juice (Sim et al., 2018). In this study, water hyacinth (WH) is chosen as the green source to synthesize CDs using hydrothermal carbonization. WH is widespread on freshwater wetlands that available all year round and it can be easily obtained in local pond and river. According to past study, WH was native from Brazil but it has diffused to all subtropical and tropical nations around the world now, and it is considered as the largest invasive aquatic plants due to the reproduces pattern, since it can multiplies its size rapidly and forms dense mats (Keller and Lodge, 2009). WH populations have large negative impacts on human society by clogging waterways, wiping out aquatic flora and fauna and forming ideal prerequisite for diseases grow which eventually exacerbating vector-borne diseases (Kushwaha, 2012). Furthermore, WH also causes important ecological and socio-economic effects (Villamagna and Murphy, 2010) and it is considered as one of the world's most damaging and costly species. Thus, converting WH into valuable CDs can reduce the negative impacts on environment and become a sustainable and low cost precursor. To the best of our knowledge, there is no attempt using WH as precursor to synthesis CDs.

1.3 Objectives and Scopes of Research

This research aims to modify g-C_3N_4 with various noble metals and carbon dots to achieve sunlight-driven photocatalysis. All of the photodegradation experiments were performed under full sunlight illumination and applied for the degradation of BPA and 2,4-DCP from aqueous solution as contaminated water treatment. This research significantly contributes to a new development of composite photocatalysts that endorsed the sustainability in environmental applications. This project embarks on the following objectives:

1. To develop sunlight-responsive g-C_3N_4 based photocatalysts through the modification with different noble metals (Pd, Ag and Au) and CDs.
2. To produce CDs from water hyacinth (WH) via a green and versatile route.
3. To investigate the physicochemical properties of synthesized photocatalysts using various spectroscopic and microscopic techniques.
4. To evaluate the application of M/g-C_3N_4 (M=Pd, Ag and Au) and CDs/g-C_3N_4 for photocatalytic degradation of BPA and 2,4-DCP, respectively under irradiation of sunlight.
5. To determine the sustainability of M/g-C_3N_4 (M=Pd, Ag and Au) and CDs/g-C_3N_4 by production cost estimation.

1.4 Thesis Overview

Chapter 1 begins with the introduction on environmental pollution issues which is the main subject of present thesis. This is followed by an introductory note on photocatalysis and g-C_3N_4 photocatalyst. Afterward the major limitations of these specific studies were indicated and the precise objectives were established.

Chapter 2 outlines the literature study relevant to the thesis. In general, the chapter explains the foundation of semiconductor photocatalysis, different reports on modification approach and lastly the photocatalytic performance for degradation of organic pollutants.

Chapter 3 provides the detailed synthesis route for g-C_3N_4, followed by modification methods using noble metals (Ag, Au, Pd) and carbon dots (CDs). The synthesis is followed by the characterization techniques that are involved in understanding the physicochemical nature of the prepared samples. The last section of this chapter elaborates the experimental setup and conditions adopted for the degradation of organic pollutants.

Chapter 4 presents the outcome of the thesis findings with comprehensive discussion. The physicochemical properties of synthesized photocatalysts were deeply discussed in the chapter. Furthermore, the photocatalytic performance of organic pollutant degradation and its mechanism of synthesized composites were also presented in the chapter. The conclusions and recommendations are included in **Chapter 5**.

CHAPTER 2

LITERATURE REVIEW

2.1 Endocrine-Disrupting Compounds (EDCs) Contamination

These days, the water pollution becomes more serious owing to the excessive industrialization and increasing of population. Water treatment technology has become a popular topic in research in order to solve the water pollution issues. Compare to industrial discharges, wastewater produced from the human daily activities (domestic wastewater) caused higher impacts to the water source. This is because the discharge limit of industries had strictly controlled by Environmental Quality Act 1974 in Malaysia. According to Snyder (2003), traditional wastewater treatment cannot completely remove the pollutants like EDCs, pharmaceuticals and personal care products (PPCPs) in wastewater. PPCPs, a classification of EDCs, are metabolites and transformation products of food supplements, pharmaceutical drugs, ingredients in cosmetics and other personal care products (Esplugas et al., 2007). EDCs will affect human health by interfering with the synthesis and metabolism of endogenous hormones. On the other hand, the potential dangerous effects of EDCs on human health are cancer development, long-term effect on metabolism, immune system weaknesses, reduced fertility and dysfunction of reproductive system. A lot of studies proved that advanced oxidation process (AOPs) is a promising treatment method which can fully degrade the EDCs (Wang and Chu, 2016).

2.2 Advanced Oxidation Processes (AOPs)

AOPs use oxidizing agents like hydrogen peroxide (H_2O_2) and ozone (O_3) to generate $^{\bullet}OH$, to apply in biological treatment for degradation of toxic pollutants (Andreozzi et al., 1999; Hilles et al., 2019). AOPs generate hydroxyl radicals ($^{\bullet}OH$) *via* combination of oxidizing agents, irradiation and radiolysis. $^{\bullet}OH$ has high standard potential (2.38 eV vs. NHE) in acidic media and its high reactivity allow $^{\bullet}OH$ to mineralize the pollutants to carbon dioxide (CO_2), water and organic substances which boost its biodegradability in aqueous solution (Wang and Xu, 2012). There are many types of AOPs such as Fenton process, photo-assisted Fenton process, electro-Fenton, sono-Fenton, photocatalysis, and ozone water system. Table 2.1 shows the EDCs degradation efficiency by using different types of AOPs. Overall, the AOPs exhibited superior degradation efficiency of EDCs compared to that of conventional wastewater treatment.

Table 2.1: Advantage of Different Treatment Methods Applied to EDCs

Types of EDCs Removal	Method description	Advantages	References
BPA	Photocatalysis with TiO_2	Achieved 99.7% removal of BPA after 60 min.	Guo et al., 2009
2,4-DCP	Fenton/ UV	Degradation of 2,4-Dichorophenol up to 90%, mineralized to CO_2	Sabhi and Kiwi, 2001
Phthalic acid esters (PAEs) and BPA	Fenton treatment	Removal efficiencies of BPA and PAEs were more than 88%.	He et al., 2009
4-n-NP	Ultrasound	The degradation rate of NP in alkaline pH solution was faster.	Gultekin et al., 2009
Caffeine PPCPs and EDCs	Ozonation	Removed over 80% of caffeine, PPCPs and EDCs compound.	Broséus et al., 2009
BPA	Oxidized using H_2O_2–UV	Removal efficiency improved by adding H_2O_2	Chen et al., 2006

2.3 Heterogeneous Photocatalysis

Photocatalysis is a classification of advanced oxidation process (AOPs) that are occurred and accelerated by a light activated catalyst (Malekshoar, 2016). There are two categories of photocatalysis namely homogeneous and heterogeneous photocatalysis. Homogeneous photocatalysis has the photocatalysts and the reactants exist in the similar stage while heterogeneous photocatalysis has the photocatalyst in a different stage with the reactants (Gonzalez, 2015). Commonly, heterogeneous photocatalysts are semiconductors which have unique characteristics. The heterogeneous photocatalysis is activated by the photoexcitation of a semiconductor upon light illumination where the electron and hole are generated and captured by reactant species on the surface to perform the secondary reactions.

Heterogeneous photocatalysis is a branch of knowledge which involved a vast range of reactions: photoreduction, water detoxification, disinfection, water splitting, hydrogen transfer, organic synthesis, metal deposition, deuterium–alkane isotopic exchange, anti-cancer therapy, gaseous pollutant removal and etc. (Gaya and Abdullah, 2008). In recent decades, major attentive areas of heterogeneous photocatalysis obtained are carbon dioxide (CO_2) reduction, water splitting (hydrogen generation) and organic pollutants degradation either by using artificial or natural light.

A photocatalyst is characterized by its ability to perform the oxidation and reduction by efficient absorption of electromagnetic radiation (light) more than its band gap energy ($h\nu \geq E_g$). Semiconductors have a relatively small band gap (1 ~ 4 eV) than insulator which allows the electrons to be excited from VB to CB. Figure 2.1 shows the electronic band structure of different photocatalysts (Cu_2O, NiO, SnO_2, TiO_2, ZnO, C_3N_4 and etc) with the standard potentials of water redox reaction (Li and Wu, 2015). Redox reactions on the surface of semiconductor involve two types of electron transfer processes which are oxidation and reduction that are also known as interfacial charge transfer. This interfacial charge transfer rate highly depends on the energy levels between the semiconductor and the adsorbed species. The energy level of CB has to be less positive than the reduction potential of absorbed species in order to reduce the absorbed, whereas the energy levels of VB need to be less negative than the oxidation potential of adsorbed donor in order to oxidize the absorbed (Malekshoar, 2016).

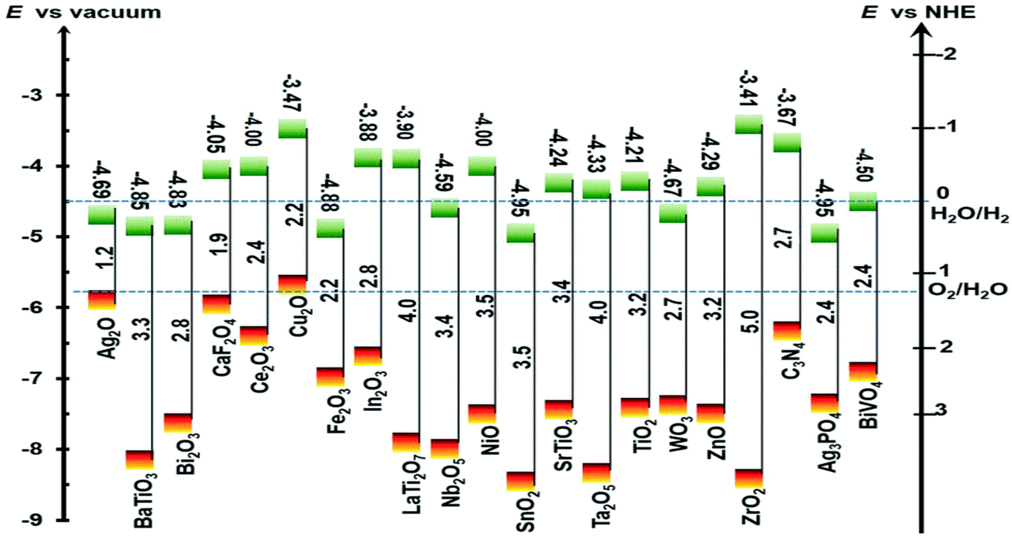

Figure 2.1: Electronic Band Structure of Different Semiconductor and Relative Band Edge Position to Electrochemical Scale (Li and Wu, 2015)

Figure 2.2 shows the mechanism of semiconductor (SC) photocatalysis. When the SC is stroked by photons (hν) with the energy equivalent or higher than the band gap energy (E_g), the electron (e^-) is excited from VB into CB remaining a hole (h^+) in VB (Equation 2.1). The electrons and holes will diffuse to the surface of SC (pathways C and D) in order to reduce and oxidize the reactants (A and D) as shown in Equation 2.2 and 2.3 (Linsebigler et al., 1995). However, electron-hole pairs tend to recombine instead of separating (Malekshoar, 2016). Electrons will reduce their potential energy while the holes will raise their potential energy via surface recombination and volume recombination (pathways A and B). The recombination of electron-hole pairs will release the absorbed light energy as heat (Linsebigler et al., 1995). In order to achieve higher efficiency of photoactivity, the recombination process should be suppressed.

$$\mathrm{SC} + h\nu\ (\geq E_g) \rightarrow e^- + h^+ \tag{2.1}$$

$$e^- + A \rightarrow A^{\bullet -} \tag{2.2}$$

$$h^+ + D \rightarrow D^{\bullet +} \tag{2.3}$$

where D is “reductant” (electron donor), and A is “oxidant” (electron acceptor).

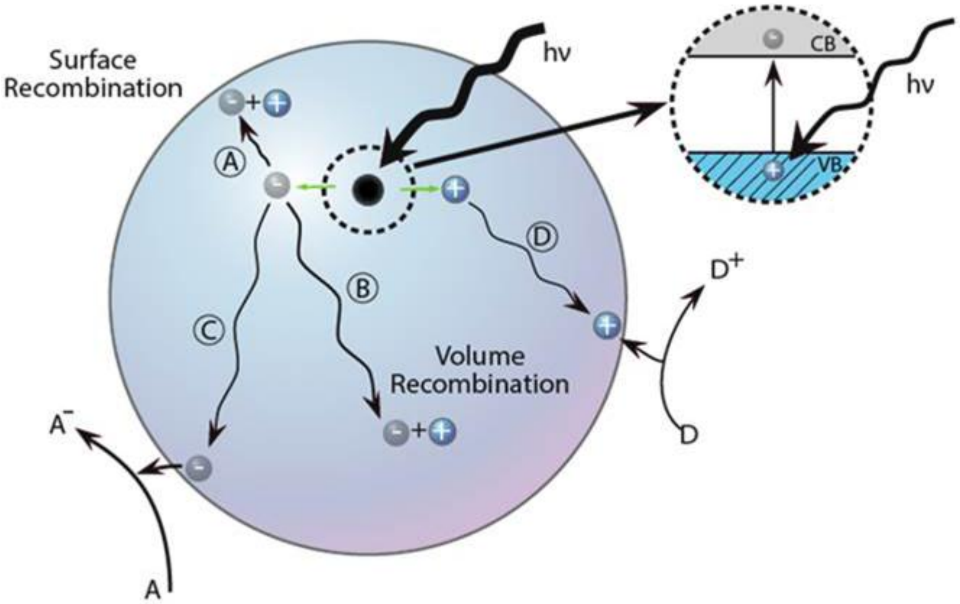

Figure 2.2: Different Pathways for Photogenerated Charges (Linsebigler et al., 1995)

2.4 Graphitic Carbon Nitride (g-C_3N_4)

Recently, a polymeric semiconductor, graphitic carbon nitride (g-C_3N_4) has become famous among the semiconductor photocatalyst. The g-C_3N_4 possesses attractive properties such as reliable thermal and chemical stability, water resistivity, biocompatibility, super hardness and low density (Dong et al., 2014). This makes it become a promising material for photocatalysis. The g-C_3N_4 has a band gap of 2.7 eV which enable it to perform catalytic reaction under visible light (Lam et al., 2016). Moreover, band positions of VB and CB of g-C_3N_4 are approximately 1.4 eV and -1.3 eV, respectively. This allows simultaneous reduction of protons (E_{NHE} (H^+/H_2) = 0.0 eV) and oxidation of water (E_{NHE} (O_2/H_2O) = 1.23 eV) (Li and Wu, 2015).

Furthermore, g-C_3N_4 can be synthesis by a simple polymerization of low-cost precursor like cyanamide, urea, melamine and etc. (He, 2015). Among these precursors, urea is the most favorable because it is an abundant, non-toxic, environment-friendly and low-cost raw precursor for the synthesis of g-C_3N_4. A simple thermal treatment is favorably adopted over other method to synthesize a large scale of g-C_3N_4 because urea is an active molecular precursor for thermal process (Liu et al., 2011). Dong et al, (2013) stated that the surface area of g-C_3N_4 increased with the heating time using urea as precursor (Table 2.2). As illustrated in Figure 2.3, the urea will decompose into isocyanic acid and ammonia when it is heated under a closed air atmosphere. It will then transform into other intermediates such as ammelide, ammeline and cyanuric acid (Schaber et al., 2004). The formation of cyanuric acid will further convert into melamine which then condenses to form melem. The melem will polymerize into melon and lastly the melon turn into g-C_3N_4 (Xu et al., 2013).

Table 2.2: Band Gap and Surface Area of g-C_3N_4 under Different Synthetic Conditions

Precursors	**Condition**	**Band Gap (eV)**	**Surfaca area (m^2/g)**	**References**
Cyanamide	550 °C, 4 h	2.70	ca. 10	Maeda et al., 2009
Melamine	500 °C, 2 h	2.80	ca. 8	Yan et al., 2009
	580 °C, 2 h	2.75	-	
Dicyandiamide	550 °C, 2 h	2.75	ca. 10	Zhang et al., 2012
Thiourea	450 °C, 2 h	2.71	ca. 11	Zhang et al., 2012
	500 °C, 2 h	2.70	ca. 17	
	550 °C, 2 h	2.58	ca. 18	
	600 °C, 2 h	2.62	ca. 27	
	650 °C, 2 h	2.76	ca. 52	
Urea	450 °C, 2 h	2.79	ca. 43	Zhang et al., 2012
	500 °C, 2 h	2.70	ca. 49	
	550 °C, 2 h	2.66	ca. 58	
	600 °C, 2 h	2.67	ca. 77	
	650 °C, 2 h	2.69	ca. 97	
	550 °C, 0 h	2.72	ca. 31	Dong et al., 2013
	550 °C, 1 h	2.68	ca. 62	
	550 °C, 2 h	2.72	ca. 75	
	550 °C, 4 h	2.78	ca. 288	

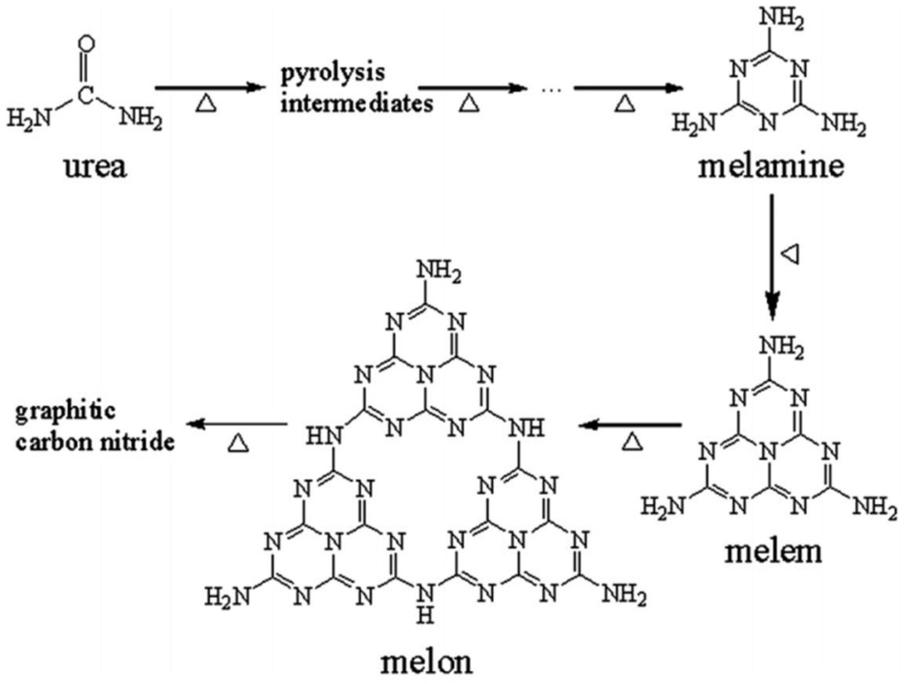

Figure 2.3: The Formation Mechanism of g-C_3N_4 by Pyrolysis of Urea (Xu et al., 2013)

However, bulk g-C_3N_4 suffer from fast recombination of photogenerated electron-hole pairs due to low charge mobility and slow electron transfer aroused from the weak interaction between neighboring planes, resulting in the poor photocatalytic performance (Pawar et al., 2015a; Gao et al., 2015). A number of approaches are available to improve the performance of g-C_3N_4, such as non-metal/metal doping, combination with other semiconductors (Tonda et al., 2016) and incorporation of carbon materials such as graphene, graphene quantum dots and carbon dots. Among these attempts, doping with a noble metal is identified as one of the most promising alternatives to further improve the visible light properties of g-C_3N_4 and suppress the photoinduced charge carrier recombination. This is attributable to the localized surface plasmon resonance (LSPR) effect of noble metal NPs (Au, Ag and Pd) and also acts as trapping sites for the electrons (Fu et al., 2015). Besides, incorporating carbon dots into g-C_3N_4 could be an alternative way to improve photocatalytic performance of g-C_3N_4. Carbon dots can be produced easily from various bioprecursors such as orange pericarp, lemon peel, leaves, urine and hair which are low cost and environment friendly.

2.5 Surface Plasmon Resonance (SPR)

Plasmons can be explained as an oscillation of fixed positive ions and free electron density in a metal as shown in Figure 2.4. Plasma oscillation occurs when an external electric field applied to a metal, the loosely bound electronic cloud will polarize to the downside and the positive ions will polarize to opposite side result in charge separation (Sun et al., 2016). If the electric field is cancelled, the electrons will move to the upside, repelled and attracted by each other to the positive ions on the downside. The electron and positive ions oscillate at the plasma frequency until the energy is lost due to resistance or damping (Jana et al., 2016). Plasmons are a quantization of this plasma oscillation. Plasmonics is the study of the interaction between free electrons and electromagnetic field in a metal (Malekzad et al., 2018). The electric component of light (photon) can stimulate the free electrons in the metal to have collective oscillations. However, loss is unavoidable for the plasmon oscillation due to the electron-core interactions and Ohmic loss (Maier, 2007).

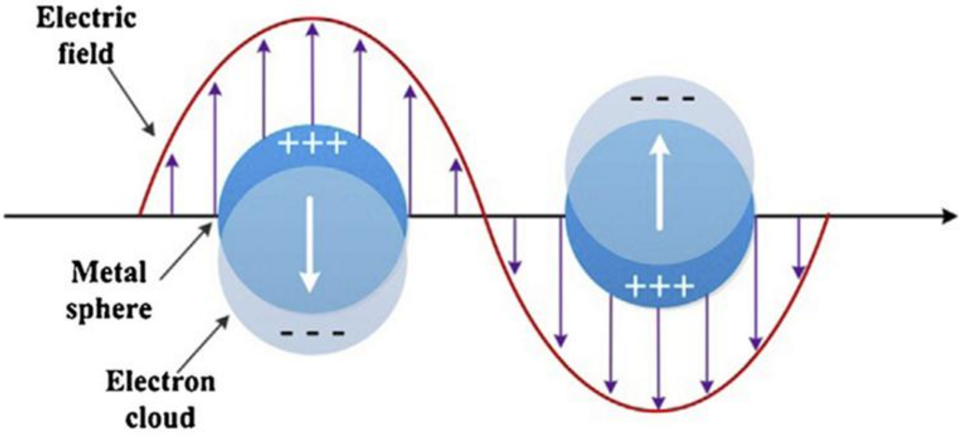

Figure 2.4: Illustration of Plasma Oscillation (Willets and Van Duyne, 2007)

SPR is a collective resonance oscillation of surface charge density which excited by incident light and propagates at the interface between dielectric medium and metal (Hma Salah, 2015). When the frequency of incident photons adapts the natural frequency of surface electrons, it will create the resonance oscillation condition (Lang et al., 2014). Meantime, the oscillation of the electron is against the restoring force of positive nuclei (Ong et al., 2016). The oscillation frequency and light absorption band are sensitive to the shape, size, and nanostructure of the metal (Xie et al., 2016).

2.6 Noble Metal Nanoparticles (NPs)

Noble metals are a group of metals including osmium (Os), ruthenium (Ru), palladium (Pd), rhodium (Rh), silver (Ag), platinum (Pt), gold (Au) and iridium (Ir) which are highly withstood to corrosion and oxidation in moist air (Daghrir et al., 2013). Noble metal NPs possess intensive absorption of visible light due to SPR effect characterized by strong field enhancement at the interface (Kvítek et al., 2013). The noble metal can improve the electron-hole pair separation as it acts as trapping sites for electrons and efficiently inhibit the fast recombination of electron-hole pairs (Pawar et al., 2015b). Moreover, the noble metals NPs are able to absorb a huge amount of light energy through SPR effect and release low amount of heat energy to the surrounding environment. Hence, the plasmon absorption may cause fast heating of noble metal NPs (Chen, 2010).

Recently, due to the inherent plasmonic phenomenon of noble metal NPs, many researchers attentive on the hybridization of g-C_3N_4 and noble metal NPs to boost the photoactivity performance. Noble metal NPs such as Ag and Au can intensely absorb visible light owing to their localized surface plasmon resonance (LSPR) phenomenon that arises from the resonant photo-induced coherent oscillation of surface charge and they can broaden the light absorption range of photocatalyst (Zhao et al., 2016; Xie et al., 2016; Samanta et al., 2014; Tonda et al., 2016). LSPR is collective electron oscillations in metallic NPs that are stimulated by the electromagnetic field of the incident light with certain natural frequency (Chen, 2014). This LSPR phenomenon led the conduction of electrons on the noble metal NPs to obtain energy from the incident light's wavelength and achieved high energy charges at the surface. This enables activating chemical reactions on the surface of noble metal NPs and enables the reactant molecules to interact with the NPs efficiently. The superiority of this phenomenon is to lower down the energy loss caused by the electron transferring or transmitting. Moreover, the intensity of LSPR is highly influenced by the particle size, interparticle interactions, morphology and local dielectric environment of noble metals (Sun et al., 2016).

Although Au NPs is comparatively expensive, still a lot of researches carried out the study because of its unique physiochemical properties such as surface carrier capabilities, amphilicity, and biocompatibility (Pawar et al., 2015a). Xie and co-worker (Xie et al., 2016) found that the Au NPs deposited on the surface of g-C_3N_4 exhibited broader of visible light response ranging from 400 to 640 nm. Tonda and co-worker (Tonda et al., 2016) reported that hybrids of Au and mp-g-C_3N_4 nanosheets exhibited a strong absorption edge in the visible range due to the LSPR effect of Au NPs. Furthermore, Kenens and co-worker (Kenens et al., 2016) reported the doping of Au NPs onto the surface of TiO_2 with improved photodegradation efficiency under sunlight irradiation. Besides that, the characteristic of Ag was also vastly investigated by the researchers because its costs are lower than other noble metals. Ag NPs with particle sizes of 5~20 nm supported on g-C_3N_4 nanosheet exhibited 95% degradation of Rhodamine B (RhB) which was 33% higher than that of g-C_3N_4 under visible-light irradiation (Li et al., 2015). Leong and co-worker deposited Pd NPs onto the surface of TiO_2 with particle sizes ranging from 17 to 29 nm. The obtained photocatalysts successfully improved light absorption in the visible region through LSPR of Pd NPs (Leong et al., 2015a).

The plasmonic photocatalyst is the hybridization of noble metal NPs and semiconductor. Noble metal NPs serve as a thermal redox active center, visible light absorber and charge-carrier traps to suppress the recombination of electron carriers (Patnaik et al., 2018). Considering the merit of noble metal NPs, it is expected that loading noble metal NPs with semiconductor g-C_3N_4 can further improve the photocatalytic performance. Furthermore, there is limited research study on the use of different noble metal such as Ag, Au and Pd doped with g-C_3N_4 to compare their photocatalytic performance. The major findings of noble metal and g-C_3N_4 combinations are detailed in Table 2.3.

Table 2.3: Compilation of Selected Literature Reports on g-C_3N_4 and Noble Metals

Type of Noble Metals	Preparation Method & Finding Remarks	References
Au	Au NPs deposited on g-C_3N_4 photocatalyst by a facile deposition–precipitation method. 1 wt% Au-loaded g-C_3N_4 exhibited high photocatalytic activity for hydrogen gas production under visible-light irradiation which was 23 times greater than g-C_3N_4.	Samanta et al., 2014
	A template-free in situ photo-reduction method was used to decorate Au NPs onto (mesoporous) mp-g-C_3N_4. The prepared Au/mp-g-C_3N_4 exhibited a strong absorption edge in visible and near-IR region owing to the LSPR effect of Au NPs. The Au/mp-g-C_3N_4 achieved the photocatalytic degradation of rhodamine B (RhB) almost 6 times higher than that of g-C_3N_4 under sunlight irradiation.	Tonda et al., 2016
	The photocatalyst Au/g-C_3N_4 was synthesized by a facile photoassisted reduction process. Au/g-C_3N_4 showed broader visible light response ranging from 400 to 640 nm and exhibited improvement in hydrogen evolution which was 130 times faster than that of g-C_3N_4.	Xie et al., 2016
	Au NPs were loaded on g-C_3N_4 nanosheets through visible light photoreduction of Au(III). The composites showed excellent photocatalytic performance for the degradation of methyl orange (MO) under visible-light irradiation which was 4.3 folds higher than that of g-C_3N_4.	Cheng et al., 2013
	Au–CNx composite was synthesized *via* the ultrasonication of carbon nitride quantum dots and $HAuCl_4$ without adding any reducing agent. The particle sizes of Au NPs ranged from 1 to 3 nm. The Au–CNx composite is a good adsorbent and very efficient towards the degradation of various dyes. The MB dye was degraded 96% in 120 minutes under visible light.	Bhowmik et al., 2015
	Au nanoparticles with average particle size 2.6 nm were successful doped on g-C_3N_4 sheets. Photocatalysis was driven by visible light irradiation for the reduction of p-nitrophenol to p-aminophenol. The rate constant of Au/g-C_3N_4-6 was 157 times higher than that of g-C_3N_4. The improved photocatalytic activity of Au/g-C_3N_4 was ascribed to the negative shift in Fermi level of Au caused by the induced charge-transfer effect arising from the strong interaction between Au NPs and g-C_3N_4.	Fu et al., 2017

Table 2.3, continued

Type of Noble Metals	Preparation Method & Finding Remarks	Reference
Ag	$g\text{-}C_3N_4$ was loaded with Ag NPs via a facile heating method. The Ag/$g\text{-}C_3N_4$ composites showed improved photocatalytic activity for the degradation of MO and hydrogen production compared to that of bulk $g\text{-}C_3N_4$. The enhanced photocatalytic performance was attributed to the synergic effect between Ag and $g\text{-}C_3N_4$, which stimulated the transfer efficiency of photogenerated electron-hole pairs.	Ge et al., 2011b
	Ag/$g\text{-}C_3N_4$ was prepared via a facile one-step route. The Ag NPs with average size of 5.6 nm was evenly distributed on the surface of $g\text{-}C_3N_4$. The smaller size and high dispersity of Ag NPs lead to strong LSPR effect and significantly improved the photocatalytic performance of the composites.	Fu et al., 2015
	Ag NPs were deposited on the surface of $g\text{-}C_3N_4$ by chemical reduction method to increase visible-light absorption via the LSPR effect, leading to the enhanced separation rate of photoexcited electron-holes pairs and promoted higher photocatalytic efficiency.	Qin et al., 2016
	A wet-chemical pathway in the presence of polyvinylpyrrolidone (PVP) was adopted to deposit Ag NPs onto $g\text{-}C_3N_4$ sheet. Ag/$g\text{-}C_3N_4$ showed advanced photoactivity under visible light irradiation compared to that of pure $g\text{-}C_3N_4$. The photocatalytic activity improved because the Ag particles act as surface plasmon to extend light absorption range and the Ag NPs also trapped electrons to reduce the recombination of photoexcited electron-hole pairs.	Lü et al., 2014
	Ag NPs were synthesized and immobilized during the synthesis of $g\text{-}C_3N_4$ nanosheets ($g\text{-}C_3N_4$-NS). The photodegradation of RhB under visible-light irradiation indicated that the degradation rate of 2% Ag/$g\text{-}C_3N_4$-NS was 8.5 times higher than $g\text{-}C_3N_4$-NS. This proved that the LSPR of Ag NPs could effectively promote the separation efficiency of photogenerated electron-hole pairs on the surface of $g\text{-}C_3N_4$-NS.	Jin et al., 2017
	Ag NPs were deposited onto the surface of $g\text{-}C_3N_4$ *via* photodeposition method. The MO and p-nitrophenol (PNP) was adopted as model pollutant to evaluate the photocatalytic activity of Ag/$g\text{-}C_3N_4$ under visible-light irradiation. The photocatalytic performance of Ag/$g\text{-}C_3N_4$ was higher than $g\text{-}C_3N_4$. This is owing to the SPR absorption of Ag NPs that efficiently utilized visible-light as well as fast generation, separation and transportation of the photogenerated carriers.	Yang et al., 2013

Table 2.3, continued

Type of Noble Metals	Preparation Method & Finding Remarks	Reference
Ag	Ag/g-C_3N_4 composites were synthesized using photodeposition, deposition-precipitation, and doping methods. Among the different synthesis method, the highest photoactivity was achieved by Ag/g-C_3N_4 synthesized by doping method. The formation of organic-metal hybrid material lead to the effective electrons transfer in the composites.	Meng et al., 2011
	Ag/g-C_3N_4 with different Ag amount was prepared by photodeposition under ambient condition. Photogenerated hole was the main reactive species in diclofenac degradation. The composites exhibited outstanding stability for the degradation of diclofenac over multiple reaction cycles because of the close contact between Ag and g-C_3N_4, and the LSPR effect of Ag.	Zhang et al., 2016
	Ag/g-C_3N_4 nanosheets were synthesized by photodeposition method where Ag NPs with diameters of 5~20 nm were uniformly deposited onto the surface of g-C_3N_4. Ag/g-C_3N_4 showed higher absorption peak within the visible spectrum range and suppressed the recombination rate of photoexcited electron-hole pairs.	Li et al., 2015
Pd	Pd/g-C_3N_4 was prepared by ultrasonication method. The Pd NPs with an average size of 4 nm were uniformly dispersed on the surface of g-C_3N_4. Under moderate reaction conditions, the composites exhibited higher efficiency in Suzuki–Miyaura reactions with up to 99% isolated yield.	Su et al., 2015
	The Pd/g-C_3N_4 synthesized *via* photoassisted method exhibited robust electrocatalytic behaviour towards the enhanced oxygen reduction reaction (ORR). This enhanced ORR activity might be ascribed to synergetic effects between g-C_3N_4 and Pd along with the even dispersion of the small Pd NPs. The developed catalyst demonstrated a significant improved tolerance against methanol as well as enhanced stability in comparison to the benchmark commercial platinum-loaded carbon catalysts.	Konda et al., 2016
Pt	Pt was loaded on g-C_3N_4 by chemical reduction process to form nanocomposites for the photoreduction of CO_2 under sunlight irradiation. With the aid of Pt NPs, more electrons were transferred from g-C_3N_4 to its surface for the photoreduction of CO_2. Simultaneously, Pt also acted as a catalyst to promote the oxidation of products.	Yu et al., 2014

Table 2.3, continued

Type of Noble Metals	Preparation Method & Finding Remarks	Reference
Pt	A chemical reduction process was used to deposit Pt NPs onto the surface of g-C_3N_4. The particle size of Pt NPs was around 2.5 nm. The Pt/g-C_3N_4 exhibited enhancement on the photoreduction of CO_2 to CH_4 in the presence of water vapour at ambient condition under visible light irradiation.	Ong et al., 2015
Au/Pt	Au/Pt/g-C_3N_4 was synthesized by a simple calcination-photodeposition technique. Au and Pt NPs with the sizes of 7-15 nm were evenly distributed onto the surface of g-C_3N_4. The Au/Pt co-decorated g-C_3N_4 composites showed improved photocatalytic performance for the degradation of antibiotic tetracycline hydrochloride (TC-HCl) and the degradation efficiency was 3.4 fold higher than that of pure g-C_3N_4 under visible light irradiation.	Xue et al., 2015b
Pd/Au	Pd/Au bimetallic NPs were decorated on g-C_3N_4-NS as a heterogeneous catalyst by a one-pot deposition co-reduction method. The Pd/Au@g-C_3N_4-NS (1:1) achieved a 100% conversion within only 4.5 min for the p-NP reduction. The as-synthesized material had excellent anti-oxidation and recyclability, which greatly promoted its industrial application.	Fang et al., 2017
Au/pg-C_3N_4/GR	A facile sonication-photodeposition method was used to synthesize Au-loaded porous g-C_3N_4/graphene layered, Au/pg-C_3N_4/GR. A layered composite was formed by immobilizing pg-C_3N_4 on the surfaces of graphene sheets with Au NPs of sizes 10–15 nm. The degradation rate of ciprofloxacin (CIP) over the Au/pg-C_3N_4/GR composite was 6.09 folds higher than that of bulk g-C_3N_4. The LSPR effect of Au improved the visible light harvesting ability and facilitated photogenerated charge carrier separation.	Xue et al., 2015a

2.7 Application of g-C_3N_4 Based Plasmonic Photocatalysts

In recent years, g-C_3N_4 is widely used for the photocatalytic degradation of organic pollutants. Upon light irradiation, the photocatalyst will generate the electron-hole pair. The holes will react with water (H_2O) or hydroxyl ion (OH^-) to form hydroxyl radicals ($^\bullet OH$), while electron will react with oxygen (O_2) to form superoxide anions radical ($^\bullet O_2^-$) as shows in Equation 2.4 and 2.5. The strong oxidizing activity of $^\bullet O_2^-$ and $^\bullet OH$ radicals will degrade the organic pollutants into almost non-toxic compounds, water, H_2O and carbon dioxide, CO_2. The complete mechanism is demonstrated in Figure 2.5.

$$O_2 + e^- \rightarrow {}^{\bullet}O_2^- \tag{2.4}$$

$$H_2O + h^+ \rightarrow {}^{\bullet}OH \tag{2.5}$$

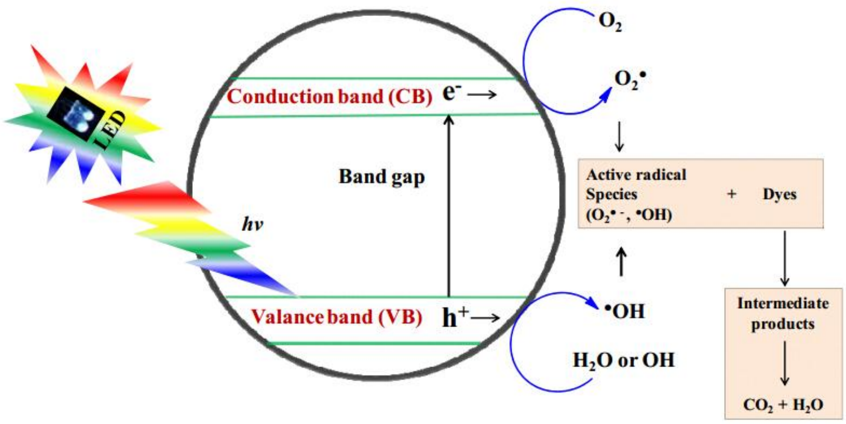

Figure 2.5: Schematic of Photocatalytic Mechanism (Jo and Tayade, 2014)

Ge and co-workers reported that Ag/g-C_3N_4 with 1 wt% of Ag showed an excellent visible light photocatalytic performance by completely degrading Methyl Orange (MO) (Ge et al., 2011b). Cheng et al. (2013) found that Au supported on g-C_3N_4 nanosheet greatly improved photocatalytic performance by degrading MO under visible light irradiation (Cheng et al., 2013). Tonda and co-workers synthesized Au/mesoporous g-C_3N_4 nanosheets which exhibited high photocatalytic activity for the degradation of rhodamine B under sunlight irradiation. Au NPs act as an electron reservoir to minimize the electron-hole recombination by trapping the electrons on the surface of Au NPs as shown in Figure 2.6. Furthermore, the SPR effect of noble metals NPs widens the absorption edge to visible region (Tonda et al., 2016). More related studies are reviewed and summarized in Table 2.4.

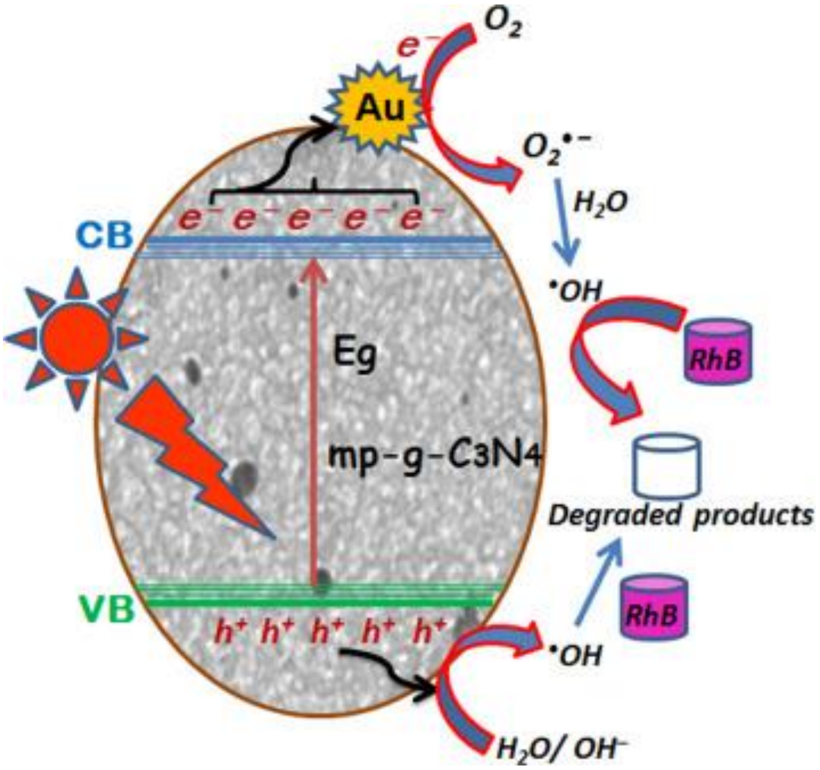

Figure 2.6: Schematic of Plasmonic Photocatalysts Photocatalytic Mechanism (Tonda et al., 2016)

Overall from past literature review, the modifications of g-C_3N_4 with noble metals well contributed to the photocatalytic removal of organic pollutants such as MO, Rhodamine B (RhB) and methylene blue (MB). However, organic dyes are photosensitizing compound and itself can be degraded under light irradiation. It is more preferable to use non photosensitizing pollutant like EDC to evaluate the photodegradation efficiency. Furthermore, most of the researches were utilized artificial light such as Xenon (Xe) lamp as the light source to induce the photodeposition of noble metals onto g-C_3N_4 and photodegradation of organic pollutants. However, the natural sunlight can potentially replace the artificial light as a sustainable route to induce photodeposition of noble metals onto the surface of photocatalyst. This could also promote the application of sunlight as sustainable energy input from the synthesis to application route.

Table 2.4: Summary of Literature Reports on Photodegradation of Organic Pollutants

Photocatalyst	Loading	Preparation Method	Organic Pollutant	[Initial Pollutant] (mg/L)	Radiation Period (min)	Light Source	Degrade Efficiency, %	Reference
g-C_3N_4	-	photoreduction (infrared light)	MO	10	180	500W Xe lamp (λ> 420nm)	30.0	Ge et al., 2011b
Ag/g-C_3N_4	0.5 wt% Ag						93.3	
Ag/g-C_3N_4	1.0 wt% Ag						100.0	
Ag/g-C_3N_4	1.5 wt% Ag						83.1	
Ag/g-C_3N_4	2.0 wt% Ag						72.7	
Ag/g-C_3N_4	3.0 wt% Ag						61.3	
Ag/g-C_3N_4	4.0 wt% Ag						33.3	
Ag/g-C_3N_4	5.0 wt% Ag						43.0	
g-C_3N_4	-	wet-chemical	MO	10	360	300 W Xe lamp (λ> 400nm)	21.0	Lü et al., 2014
Ag/g-C_3N_4	0.5 wt% Ag						32.9	
Ag/g-C_3N_4	1.0 wt% Ag						44.9	
Ag/g-C_3N_4	2.0 wt% Ag						57.1	
Ag/g-C_3N_4	5.0 wt% Ag						72.2	
Ag/g-C_3N_4	10.0 wt% Ag						81.7	
g-C_3N_4	-	Photodeposition (300 W Xe lamp)	MO	10	120	300 W Xe lamp (400< λ <680nm)	70.0	Yang et al., 2013
Ag/g-C_3N_4	0.1 wt% Ag						74.0	
Ag/g-C_3N_4	0.5 wt% Ag						78.0	
Ag/g-C_3N_4	1.0 wt% Ag						86.0	
Ag/g-C_3N_4	2.0 wt% Ag						91.0	
Ag/g-C_3N_4	5.0 wt% Ag						92.0	

Table 2.4, continued

Photocatalyst	Loading	Preparation Method	Organic Pollutant	[Initial Pollutant] (mg/L)	Radiation Period (min)	Light Source	Degrade Efficiency, %	Reference
g-C_3N_4	-	Photodeposition (Xe lamp)	diclofenac (DCF)	100	120	300 W Xe lamp (λ> 400nm)	79.0	Zhang et al., 2016
Ag/g-C_3N_4	10 wt% Ag						82.0	
Ag/g-C_3N_4	19 wt% Ag						91.0	
Ag/g-C_3N_4	32 wt% Ag						99.0	
Ag/g-C_3N_4	54 wt% Ag						99.5	
Ag/g-C_3N_4	70 wt% Ag						100.0	
`g-C_3N_4	-	Photodeposition (800 W Xe lamp)	RhB	10	30	800W Xe lamp (λ> 420nm)	33.0	Li et al., 2015
Ag/g-C_3N_4	1.0 wt% Ag						52.0	
Ag/g-C_3N_4	4.0 wt% Ag						85.0	
Ag/g-C_3N_4	8.0 wt% Ag						95.0	
Ag/g-C_3N_4	10.0 wt% Ag						77.0	
Bi_2WO_6	-	Photodeposition (500 W Xe lamp)	RhB	10	90	350 W Xe arc lamp (λ> 420nm)	25.0	Xiao et al.,2016
Ag/Bi_2WO_6	-						34.0	
g-C_3N_4	-						51.0	
C_3N_4/Bi_2WO_6	-						70.0	
C_3N_4/AgBi_2WO_6	-						100.0	

Table 2.4, continued

Photocatalyst	Loading	Preparation Method	Organic Pollutant	[Initial Pollutant] (mg/L)	Radiation Period (min)	Light Source	Degrade Efficiency, %	Reference
bulk g-C_3N_4	-	ultrasonication-assisted liquid exfoliation, photoreduction (visible light)	MO	10	150	500W Xe lamp (λ> 400nm)	21.5	Cheng et al., 2013
g-C_3N_4 nanosheets	-						28.7	
Au/bulk g-C_3N_4	55M						42.4	
Au/g-C_3N_4 nanohybrids	55M						92.6	
g-C_3N_4	-	photodeposition (mercury arc lamp, 250 W, λ =365 nm)	MB/CIP (ciprofloxacin)	10	180	500W Xe lamp (λ> 420nm)	47.4/44.5	Xue et al., 2015a
pg-C_3N_4	-						81.0/72.6	
pg-C_3N_4/GR	-						93.0/81.0	
Au/pg-C_3N_4	-						94.0/88.3	
Au/pg-C_3N_4/GR	5 wt% GR, 1wt% Au						100.0/96.7	
g-C_3N_4	-	two-step photoreduction (300 W Xe lamp)	RhB	10	30	300 W Xe lamp (λ> 400nm)	43.0	Peng et al., 2016
Au/g-C_3N_4	-						77.5	
CdS/g-C_3N_4	-						84.1	
CdS/Au/g-C_3N_4	-						90.1	

Table 2.4, continued

Photocatalyst	Loading	Preparation Method	Organic Pollutant	[Initial Pollutant] (mg/L)	Radiation Period (min)	Light Source	Degrade Efficiency, %	Reference
g-C_3N_4	-	calcination-photodeposition (mercury arc lamp, 250 W, λ=365nm)	tetracycline hydrochloride (TC-HCl)	20	180	500W Xe lamp (λ> 400nm)	52.8	Xue et al., 2015b
Pt/g-C_3N_4	0.5 wt% Pt						67.2	
Au/g-C_3N_4	2.0 wt% Au						78.6	
Au/Pt/g-C_3N_4	2.0 wt% Au, 0.5 wt% Pt						93.0	
mpg-C_3N_4	-	Chemical deposition	BPA	20	360	350 W Xe lamp	50.4	Chang et al., 2013
Pd/mpg-C_3N_4	0.15 wt% Pd						85.0	
Pd/mpg-C_3N_4	0.30 wt% Pd						96.0	
Pd/mpg-C_3N_4	0.60 wt% Pd						98.0	
Pd/mpg-C_3N_4	1.50 wt% Pd						100.0	
Pd/mpg-C_3N_4	3.00 wt% Pd						94.0	
Pd/mpg-C_3N_4	4.50 wt% Pd						91.9	
g-C_3N_4	-	photodeposition (visible light, λ >420 nm)	4-fluorophenol (4-FP)	10	240	300 W Xe lamp (λ> 420nm)	35.0	Zeng et al., 2017
Pt/g-C_3N_4	3 wt% Pt						47.0	
pg-C_3N_4	-						50.0	
Pt/pg-C_3N_4	1 wt% Pt						59.0	
Pt/pg-C_3N_4	2 wt% Pt						70.0	
Pt/pg-C_3N_4	3 wt% Pt						83.0	
Pt/pg-C_3N_4	4 wt% Pt						76.0	

2.8 Carbon Dots (CDs)

Carbon dots (CDs) are tiny carbon nanoparticles of a semiconducting material with size smaller than 10 nm and were initially isolated during the purification of single-walled carbon nanotubes (SWNTs) in 2004 (Xu et al., 2004). The properties of CDs rely on the starting material and the synthesis method. There are few methods used to synthesize CDs such as laser ablation, chemical ablation, microwave irradiation and hydrothermal. There are some unique properties of CDs, such as good electrical conductivity, strong fluorescent lifetime, water solubility, optical stability, low toxicity and nanoparticle size (Xu et al., 2015; Chen et al., 2016; Thambiraj and Shankaran, 2016). The fluorescent and low toxicity of CDs enable it applicable in biosensing (Zhang et al., 2015), bioimaging (Song et al., 2016) and chemical sensing (Tyagi et al., 2016). The carboxyl, hydroxyl and nitrogen groups attached on the surface of CDs improve the biocompatibility and optical property along with enhances the selectivity and sensitivity for metal ions (Zhang et al., 2016). Furthermore, CDs have unique property which make it applicable in photocatalysis such as photo-induced electron transfer, different emissive traps on the surface of CDs arising from quantum effect and the up-conversion photoluminescence (UCPL) that enable the conversion of near-infrared (NIR) light into shorter wavelength light (Li et al., 2016). These distinctive properties of CDs had motivated numerous researchers to utilize CDs in photocatalysis.

The synthetic methods for CDs are categorized into bottom up and top-down synthetic routes. Top-down methods refer to arc discharge, plasma treatment, electrochemical oxidation and laser ablation. The top-down approach requires expensive equipment and harsh physical or chemical conditions for oxidation or exfoliation of large carbon molecule like graphite rod, graphene, and carbon fiber in to CDs (Roy et al., 2015). The bad side of top-down approach is the quantum yield produced is very low, around tens of milligrams (Hu et al., 2013). Surface passivation could enhance the quantum yield of the particles by using the doping process (Jelinek, 2017). The bottom-up method utilize small molecules to synthesis CDs by applying external energy such as pyrolytic, microwave assisted, hydrothermal, chemical oxidation, and ultrasonic as shown in Table 2.5. The bottom up method utilizes abundant and low-cost organic materials or organic solvent that might harmful towards the environment and human health. Bottom-up approach is hard to manage the morphology and size distribution of CDs, due to the strong surface tension of nanoparticles that causes conglomeration (Bu et al., 2007). It is more cost effective in producing high quantum yield compared to top-down method.

Table 2.5 shows that hydrothermal treatment can produce higher quantum yield CDs compared to others synthesis approach, so hydrothermal treatment was adopted in this study. Hydrothermal treatment is an environmentally friendly, low cost and nontoxic route that is widely used to synthesize CDs from various bioprecursors, such as leaves, fruit, juice, waste peels and etc (Table 2.6). The chemical precursors can replace by bioprecursors to improve the sustainability of CDs. Hydrothermal method is a low level of oxygen heating, using low temperature to produce high quantum yield (Fadllan et al., 2017). Another feature of hydrothermal synthesis is the residue remained on the surface of crystalline cores, can be washed through chemical centrifugation.

Table 2.5: Summary of Typical Synthetic Methods of CDs

Routes	Methods	Precursors	Quantum Yield	Wavelength	References
Top-down	Laser ablation	polyethylene glycol	1.7 %	390 nm	Castro et al., 2017
		Graphite	4–10 %	450–650 nm	Sun et al., 2006
	Arc discharge	single-walled carbon nanotubes (SWNTs)	1.6 %	Yellow	Xu et al., 2004
		Oxidized carbon nanotubes	-	Blue to yellowish-green	Bottini et al., 2006
	Electrochemical oxidation	Graphite	2.8-5.2 %	Blue	Lu et al., 2009
		Graphite	8.9 %	450 nm	Yao et al., 2014
	Plasma treatment	polyethylene glycol	-	Blue to Green	Park et al., 2017
		Benzene	-	Green	Jiang et al., 2009
Bottom-up	Pyrolytic process	N-Hydroxysuccinimide.	14 to 31 %	Blue to Green	Stan et al., 2015
		Citric acid and glutathione	~80.3 %	Blue	Zhuo et al., 2015
	Microwave assisted method	Eggshell membrane	14 %	450 nm	Wang et al., 2012
		Folic acid	18.9 %	Blue	Guan et al., 2014
	Hydrothermal	folic acid	94.5 %	Blue	Liu et al., 2018
		Citric acid, ethylenediamine	94 %	450 nm	Qu et al., 2014
	Chemical oxidation	starch	11.4 %	Blue	Yan et al., 2015
		Acetic acid	-	Green	Fang et al., 2011
	Ultrasonic	Citrus limone	12.1-15 %	Blue	Oza et al., 2015
		Glucose	~7 %	Visible to near infrared	Li et al., 2011

Table 2.6: Hydrothermal Treatment Using Different Organic Precursors

Precursors	Methods	Quantum Yield	Particle Size (nm)	Application	References
Aloe	Hydrothermal 180^{o}C for 11 h	10.37 %	5 nm	Chemical Sensing	Xu et al., 2015
Orange pericarp	Hydrothermal 220^{o}C for 48 h	64 %	2.1 nm	Bio-imaging	Zhang et al., 2015
Lemon peel	Hydrothermal 200^{o}C for 12 h	14 %	1-3 nm	Photocatalyst	Tyagi et al., 2016
Pomegranate fruits	Hydrothermal 170^{o}C for 12 h	7.6 %	3.5 nm	Bio-imaging	Kasibabu et al., 2015
Coriander leaves	Hydrothermal 240^{o}C for 4 h	6.48 %	2.4 nm	Bio-imaging	Sachdev and Gopinath, 2015
Orange Juice	Hydrothermal 120^{o}C for 2.5 h	25.6 %	1.5-4.5 nm	Bio-imaging	Sahu, et al., 2012
Lignin	Hydrothermal assistance with H_2O_2	25 %	2-10 nm	Bio-imaging	Chen et al., 2016
Urea	Hydrothermal 160^{o}C for 6 h	44.7 %	5 nm	Ions sensing	Li et al., 2014
Hair	Hydrothermal 200^{o}C for 24 h	10.75 %	4.56 nm	Hg^{2+} sensing	Guo et al., 2016
Soy milk	Hydrothermal 180^{o}C	2.6 %	25 nm	Electrocatalysts	Zhu et al., 2012
Grass	Hydrothermal 180^{o}C for 3 h	4.2 %	3-5 nm	Ions sensing	Liu et al., 2012
Apple juice	Hydrothermal 180^{o}C for 3 h	4.27 %	3.72 nm	Bio-imaging	Mehta et al., 2015

2.9 Application of CDs Composites

The high solubility property of CDs limits its application in the degradation of organic pollutants in aqueous solution. This limitation can overcome by combining CDs with other semiconductor photocatalyst. Further the photocatalyst can act as a supported media to attach with CDs, so that can reclaim the photocatalyst with CDs. The incorporation of CDs and g-C_3N_4 was proved to promote the separation of electron hole pairs and increased the degradation efficiency (Cao et al., 2015). Owing to the narrow band gap of g-C_3N_4 (2.7 eV), the electrons can easily fall back into its original position. In this context, the fast recombination of electron-hole pair in g-C_3N_4 can be suppressed by combining g-C_3N_4 with CDs. When g-C_3N_4 and CDs are formed heterojunction, the differences in the CB and VB level between two photocatalysts causes band bending at the interface of junction. The band bending drives the photogenerated electrons and holes to move in opposite directions (Wang et al., 2013). One of the photocatalyst will serve as an electron/hole acceptor and hence the electron will not fall back easily to VB and recombine with the holes. The coupling mechanism enables the photocatalytic application of CDs in aqueous solution by supporting the highly soluble CDs with insoluble g-C_3N_4. Furthermore, the incorporate of CDs into g-C_3N_4 could enhance the light absorption capacity in entire visible and NIR range and promote more electron-hole pairs generate.

Zhang and coworkers (Zhang et al., 2016) showed an impressive performance for the photodegradation of phenol using the composites of CDs and g-C_3N_4. The performance of composite was boosted by UCPL properties of CDs and band alignment in the semiconductor-semiconductor junction.

Besides, N doped CDs (NCDs) and g-C_3N_4 composite were used for photodegradation of indomethacin in aqueous solution (Wang et al., 2017). The composite displayed enhanced visible light and near-infrared light absorption capacity. This is due to the UCPL properties of NCDs that empowered the composite to alter the wavelengths of light to shorter wavelengths. Fang et al. (2016) reported that the amount of CDs loaded into g-C_3N_4 was optimized at 0.25 wt%, achieving the best removal of RhB with degradation efficiency of 85%. The optimum amount of CDs loading is important factor that could affect the recombination rate of charges carrier. The excessive of CDs will act as recombination center instead of facilitating the electron transfer and thus deteriorating the photocatalytic performance of composite (Fang et al., 2016). Overall, CDs can form heterojunction with various photocatalysts to improve the entire light absorption range and to inhibit the recombination of electron-hole pairs by trapping the photogenerated electrons. The previous studies are summarized in Table 2.7.

There are some projects have been executed in this area, but most of the researchers focused on the application of citric acid-derived CDs and g-C_3N_4 composites for water splitting and organic dye degradation. The reported results are promising but there is still very limited research reported on the use of bioprecursors derived CDs and g-C_3N_4 composite for water remediation application especially for EDC removal. Therefore, few insights are yet to be discovered to fill the gaps of past studies. This includes producing CDs from WH leaves and utilizing sustainable sunlight to irradiate CDs which are more responsive to visible and NIR. With all the uncertain doubts, this study builds a foundation for further discovering green photocatalyst for water remediation.

Table 2.7: Summarized Different Types of CDs Composite with its Synthesis Method and Applications

Composite	CDs Loading	Composite Synthesis Method	CDs precursor/ Synthesis Method	Application	Radiation Period (min)	Light Source	Degradation Efficiency, %	Reference
g-C_3N_4	-	Impregnation-thermal	Citric acid / pyrolysis	Degradation of phenol	200	300 W Xe lamp (λ> 400nm)	43.0	Zhang et al., 2016
g-C_3N_4/CDs(0.1)	0.1 wt%						62.0	
g-C_3N_4/CDs(0.2)	0.2 wt%						81.0	
g-C_3N_4/CDs(0.5)	0.5 wt%						100.0	
g-C_3N_4/CDs(1.0)	1.0 wt%						85.0	
g-C_3N_4	-	Electrostatic adsorption	Graphite rod / electrochemical	Degradation of MB	120	Visible light	50.0	Jian et al., 2016
g-C_3N_4/CDs(0.1)	-						100.0	
g-C_3N_4	0	Thermal treatment	Candle Soot / hydrothermal	Rhodamine B	60	3 W Led lamp (λ= 370nm)	25.0	Fang et al., 2016
g-C_3N_4/CDs(4)	4 ml						58.0	
g-C_3N_4/CDs(5)	5 ml						85.0	
g-C_3N_4/CDs(6)	6 ml						45.0	
g-C_3N_4/CDs(10)	10 ml						40.0	

Table 2.7, continued

Composite	CDs Loading	Composite Synthesis Method	CDs precursor/ Synthesis Method	Application	Radiation Period (min)	Light Source	Degradation Efficiency, %	Reference
$g\text{-}C_3N_4$	0	Solvothermal	Citric acid / thermal treatment	H_2 generation (µmol)	240	300 W Xe lamp (λ> 420nm)	151.0	Li et al., 2016
$g\text{-}C_3N_4$/CDs(2)	2 ml						250.0	
$g\text{-}C_3N_4$/CDs(4)	4 ml						340.0	
$g\text{-}C_3N_4$/CDs(7)	7 ml						464.5	
$g\text{-}C_3N_4$/CDs(10)	10 ml						360.0	
$g\text{-}C_3N_4$	-	Hydrothermal	Sugarcane juice / hydrothermal	Degradation of BPA	90	Sunlight	68.2	Sim et al., 2018
$g\text{-}C_3N_4$/CDs(0.1)	0.1 wt%						78.0	
$g\text{-}C_3N_4$/CDs(0.2)	0.2 wt%						98.0	
$g\text{-}C_3N_4$/CDs(0.5)	0.5 wt%						100.0	
CDs	-	Solution dispersion	Orange peel / hydrothermal	Degradation of Naphthol blue-black (NBB)	45	UV light irradiation	4.4	Prasannan, and Imae, 2013
ZnO	-						84.3	
ZnO/CDs(1.0)	1.0 wt%						100.0	

Table 2.7, continued

Composite	CDs Loading	Composite Synthesis Method	CDs precursor/ Synthesis Method	Application	Radiation Period (min)	Light Source	Degradation Efficiency, %	Reference
TiO_2 TiO_2/CDs(10)	- 10 mL	Chemical mixing	Lemon peels / hydrothermal	Degradation of MB	120	UV light (12 W)	48.0 80.0	Tyagi et al., 2016
Bi_2WO_6 Bi_2WO_6/CDs(2) Bi_2WO_6/CDs(3) Bi_2WO_6/CDs(4) Bi_2WO_6/CDs(6)	- 2.0 g 3.0 g 4.0 g 6.0 g	Wet impregnation	Graphite rod / Electrochemical	Degradation of acetone (CO_2 production, ppm)	480	500 W Xe lamp (λ> 420nm)	200 220 300 380 190	Qian et al., 2016
g-C_3N_4 ZnO/g-C_3N_4/CDs(2) ZnO/g-C_3N_4/CDs(4) ZnO/g-C_3N_4/CDs(6)	- 2.0 wt% 4.0 wt% 6.0 wt%	Impregnation-thermal	Graphite rod / electrochemical	Degradation of Tetracycline	60	Xe lamp (λ> 420nm)	40.0 90.0 100.0 100.0	Guo et al., 2017
g-C_3N_4 g-C_3N_4/N-CDs(1)	- 1.0 wt%	Polymerize	Citric acid / hydrothermal	Degradation of indomethacin	90	350 W Xe lamp (λ> 420nm)	16.0 91.5	Wang et al., 2017

CHAPTER 3

RESEARCH METHDOLOGY

This chapter discusses the synthesis method and the materials used in this study for the preparation of different photocatalyst composites. It also covers the information on the characterizations techniques adopted to study its materials chemistry. The procedures of photocatalytic experiments to study the performance of synthesized photocatalysts are mentioned in this chapter. The overall process flow of the experiments are shown in Figure 3.1.

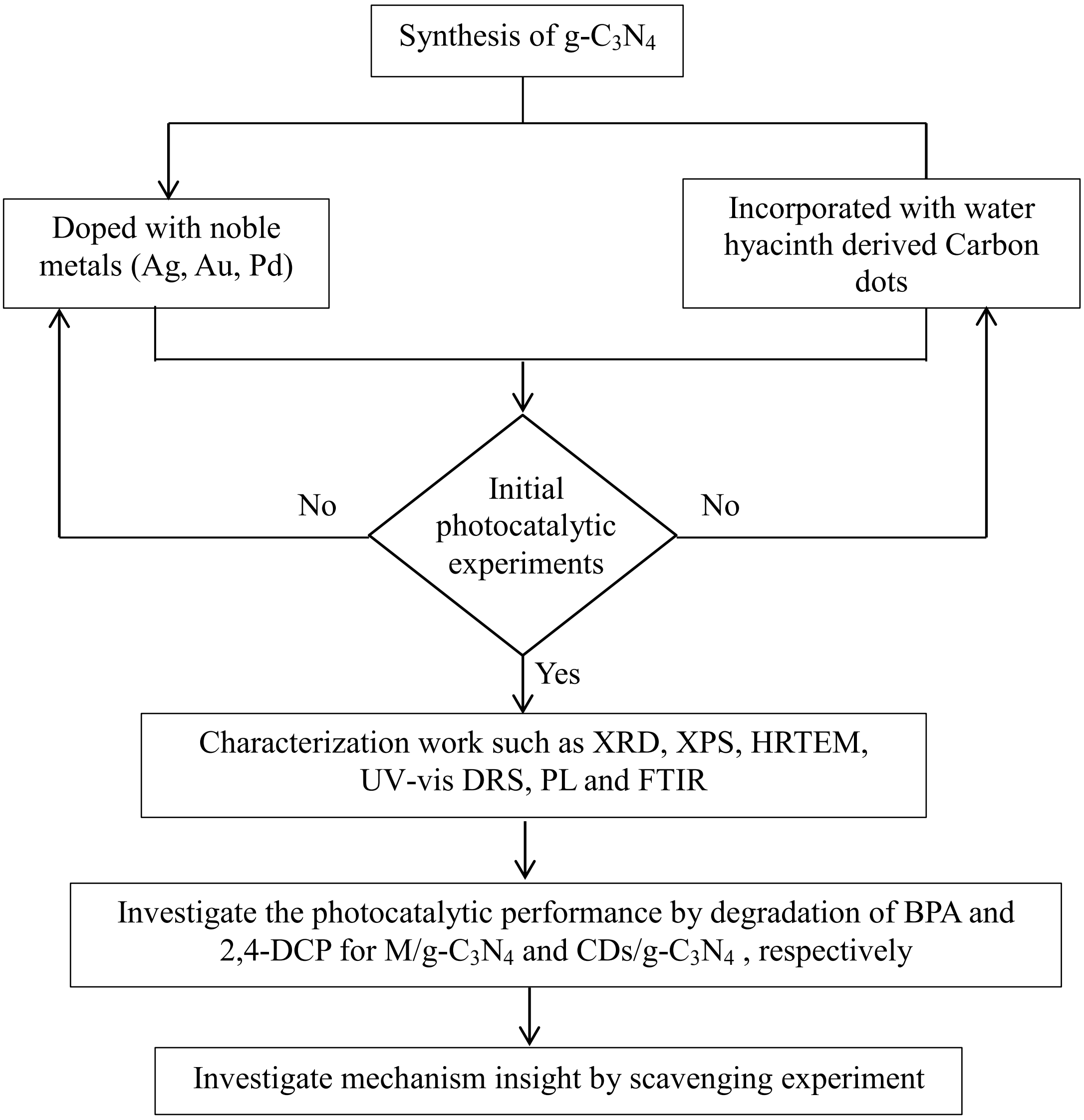

Figure 3.1: Process Flow Diagram of the Experiments

3.1 Materials

All the chemical reagents were of analytical grade and used without any further purification. Urea (99.8%, R&M Chemicals) powder was used to synthesize g-C_3N_4 *via* pyrolysis method. Gold (III) chloride trihydrate ($HAuCl_4$, 49.0%, Sigma–Aldrich), silver nitrate ($AgNO_3$, 99.9%, Sigma-Aldrich), and sodium tetrachloropalladate(II) ($Na_2[PdCl_4]$ 99.998%, Sigma–Aldrich) metal precursors were used as metal precursor to synthesize noble metals NPs. Ethylene glycol was used as hole scavenger to promote photodeposition. The ethanol was used as cleaning agent to remove the unreacted organic moieties. Milli-Q water was utilized for dilution and washing purpose during the entire experiment. The Bisphenol A (BPA, 99%, Sigma–Aldrich) and 2,4-dichlorophenol (2,4-DCP, 98.0%, Merck) were used as pollutant model for photocatalytic experiment. In addition, isopropyl alcohol (IPA, 83.5%, QReC), dimethylsulfoxide (DMSO, 99%, Univar), benzoquinone (BQ, 98%, Sigma-Aldrich) and ethylenediamine tetraacetic acid disodium salt (EDTA-$2Na^+$, 99%, Bio Basic Inc.) were used as scavengers in radical scavenging experiment.

3.2 Preparation of g-C_3N_4

The g-C_3N_4 was synthesized by using a facile thermal heating method. In details, 10 g of urea was placed in a crucible with a cover under ambient pressure and dried in an oven at 80 °C for 12 h. Then the crucible with dried urea was heated in a muffle furnace at 550 °C for 3 h at a heating rate of 10 °C min^{-1} to complete the reaction. The obtained yellow-colored product was washed with nitric acid (0.1 M) and Milli-Q water for 2 times each with centrifugation at 3500 rpm for 10 min to remove any residual alkaline species (e.g. ammonia) absorbed on the sample surface. Finally the washed derivative were dried overnight in an oven at 80 °C, the obtained g-C_3N_4 was well grounded in an agate mortar (Zhou et al., 2014). The photograph of the prepared g-C_3N_4 is shown in Figure 3.2.

Figure 3.2: Image of Synthesized g-C_3N_4

3.3 Preparation of carbon dots

CDs were prepared by hydrothermal treatment of water hyacinths (WH) leaves. First, the water hyacinths leaves were dried under natural sunlight to remove the moisture and finely grinded into powder. 5 g of prepared leaves powder were mixed with 120 mL of Milli-Q water and stirred for 30 min to make the mixture homogeneous. After that, the mixture was transferred into the 150 mL Teflon-lined stainless-steel autoclave to undergo hydrothermal treatment process in the oven for 4 h at 200 °C (Sachdev and Gopinath, 2015). After heating, the autoclaves were allowed to naturally cool down at room temperature for more than 1 h and the CDs were collected by removing larger particles through centrifugation at 10000 rpm for 15 min. The upper light yellowish-brown solution containing CDs were obtained and then dried overnight in an oven at 100 °C converted into solid form to measure the weight (Tyagi et al., 2016). After that, the solid CDs were diluted with 1 L Milli-Q water to obtain the concentration (mg/L). Finally, the CDs solution was stored at 4 ℃ for further characterization and incorporation with g-C_3N_4. Figure 3.3 (a) and (b) show diluted CDs solution under daylight and UV light.

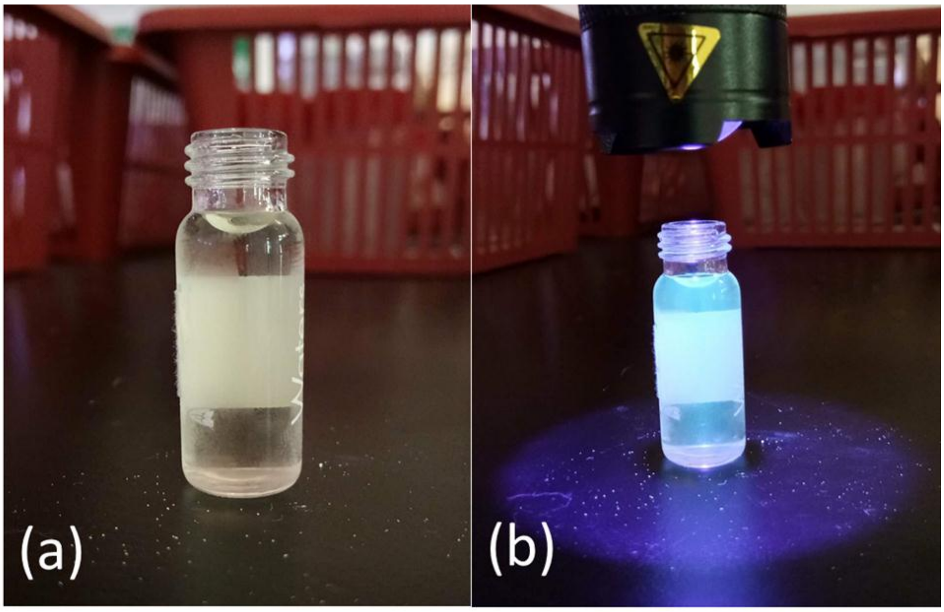

Figure 3.3: Water Hyacinths Derived CDs Solution under (a) Daylight (b) UV Light

3.4 Modification of g-C_3N_4

The synthesized g-C_3N_4 was further modified with different noble metals (Ag, Au and Pd) and CDs. The preparation method is discussed clearly in the following sections.

3.4.1 Preparation of M/g-C_3N_4 Composite (M=Au, Ag, Pd)

The Au/g-C_3N_4 NPs composite was synthesized by photodeposition method using sunlight. The prepared g-C_3N_4 (0.5 g) was added to 20 mL of ethylene glycol containing a chosen amount of $HAuCl_4$ (40 mM) and the sample was then sonicated for 30 min. The resulting suspension was exposed under sunlight with light intensities ranging from 120 to 160 W/m^2 to trigger the reduction reaction. The process was continuously stirred for 60 min to promote sustainable photochemical reduction. The schematic diagram and photograph of experimental setup is shown in Figure 3.4 and 3.5. The precipitate was reclaimed by centrifugation at 2500 rpm for 10 min. Finally the obtained Au/g-C_3N_4 was washed repeatedly with ethanol and Milli-Q water, followed by drying in oven for overnight at 80 °C. The prepared Au/g-C_3N_4 was fine grounded into powder form in agate mortar (Leong et al., 2014). Both of Ag/g-C_3N_4 and Pd/g-C_3N_4 composites were synthesized with the same procedure by using $AgNO_3$ and $Na_2[PdCl_4]$, respectively as noble metal precursor. The synthesized composites were shown in Figure 3.6.

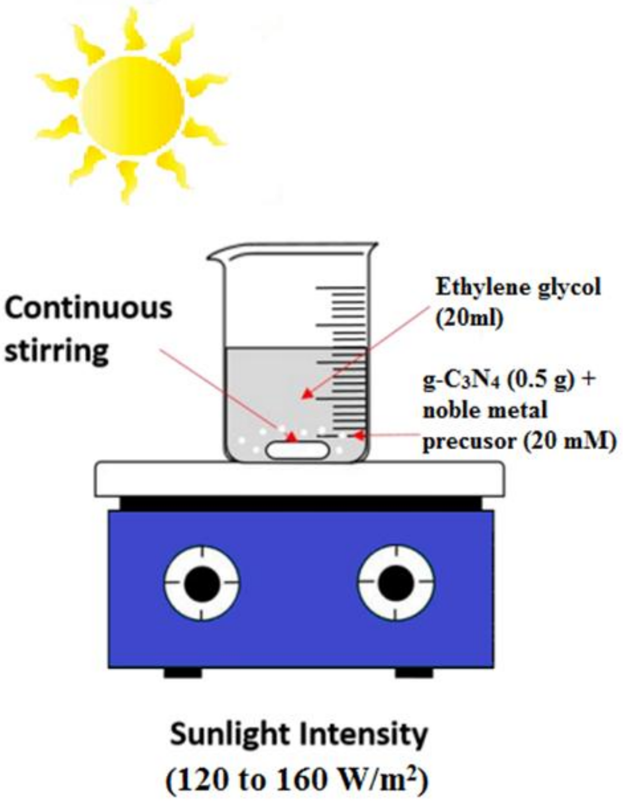

Figure 3.4: Schematic of Photodeposition Experimental Setup

Figure 3.5: Photograph of Photodeposition Experimental Setup

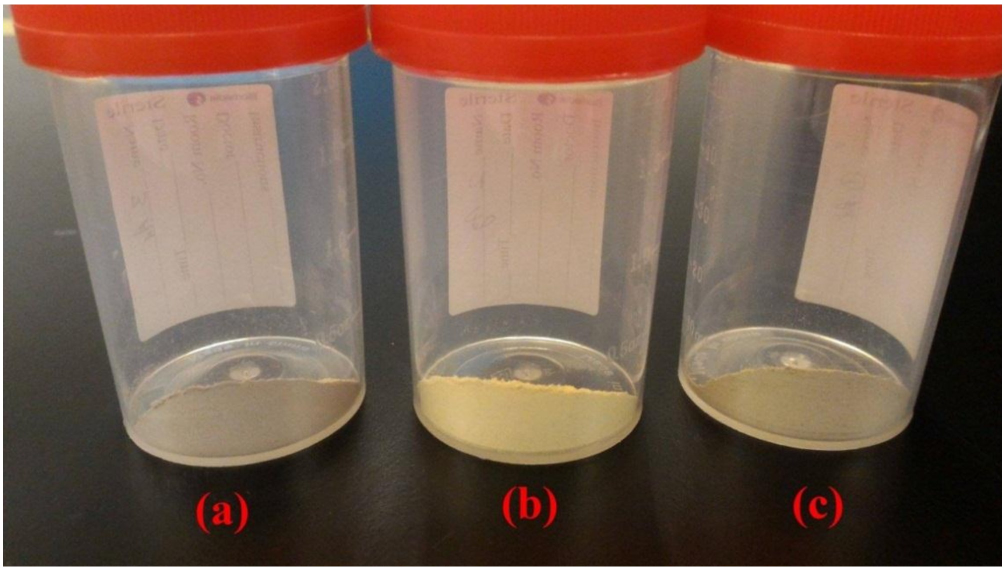

Figure 3.6: Image of Synthesized (a) Au/g-C_3N_4, (b) Ag/g-C_3N_4 and (c) Pd/g-C_3N_4

3.4.2 Preparation of CDs/g-C_3N_4 Composites

0.6 g of g-C_3N_4 was mixed with 23 mL of CDs solution and vigorously stirred for 24 h at room temperature to obtain a homogeneous suspension. After that, the mixture was shifted into a 100 mL Teflon-lined stainless steel autoclave and heated for 2 h at 100 °C. Then the autoclave was cooled down naturally for 1 h and the obtained products were washed and collected by centrifugation. The washed sample was then dried overnight at 80 °C (Sim et al., 2018). CDs/g-C_3N_4 composite with different CDs weight percentage of (0.6 wt%, 20 wt% and 40 wt%) was synthesized using the same procedures stated above. The synthesized composites were indicated as 0.6CDs/g-C_3N_4, 20CDs/g-C_3N_4 and 40CDs/g-C_3N_4, respectively and were shown in Figure 3.7.

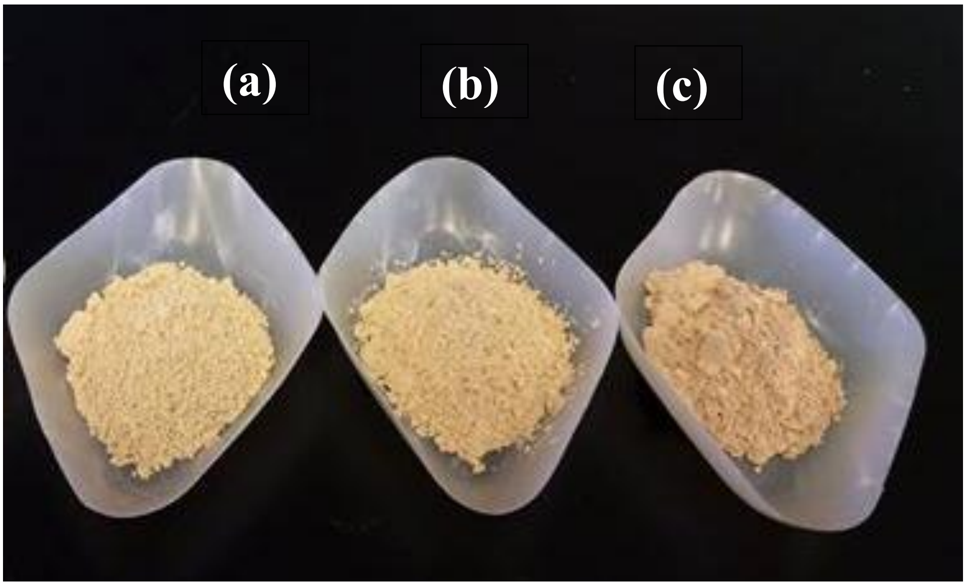

Figure 3.7: Image of Synthesized (a) 0.6CDs/g-C_3N_4, (b) 20CDs/g-C_3N_4 and (c) 40CDs/g-C_3N_4

3.5 Characterization

The morphology and composition of both M/g-C_3N_4 and CDs/g-C_3N_4 were observed using a field emission scanning electron microscope (FESEM, Auriga, Zeiss) equipped with an energy dispersive X-ray spectroscopy (EDS). The images were obtained at an accelerating voltage of 20 kV. High resolution transmission electron microscope (HRTEM, Tecnai 20, Philips) images were obtained at 200 kV. The crystalline phase was identified using an X-ray diffractometer (XRD, D8 Advance, Bruker). The target used in the diffractometer is copper (Cu Kα radiation, $\lambda = 1.54$ Å). The surface chemical composition of samples was analyzed by X-ray photoelectron spectroscopy (XPS, Axis Ultra DLD, Kratos) with Al Kα radiation source. Peak fitting to the spectra was applied using Gaussian-Lorentzian peak shape after subtraction of Shirley background. The binding energy of C 1s peak at 284.6 eV was used as internal charge correction. The Fourier transform infrared (FTIR) spectra of products were obtained on a Perkin Elmer Spectrum 400 spectrophotometer at the range of 400–4000 cm^{-1}. Ultraviolet-visible diffuse reflectance spectra (UV-vis DRS) were performed using UV-vis NIR spectrophotometer (UV-260, SHIMADZU) with a wavelength range of 200–800 nm. A micro-PL/Raman spectroscope (Renishaw, inVia Raman Microscope) was used to acquire the Raman and photoluminescence (PL) spectra with the excitation wavelengths of 514 and 325 nm, respectively. Brunauer-Emmett-Teller (BET) surface area was based on nitrogen adsorption-desorption isotherms with TriStar II 3020 (Micrometrics®, USA). Photoluminescence (PL) spectra of CDs solution were acquired with a PL spectrophotometer (Perkin Elmer LS 55). An Edinburgh FLS 920 Time Resolved Photoluminescence (TRPL) was used to acquire TRPL spectrum and exciton decay lifetime of x-FZNR/P3HT active layers were obtained using a 376.4 nm picosecond pulsed laser as the excitation source with excitation wavelength 480 nm. The average lifetime, τ of the excited charge-carrier was calculated using the equation below:

$$\tau= (B_1T_1^2+B_2T_2^2+B_3T_3^2)/(B_1T_1+B_2T_2+B_3T_3) \tag{3.1}$$

3.6 Photocatalytic Experiments

3.6.1 M/g-C_3N_4 Composites (M=Ag, Au, Pd)

The photocatalytic performance of the prepared Au/g-C_3N_4, Ag/g-C_3N_4 and Pd/g-C_3N_4 were evaluated by degrading Bisphenol A (BPA). The entire experiments were implemented as batch manner in a 500 mL beaker, while the functioning volume was 200 mL. The initial concentration of BPA was set at 5 mg/L for all the study with 0.1 g photocatalyst loading under stirring conditions. Prior to photodegradation, the solutions were magnetically stirred in a dark for 2 h to establish an adsorption-desorption equilibrium. All the photocatalytic experiments were carried out under direct sunlight between 11:00 am and 2:00 pm in March 2017 at Universiti Tunku Abdul Rahman, Perak (longitude 4.3394° N and latitude 101.1398° E). The average solar intensity over the duration of clear sky weather condition was measured to be ~108000 lux (158 W/m^2) by using Light meter HS1010A of 2000 × 100. Control and blank experiments were also carried out for comparison purpose. Table 3.1 shows the recorded light intensity during the photodegradation. The experimental configuration is illustrated in Figure 3.8 and 3.9. The BPA samples were withdrawn at regular intervals, centrifuged and analyzed for residual concentration using a high-performance liquid chromatography (HPLC, PerkinElmer Flexar) equipped with fluorescence detector and Ascentis C18 column (Supelco Analytical, USA) (15 cm × 4.6 mm × 5 μm). Acetonitrile (ACN) and water in the ratio 40:60 were used as mobile phase with flow rate of 1.0 mL/min for BPA quantification. The BPA was quantified with an excitation and emission wavelength of 226 nm and 305 nm, respectively. The retention time was found to be 0.71 min. The calibration curve adopted for quantification of BPA is shown in Figure 3.10.

Table 3.1: The Intensity of Sunlight for Photodegradation

Time Interval (min)	0	15	30	45	60	75	90	105	120
Light intensity (x100 lux)	1067	1080	1079	1081	1085	1082	1083	1081	1081

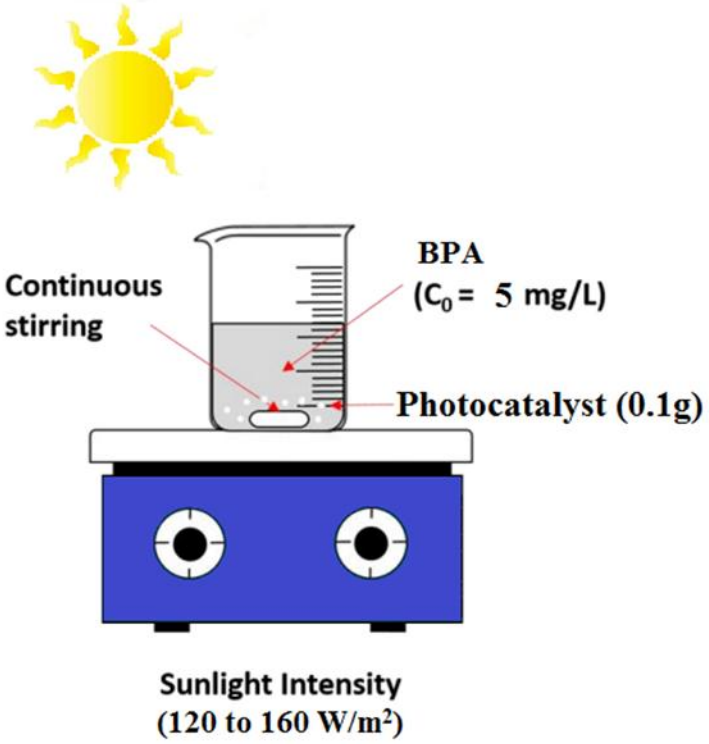

Figure 3.8: Experimental Setup for Solar Photocatalysis Experiment

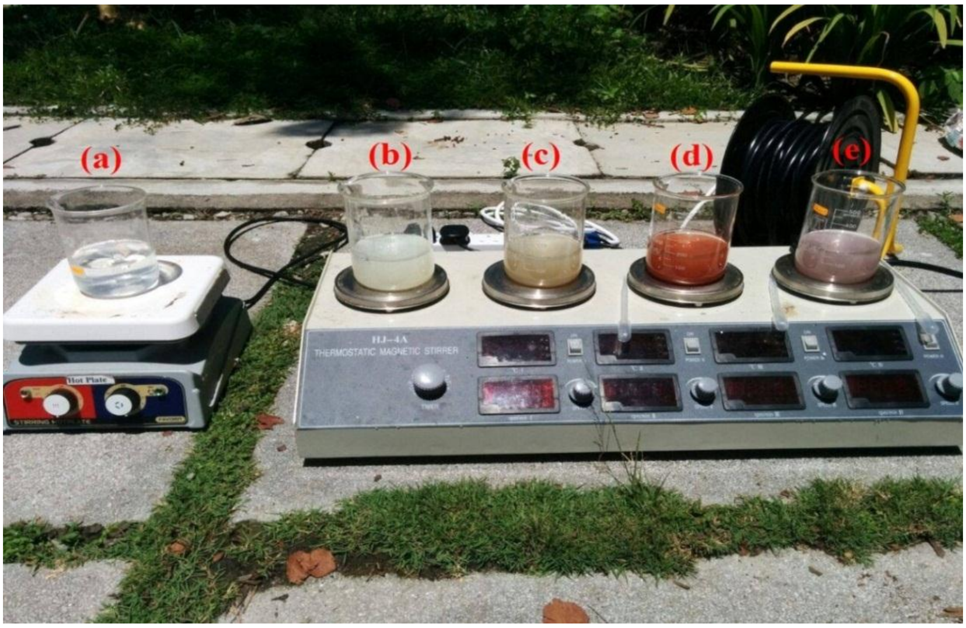

Figure 3.9: Image of Experimental Setup for the Sunlight Driven Photocatalytic Degradation of BPA for (a) Blank, (b) g-C_3N_4, (c) Pd/g-C_3N_4, (d) Ag/g-C_3N_4 and (e) Au/g-C_3N_4

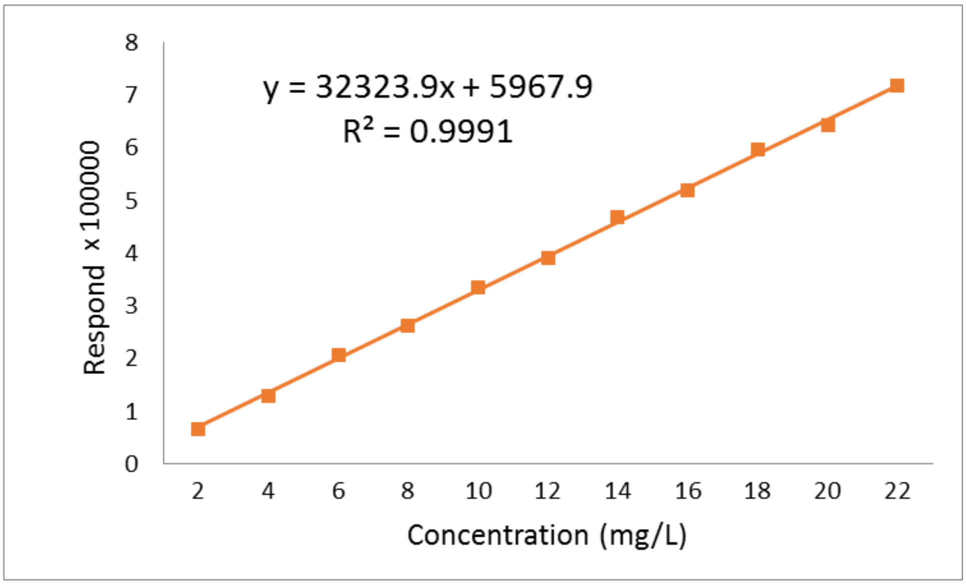

Figure 3.10: Calibration Curve for BPA

3.6.2 CDs/g-C_3N_4 Composites

The photodegradation of 2,4-DCP was carried out in a 500 mL beaker with the working volume of 200 mL 2,4-DCP solution (5 mg/L). 0.1 g of the prepared 0.6CDs/g-C_3N_4, 20CDs/g-C_3N_4 and 40CDs/g-C_3N_4 composites were loaded in 2,4-DCP solution. A pre-experiment was carried out in dark condition for more than 12 h to acheive the adsorption-desorption equilibrium. The 2,4-DCP samples were analyzed every 15 min using the same HPLC equipment mentioned above. The mobile phase was acetonitrile (ACN) and water in the ratio 80:20 with a flow rate of 0.8 mL/min. An UV detector was used to quantify 2,4-DCP with an analytical wavelength 280 nm. The retention time was found to be 0.25 min. The calibration curve utilized for quantification of 2,4-DCP concentration is shown in Figure 3.11. The experimental setup is same as Figure 3.8 and 3.9.

The experiment for CDs/g-C_3N_4 was executed under clear sky condition at Universiti Tunku Abdul Rahman, Perak, (longitude 4.3394° N and latitude 101.1398° E) between 11.00 am and 2.00 pm in December 2017.

Sunlight light intensity was dignified using Light meter HS1010A of 2000 × 100 lux and the average light intensity over the duration was found to be 104000 lux. Table 3.2 showed the recorded light intensity during the photodegradation.

Table 3.2: The Intensity of Sunlight for Photodegradation

Time Interval (min)	0	15	30	45	60	75	90	105	120
Light intensity (x100 lux)	924	931	1019	1066	1075	1077	1081	1097	1098

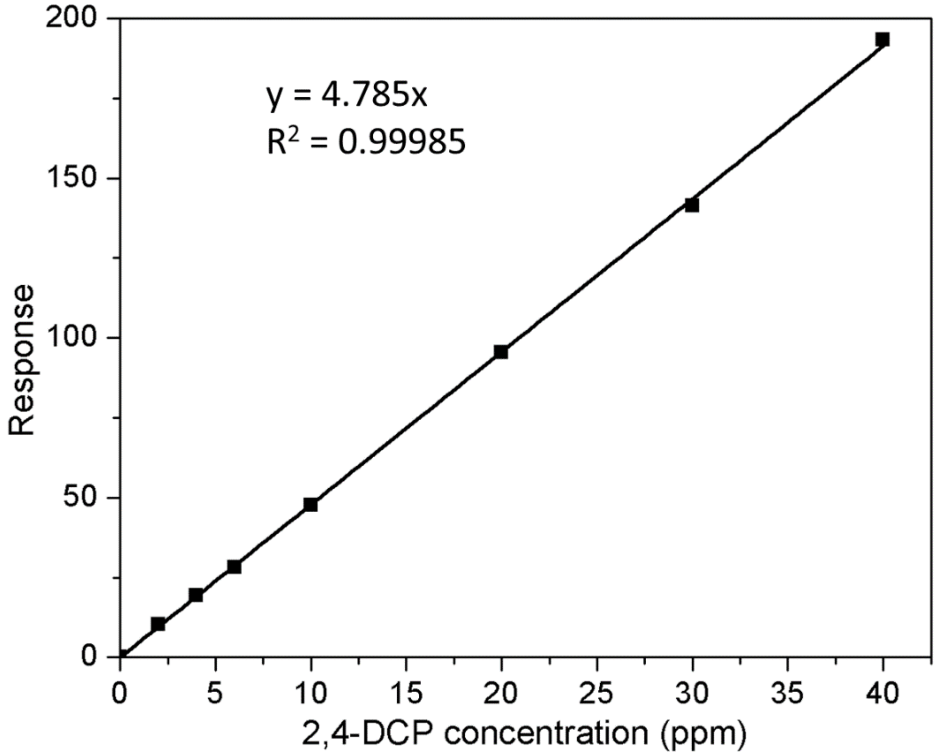

Figure 3.11: Calibration Curve for 2,4-DCP

3.6.3 Near Infrared (NIR) Degradation Test

40CDs/g-C_3N_4 was adopted as the representative photocatalyst to evaluate the photocatalytic performance under NIR illumination. This is to investigate the contribution of CDs towards NIR-driven photocatalysis Similar experiment procedure in section 3.6.2 was repeated with the additional placement of NIR filter glass (λ=730 nm) on top of the beaker. The surrounding of beaker was covered by aluminum foil to prevent the solution absorbing UV and visible light. The experimental setup was shown in Figure 3.12. The light intensity during the photodegradation was recorded in Table 3.3.

Table 3.3: The Intensity of Sunlight for NIR Degradation Test.

Time Interval (min)	0	15	30	45	60	75	90	105	120
Light intensity (x100 lux)	842	911	954	937	996	1024	983	965	1018

Figure 3.12: Image of Experimental Setup for NIR Degradation Test

3.6.4 Scavenger Test

A radical scavenger experiment was executed to detect the core reactive radical species associated in the photodegradation of both BPA and 2,4-DCP. The scavenging experiment was carried out by adding 2 mM dimethylsulfoxide (DMSO) which served as electron (e^-) scavenger. This experiment was repeated by adding 2 mM ethylenediamine tetraacetic acid disodium salt (EDTA-2Na$^+$), benzoquinone (BQ) and isopropyl alcohol (IPA) which acted as hole (h^+) scavenger, superoxide radical ($^\bullet O_2^-$) scavenger and hydroxyl radical ($^\bullet OH$) scavenger, respectively. Table 3.4 to 3.7 shows the recorded light intensity during the radical scavenger experiment.

Table 3.4: The Intensity of Sunlight for Scavengers Test, Ag/g-C_3N_4

Time Interval (min)	0	15	30	45	60	75	90	105	120
Light intensity (x100 lux)	1060	1073	1083	1077	1080	1068	1081	1082	1060

Table 3.5: The Intensity of Sunlight for Scavengers Test, Au/g-C_3N_4

Time Interval (min)	0	15	30	45	60	75	90	105	120
Light intensity (x100 lux)	953	999	963	1041	992	989	1005	989	970

Table 3.6: The Intensity of Sunlight for Scavengers Test, Pd/g-C_3N_4

Time Interval (min)	0	15	30	45	60	75	90	105	120
Light intensity (x100 lux)	833	804	780	776	701	762	727	887	966

Table 3.7: The Intensity of Sunlight for Scavengers Test, CDs/g-C_3N_4

Time Interval (min)	0	15	30	45	60	75	90	105	120
Light intensity (x100 lux)	923	967	914	932	868	703	755	941	953

CHAPTER 4

RESULTS AND DISCUSSION

This chapter presents the obtained results along with the analysis, interpretations and science behind those observations. Two co-catalysts were used to modify g-C_3N_4, namely noble metals (M=Pd, Ag, Au) and carbon dots (CDs). In section 4.1, different types of noble metals (Au, Ag and Pd) were used to modify g-C_3N_4 to produce M/g-C_3N_4 composites (M=Pd, Ag and Au) for the improvement of photocatalytic performance. In section 4.2, water hyacinth (WH) leaves derived carbon dots were coupled with g-C_3N_4 to produce CDs/g-C_3N_4 composites *via* green synthesis route. In both sections, the characteristics of the synthesized g-C_3N_4 based composites were analyzed with various spectroscopic and microscopic techniques. The photocatalytic performance and the degradation mechanism of the modified g-C_3N_4 composites were also discussed. In section 4.3, the preparation cost of photocatalyst of both projects was calculated to determine the sustainability.

4.1 Doping g-C_3N_4 with Different Noble Metals (M=Pd, Ag and Au)

In this study, different types of noble metals (Au, Ag, Pd) were deposited onto the g-C_3N_4 surface via simple sunlight photodeposition method to validate the significance effect of LSPR and Schottky barrier towards the enhancement of the photocatalytic performance and photocatalysis mechanism. The visible light driven photocatalysis of the prepared composites was evaluated by degrading BPA under natural sunlight irradiation. Besides, the radical scavenging test was carried out to determine reactive radical species which were responsible for the superior photodegradation ability of the composites.

The X-ray diffraction patterns (XRD) of g-C_3N_4, Pd/g-C_3N_4, Ag/g-C_3N_4 and Au/g-C_3N_4 composites are shown in Figure 4.1. For the pure g-C_3N_4, a weak diffraction peak was observed at 12.78° indexed to the (1 0 0) crystal plane of g-C_3N_4 arising from in-plane structural packing motif of tri-s-triazine units with an interplanar distance of 0.675 nm (Pawar et al., 2015a). Simultaneously, another strong diffraction peak at 27.58° corresponded to the interlayer stacking of aromatic segments which can be indexed to the (0 0 2) crystal plane with a distance of 0.326 nm (Su et al., 2015). The diffraction peak of the g-C_3N_4 can be assigned to the hexagonal phase of g-C_3N_4 (JCPDS 87-1526) (Ge et al., 2011a,b). For Au/g-C_3N_4 composite, four additional peaks appeared at 38.15°, 44.37°, 64.59° and 77.51° were assigned to (1 1 1), (2 0 0), (2 2 0) and (3 1 1) planes of face-centered cubic Au NPs (JCPDS 65-2870) (Han et al., 2015). This result confirmed the deposition of Au NPs on the surface of g-C_3N_4 layer. Compared with g-C_3N_4, a significant decrease of (0 0 2) peak intensity was observed in Au/g-C_3N_4 because the introduction of Au NPs inhibited the growth of g-C_3N_4 layer (Samanta et al., 2014) and reduced the amount of layered structure. The similar pattern was also observed for both Pd/g-C_3N_4 and Ag/g-C_3N_4 composites.

Furthermore, the diffractions peak ascribed to the phase structure of Ag and Pd NPs were not pronounced, indicating low contents and highly homogeneous dispersion of Ag and Pd NPs on the g-C_3N_4 sheets (Zeng et al., 2017). In addition, after deposition of noble metals NPs with g-C_3N_4, the diffraction peak positions of g-C_3N_4 for all composites remain unaltered. This demonstrates that the noble metals NPs are deposited on the surface of g-C_3N_4 instead of being incorporated into the lattice of g-C_3N_4 (Yu et al., 2014). The crystallite size of the Au NPs in Au/g-C_3N_4 composite was calculated by using the Scherrer equation (Equation 4.1) and was found to be 9.5 nm.

$$D = \frac{k\lambda}{\beta\cos\theta} \qquad (4.1)$$

where D is the crystallite size (nm), *k* is the shape factor (0.89), *λ* is the wavelength of Cu Kα radiation (λ=1.5406 Å), *β* is the full width at half maximum (FWHM) for the 2θ peak (radians) and *θ* is the diffraction angle (degree).

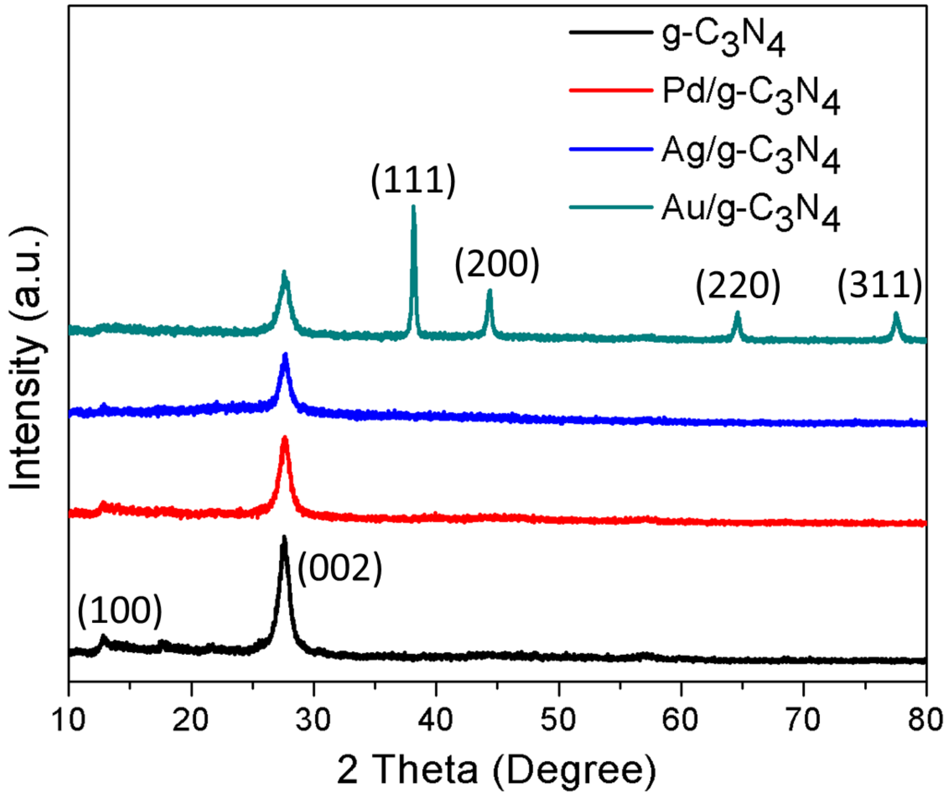

Figure 4.1: XRD Pattern of g-C_3N_4 and M/g-C_3N_4 (M=Pd, Ag and Au)

The chemical structure information of the g-C_3N_4, Pd/g-C_3N_4, Ag/g-C_3N_4 and Au/g-C_3N_4 composites were investigated by FTIR spectroscopy and presented in Figure 4.2. For pure g-C_3N_4, the sharp peak at 808 cm^{-1} was attributed to the breathing mode of whole s-triazine unit, revealing the formation of s-triazine unit. A series of strong absorption peaks in the range of 1100–1700 cm^{-1} are ascribed to the stretching vibrations of sp^3 C–N and sp^2 C=N bonds in the CN heterocycles with peaks centered at 1241, 1393, 1434 and 1630 cm^{-1}. The broad absorption peak located in the range of 2900–3500 cm^{-1} was observed and originated from the stretching vibration modes of N–H and surface adsorbed O–H group (Liang et al., 2015). The presence of N–H stretching vibration modes indicated that some uncondensed amine functional groups still existed in the carbon nitride layer (Samanta et al. 2014). The spectrum of Pd/g-C_3N_4, Ag/g-C_3N_4 and Au/g-C_3N_4 were similar to g-C_3N_4 since all of them are mainly consist of g-C_3N_4. In addition, noble metals reflect lights and cannot be detected by FTIR.

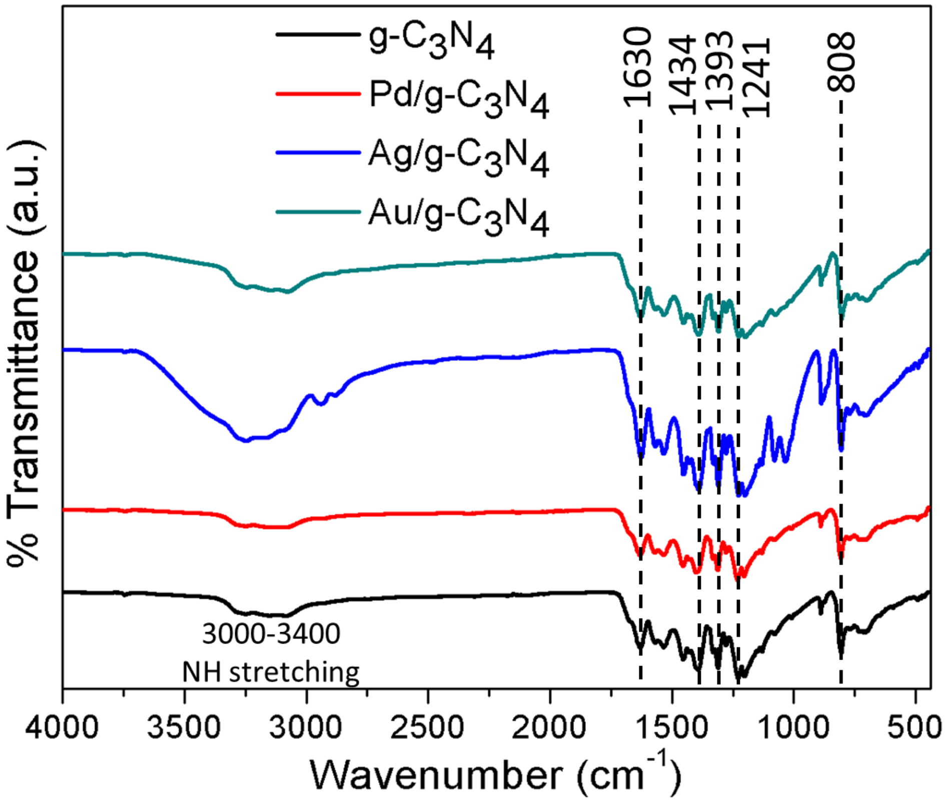

Figure 4.2: FTIR Spectra of g-C_3N_4 and M/g-C_3N_4 (M=Pd, Ag and Au)

The morphologies of synthesized samples were characterized by SEM, EDX, TEM and HRTEM and the obtained images are shown in Figure 4.3. The obtained FESEM images for Pd/g-C_3N_4, Ag/g-C_3N_4 and Au/g-C_3N_4 composites exhibited a typical lamellar structure, which is composed of numerous irregular nanosheets (NS) of g-C_3N_4 with a thickness of few nanometers (Liang et al., 2015). The structure of g-C_3N_4 remained unchanged after the doping of Au, Ag and Pd nanoparticles (NPs). The EDX spectrum of all M/g-C_3N_4 composites confirmed the existence of carbon (C), nitrogen (N) and oxygen (O) in all g-C_3N_4 based composites. The formation of noble metal (M=Pd, Ag and Au) onto the surface of g-C_3N_4 was clearly unveiled in respective composites by EDX spectrum. The presence of noble metal NPs was obviously identified from the dark contrast in the TEM images of all composites, indicating a well dispersion of noble metals over the g-C_3N_4 nanosheets. From the HRTEM images, the lattice fringes of 0.23, 0.235 and 0.23 nm were attributed to Pd (1 1 1), Ag (1 1 1) and Au (1 1 1) respectively (Li et al., 2015a,b; Zhao et al., 2016; Leong et al., 2015b). The average particles sizes are 7.3, 7.5 and 8.6 nm for each Pd, Ag and Au NPs as shown in Figure 4.4. The particle size of Au NPs falls within the range of 3–12 nm which is favorable for the enhancement of photocatalytic performance (Murdoch et al., 2011). The particle size of Pd NPs smaller than 6 nm was reported to absorb UV light only, while larger and cluster able to absorb in visible region (Mohapatra et al., 2008). Thus as obtained Pd NPs (7.3 nm) in our work are able to absorb visible light effectively. The absorption band of the Ag NPs revealed a unique behavior, it blue-shifted as the size falls in the range of 12–20 nm but then turned over strong red-shift with the sizes smaller than 12 nm (Peng et al., 2010). In addition, Ag NPs with decreasing sizes below 20 nm will serve as a more advanced media to suppress the recombination rate of photogenerated electron-hole pairs (Jiang et al., 2014). These results suggest that the particle size of all photodeposited noble metals could promote pronounced visible light harvesting effect under full solar spectrum irradiation.

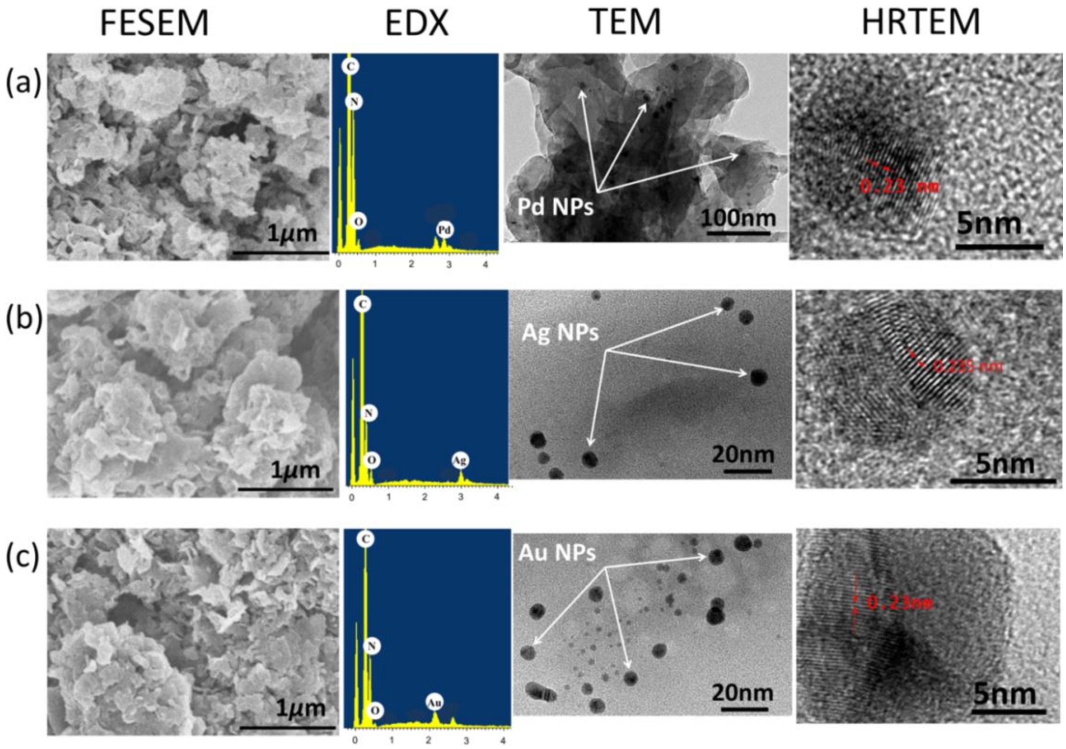

Figure 4.3: FESEM, EDX, TEM and HRTEM Images of (a) Pd/g-C_3N_4 (b) Ag/g-C_3N_4 (c) Au/g-C_3N_4 Composites

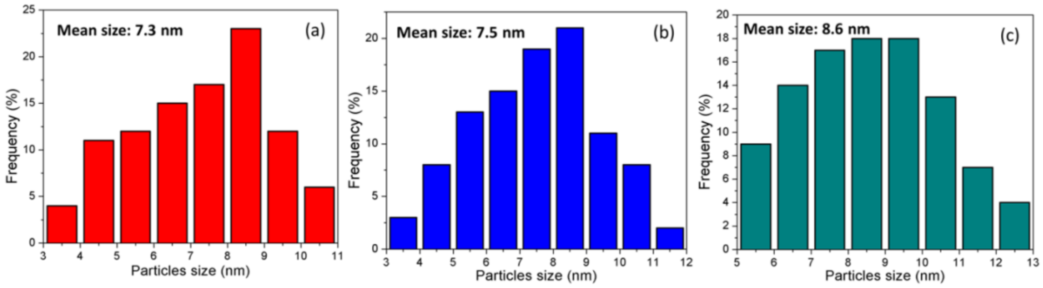

Figure 4.4: Average Particles Size Histogram of the Synthesized (a) Pd (b) Ag (c) Au NPs

The surface composition and chemical state of the prepared samples were further elucidated by XPS analysis and the obtained results were presented in Figure 4.5. The XPS survey spectrum in Figure 4.5(a) indicates the existence of C, N and O component in all g-C_3N_4 based composites and the atom percentage of the components were shown in Table 4.1. The presence of small amount of Cl element was originated from the synthesis route when g-C_3N_4 was doped with noble metals precursor such as $HAuCl_4$ and $Na_2[PdCl_4]$. The weak signal of Ag, Au and Pd was due to their low contents (Liang et al., 2015). Figure 4.5(b-d) shows the narrow scan of M/g-C_3N_4, the C1s peak was deconvoluted into four peaks which is C-C (284.69 eV), C-O (286.20 eV), C=O (287.70 eV) and COOH (288.51 eV). In the N1s spectrum shown in Figure 4.5 (e-g), the main peak observed at 398.18 eV was ascribed to CN=C coordination which originated from the sp^2-bonded N in triazine rings, while the other two weak peaks observed at binding energies 398.91 and 400.44 eV were ascribed to N-$(C)^3$ and C-N-H species (Fu et al., 2015). In Figure 4.5(h-j), the peak observed at 531.59 eV was assigned to some hydroxyl groups (OH) attached on the surface of g-C_3N_4 (Samanta et al., 2014).

The predominant existence of the metallic form Ag NPs was shown by peaks at binding energies 367.6 and 373.5 eV with 5.9 eV spin energy separation, corresponded to Ag $3d_{5/2}$ and Ag $3d_{3/2}$ respectively (Figure 4.6(a)) (Qin et al., 2016). The presence of metallic Au NPs can be distinguished by two peaks located at 83.9 and 87.6 eV with 3.7 eV spin energy separation (Figure 4.6(b)), assigned to the respective Au $4f_{7/2}$ and Au $4f_{5/2}$ (Lang et al., 2015). Figure 4.6(c) shows the Pd 3d XPS signals of higher binding energies at 340.8 and 335.7 eV which corresponds to Pd $3d_{5/2}$ and Pd $3d_{3/2}$, respectively. This confirmed the metallic form of the deposited Pd NPs. The other peaks centered at 343.3 and 338.4 eV was indexed to Pd^{2+} $3d_{5/2}$ and Pd^{2+} $3d_{3/2}$ ions which were contributed by Pd^{2+} ions adsorbed on the surface of g-C_3N_4 (Ni et al., 2016).

Table 4.1: Surface Elemental Concentration of C, N, O, Au, Ag and Pd Species from XPS Analysis for M/g-C_3N_4 (M=Pd, Ag and Au)

	Surface elemental concentration (atom %)						
Samples	**C1s**	**N1s**	**O1s**	**Cl2p**	**Au4f**	**Ag3d**	**Pd3d**
Au/g-C_3N_4	37.74	53.74	2.13	0.83	5.56	-	-
Ag/g-C_3N_4	32.99	50.74	3.91	0.00	-	12.35	-
Pd/g-C_3N_4	35.69	54.45	3.33	1.41	-	-	5.11

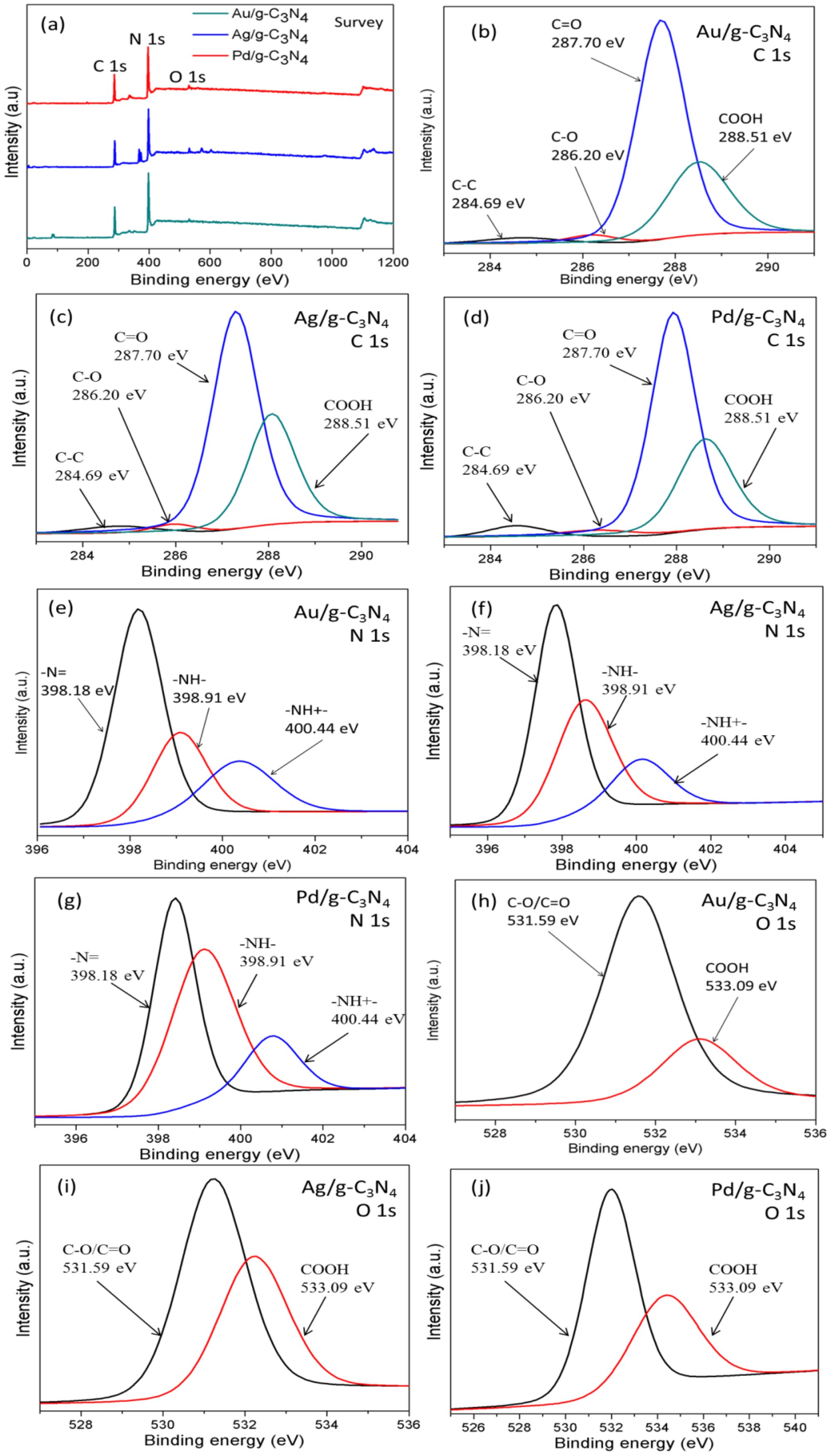

Figure 4.5: XPS Spectra (a) Survey (b-d) C 1s, (e-g) N 1s (h-j) O 1s of $M/g\text{-}C_3N_4$ (M=Pd, Ag and Au)

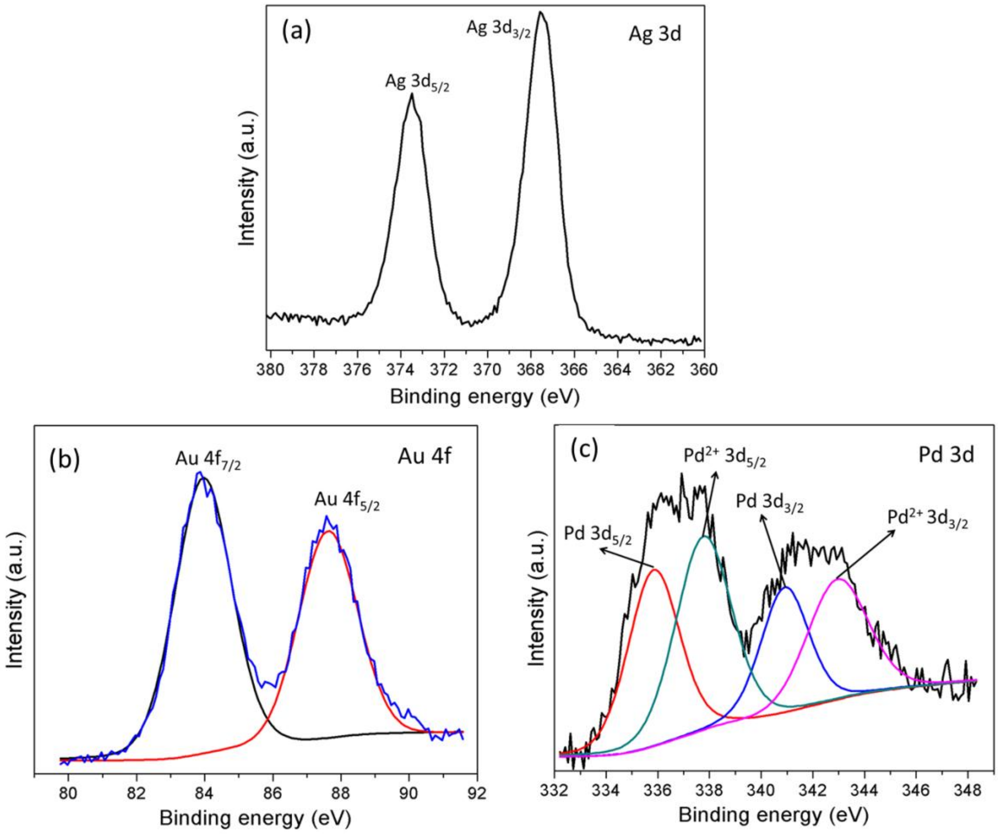

Figure 4.6: XPS Spectra of M/g-C_3N_4 (M=Pd, Ag and Au) (a) Ag 3d (b) Au 4f (c) Pd 3d

The UV–vis DRS were used to determine the visible light harvesting capability of the synthesized samples. Figure 4.7 shows the pure g-C_3N_4 displayed an expected absorption from the UV through the visible range up to 460 nm that ascribed to the optical band gap of g-C_3N_4 (Pawar et al., 2015b). These absorptions were attributed to the π–π* or n–π* electronic transitions in the conjugated aromatic s-heptazine ring system of g-C_3N_4 (Dai et al., 2013). Nevertheless, the absorption band of Au/g-C_3N_4 composite showed an obvious redshift towards the visible region. Further a hump at absorption band ~550 nm was observed after the deposition of Au NPs on the surface of g-C_3N_4. This was acknowledged to the LSPR effect delivered by Au NPs (Han et al., 2015). The presence of Au NPs had drastically created a disturbance on dielectric constant of the surrounding matrix and contributed for visible light absorption (Leong et al., 2014). Surprisingly, no hump was observed for both Pd/g-C_3N_4 and Ag/g-C_3N_4 and thus no significant LSPR effect was observed after the deposition of Pd and Ag NPs onto the surface of g-C_3N_4. The actual amount of noble metal's loading is determined by ICP-MS and shown in Table 4.2. The LSPR effect was not significant in Ag and Pd composites because of the lower loading amount of Pd (12.70 wt%) and Ag NPs (9.07 wt%) onto the surface of g-C_3N_4 compared to that of Au NPs (17.10 wt%). The LSPR effect increased with the loading amount of noble metal NPs (Yang et al., 2013). Similar observation was also reported in previous works by Jin et al. (2017). However, the band edge of both composites shifted towards visible region compared to that of pure g-C_3N_4. The absorption edge of g-C_3N_4 remain unchanged after coupling with noble metals NPs showing that depositing of noble metals NPs does not affect the band structure of g-C_3N_4 (Lu et al., 2017). This result is consistent with the XRD result in which the noble metal NPs only deposited onto the surface instead of intercalating into the lattice matrix of g-C_3N_4.

The band gap energy was obtained through the Tauc plot. It was determined by plotting $(F(R).\ h\nu)^{1/2}$ against hv, where Kubelka-Munck function F(R) is derive from equation as below:

$$F(R) = (1 - R)^2/2R \tag{4.2}$$

where hv is the photon energy and R is diffuse reflectance. The band gap energy of the synthesized photocatalysts was determined through the interception of the tangent of each curve to the photon energy (x-axis) as shown in Figure 4.8. As shown in Table 4.2, the band gap energy of g-C_3N_4 (2.95 eV) reduced significantly to 2.88 eV after modifying with Ag NPs.

While the band gap energy for both Au/g-C_3N_4 and Pd/g-C_3N_4 composites were 2.93 eV. The LSPR effect delivered by Au NPs did not contribute much in narrowing down the band gap energy.

Table 4.2: Weight Percentage of Noble Metals in the M/g-C_3N_4 (M=Ag, Au, and Pd) Determined by ICP-MS Analysis and Band Gap Energy of g-C_3N_4 and M/g-C_3N_4

Sample	Metal contents (wt%)	Band gap Energy (eV)
g-C_3N_4	-	2.95
Pd/g-C_3N_4	12.70	2.93
Ag/g-C_3N_4	9.07	2.88
Au/g-C_3N_4	17.10	2.93

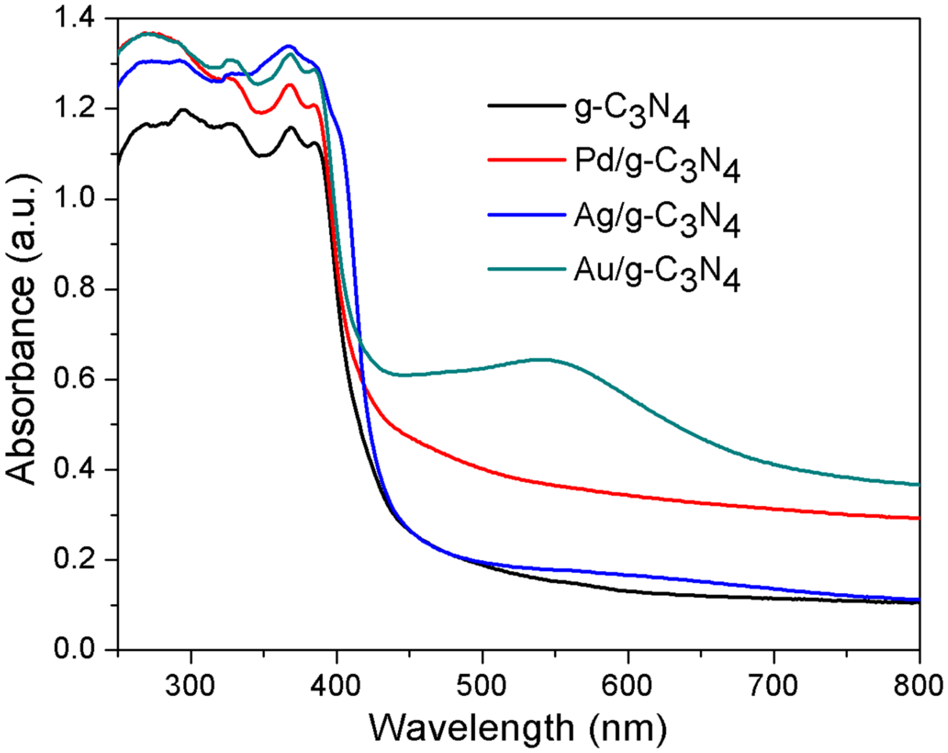

Figure 4.7: UV-Visible Absorption Spectra of g-C_3N_4 and M/g-C_3N_4 (M=Pd, Ag and Au)

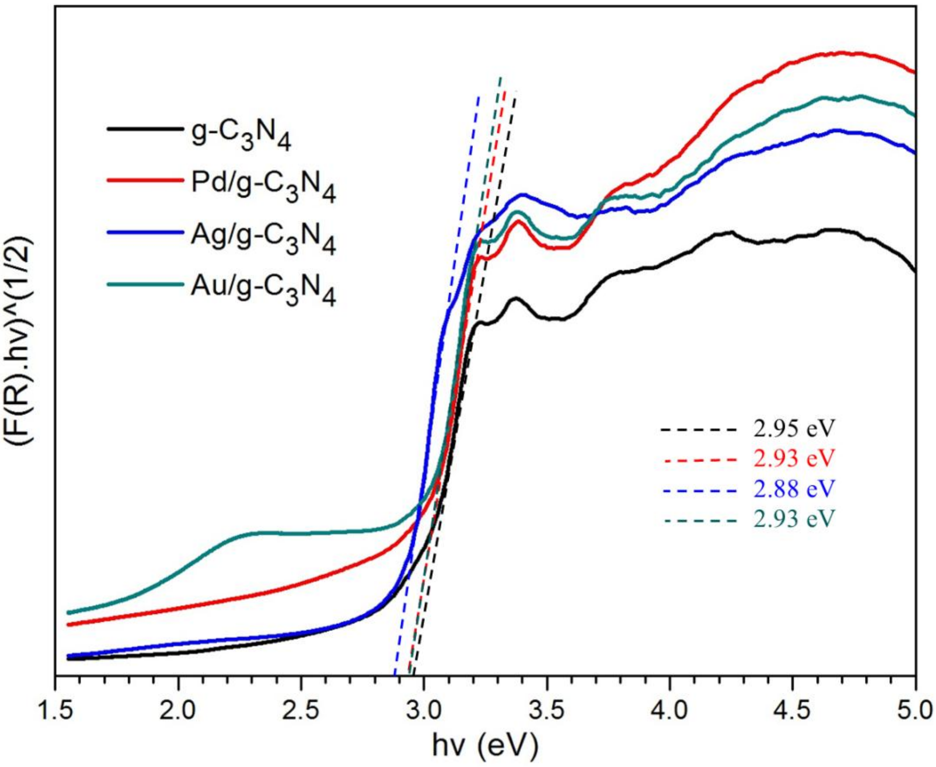

Figure 4.8: Tauc Plots of g-C_3N_4 and M/g-C_3N_4 (M=Pd, Ag and Au)

The photoluminescence (PL) emission analysis is to understand the recombination phenomenon of excited electron–hole pairs in the synthesized samples. In general, a lower PL intensity represents a lower recombination rate of electron–hole pairs. The PL spectra of g-C_3N_4, Pd/g-C_3N_4, Ag/g-C_3N_4 and Au/g-C_3N_4 are presented in Figure 4.9. The PL intensity was found in the following order: g-C_3N_4 > Au/g-C_3N_4 > Pd/g-C_3N_4 > Ag/g-C_3N_4. Notably, g-C_3N_4 showed the highest emission peak compared to other, indicating the fast recombination of photogenerated electron-hole pairs. On the contrary, both of Pd/g-C_3N_4 and Ag/g-C_3N_4 showed a more drastic quenched PL intensity relative to g-C_3N_4. Such observation shows a positive correlation with the previous results in Figure 4.4, confirming that the smaller sizes of Ag and Pd NPs prominently promoted a faster rate of electrons migration. Chang and co-workers showed that Pd NPs with average particle sizes 3 nm was uniformly distributed on g-C_3N_4 and effectively trapped the electron–hole pairs (Chang et al., 2013). Jiang and co-workers reported that Ag NPs with smaller particle size were highly dispersed on crystal plane of the photocatalyst and enhanced photocatalysis. The noble metals (M=Au, Ag and Pd) are able to trap the injected electrons from g-C_3N_4 through Schottky barrier at the interface of M/g-C_3N_4, leading to the acceleration of electrons migration (Jiang et al., 2014).

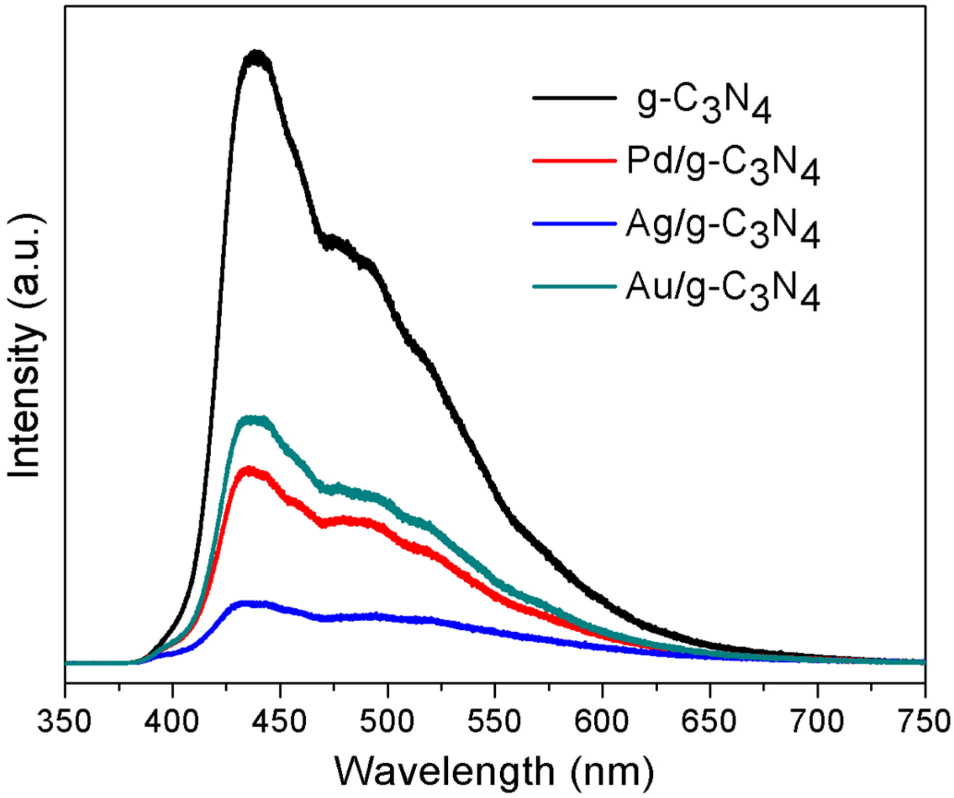

Figure 4.9: PL Spectra of g-C_3N_4 and M/g-C_3N_4 (M=Pd, Ag and Au)

The photocatalytic performances of all synthesized samples for BPA degradation were evaluated in aqueous solution under natural sunlight irradiation. As shown in Figure 4.10(a), there was almost no degradation was observed in the blank, clarifying that BPA was a poor photosensitizing compound and hardly degraded without the photocatalyst. All samples establish an adsorption-desorption equilibrium with less than 10% BPA concentration reduction during the pre-experiment in dark condition. The BPA pollutant was fully degraded by all the synthesized samples within 90 min. Both of Pd/g-C_3N_4 and Ag/g-C_3N_4 composites showed faster degradation rate of 70 min, followed by Au/g-C_3N_4 (80 min) and g-C_3N_4 (90 min). This shows that deposition of noble metals (M=Au, Ag and Pd) onto the surface of g-C_3N_4 successfully boosted the degradation efficiency of BPA compared to that of g-C_3N_4. The low band gap of pure g-C_3N_4 (2.95 eV) caused a moderately good photodegradation of BPA. The experimental degradation data were fitted into first order kinetic model to understand the reaction kinetics of BPA degradation process. The pseudo first-order reaction kinetics is expressed by Equation 4.3:

$$ln\left(\frac{C}{C_0}\right) = -kt \qquad (4.3)$$

where k represents the rate constant of first-order reaction (min^{-1}), C_0 and C are the BPA concentrations in the solution at time 0 and t min, respectively. The k values of all samples were fitted to first-order kinetic model in Figure 4.10(b). The k values of g-C_3N_4, Pd/g-C_3N_4, Ag/g-C_3N_4 and Au/g-C_3N_4 were 0.026, 0.041, 0.056, and 0.037 min^{-1} respectively (Figure 4.10(c)). For pure g-C_3N_4, the lower degradation rate was owing to the rapid recombination of electron-hole pairs. Among the samples, both of Ag/g-C_3N_4 and Pd/g-C_3N_4 achieved higher degradation rate which was 2.15 and 1.58 times higher than that of pure g-C_3N_4, respectively. This indicates that the smaller particle sizes of Ag NPs (7.5 nm) and Pd NPs (7.3 nm) over Au NPs (8.6 nm) greatly stimulated the electrons migration rate and promoted the separation of charge carriers which correlates well with its lower PL intensity (Figure 4.8). Furthermore, an optimum loading of noble metals NPs played a crucial rule in photoactivity enhancement. The actual loading of the noble metal NPs were 9.07, 12.70, and 17.10 wt% for Ag/g-C_3N_4, Pd/g-C_3N_4 and Au/g-C_3N_4 composites, respectively (Table 4.2). From the photodegradation results, the lowest loading of Ag NPs showed the best photodegradation efficiency while the highest loading of Au NPs showed the poorest efficiency. A higher loading of noble metals NPs could reduce the active sites of g-C_3N_4 for the degradation of BPA and thus decreasing the photodegradation efficiency (Zhang et al., 2014; Grabowska et al., 2016; Huang et al., 2018). The improvement of the photocatalytic performance in all composites proved that the deposition of noble metals induced the electron transfer from g-C_3N_4 to the trapping site of noble metals when the Schottky barrier formed at the interface of the composites. Interestingly, the LSPR effect of Au NPs in Au/g-C_3N_4 did not contribute much to the improvement of degradation efficiency. It is well known that the LSPR effect of Au NPs enabled its visible light utilization and also expedited the formation rate of charge carriers within the Au/g-C_3N_4 due to the intense local electromagnetic fields. However, in the meantime, the LSPR effect of Au NPs promoted the electrons transfer from surface plasmon (SP) state located at higher level to conduction band (CB) of g-C_3N_4 at lower level (Xue et al., 2015b). Hence, the amount of electrons trapped in Au NPs reduced and caused poor electron-hole pairs separation efficiency among the composites.

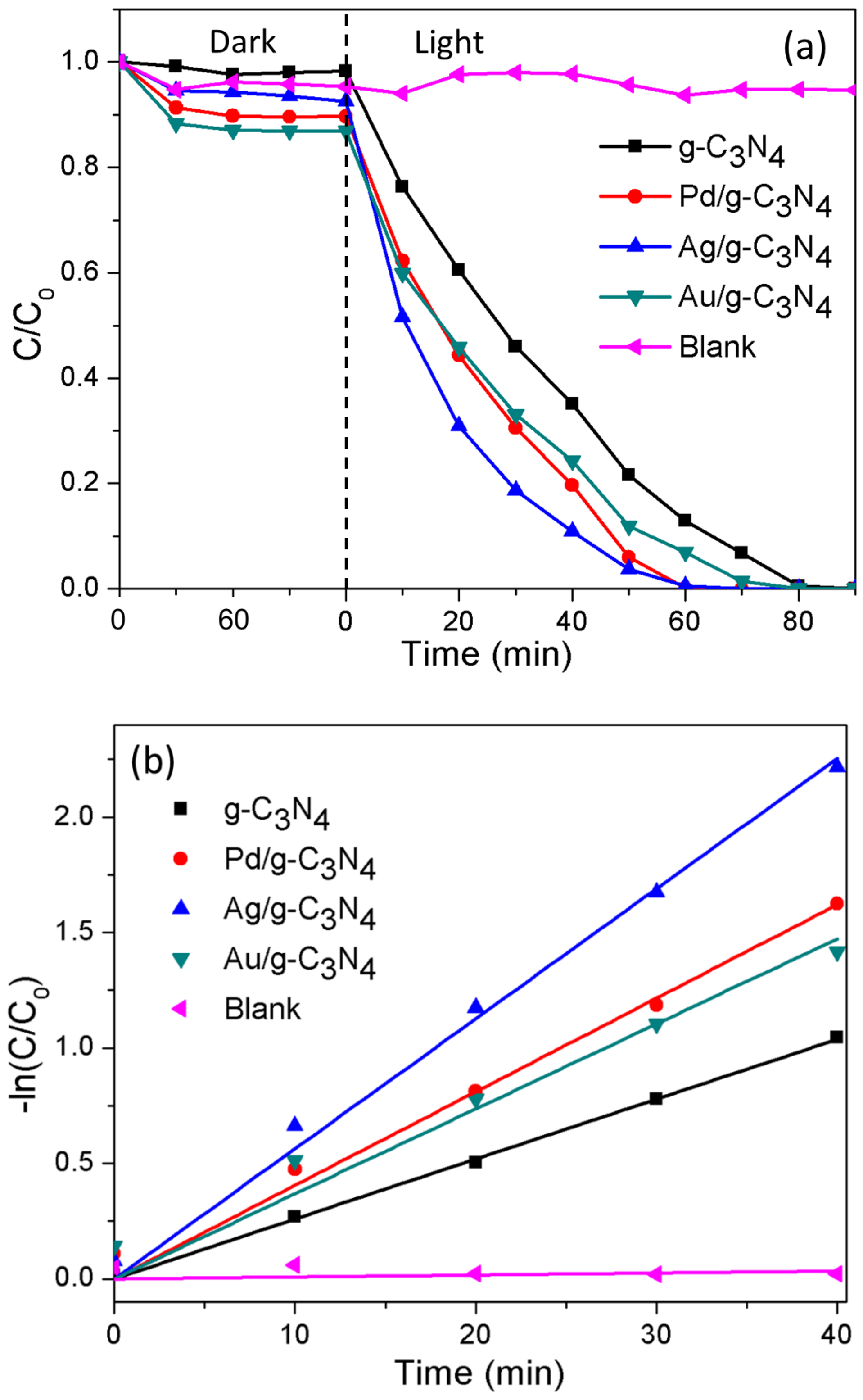
(a)
Dark
Light
C/C0
1.0
0.8
0.6
0.4
0.2
0.0
0
60
0
20
40
60
80
Time (min)
g-C3N4
Pd/g-C3N4
Ag/g-C3N4
Au/g-C3N4
Blank
(b)
-ln(C/C0)
2.0
1.5
1.0
0.5
0.0
0
10
20
30
40
Time (min)
g-C3N4
Pd/g-C3N4
Ag/g-C3N4
Au/g-C3N4
Blank

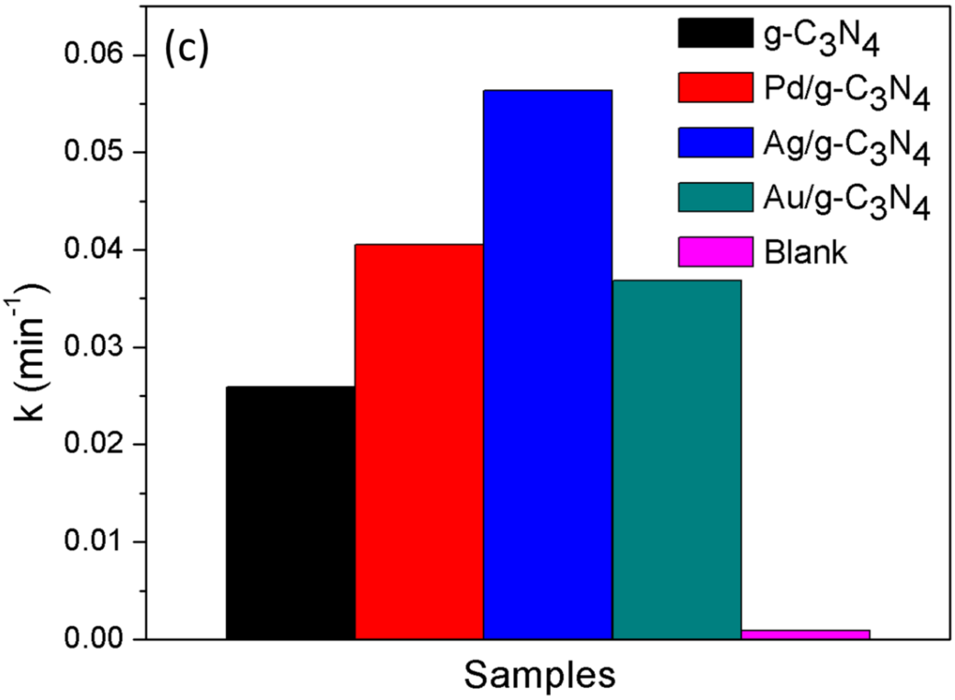

Figure 4.10: (a) Photocatalytic Degradation of BPA as a Function of Reaction Time (b) Fitted First Order Kinetic Plots for BPA Degradation (c) Apparent Rate Constant k

The effects of different scavengers for the photodegradation of BPA with Ag/g-C_3N_4 under natural sunlight irradiation are shown in Figure 4.11(a). The degradation of BPA was significantly suppressed by the addition of BQ and followed by EDTA-2Na$^+$, which implied that superoxide anion radicals ($^\bullet O_2^-$) was the main reactive species and holes (h^+) was the major reactive species in the Ag/g-C_3N_4 system. The degradation of BPA was not inhibited when IPA and DMSO were added during the experiment, implying that hydroxyl radicals ($^\bullet OH$) and electron (e^-) were not the main radical species in the degradation of BPA. The edge potential of the conduction band (CB) and the valence band (VB) of a photocatalyst at the point of zero charge were projected using the equations below:

$$E_{VB} = X - E_c + 0.5E_g \tag{4.4}$$

$$E_{CB} = E_{VB} - E_g \tag{4.5}$$

where E_{CB} and E_{VB} are the CB and VB edge potential respectively; E_g is the band gap energy of the semiconductor and E_c is the energy of free electrons on the hydrogen scale (≈4.5 eV vs NHE); X is the electronegativity of the semiconductor. The X value of g-C_3N_4 is 4.64 eV (Leong et al., 2015b) whereas the band gap energy of g-C_3N_4 is 2.95 eV (Table 4.2). The CB and VB of g-C_3N_4 were calculated to be −1.33 eV and 1.62 eV, respectively. The schematic diagram of degradation mechanism and electron transfer of Ag/g-C_3N_4 was illustrated in Figure 4.11(b). When the Ag/g-C_3N_4 was exposed under natural sunlight, electrons were excited from the VB of g-C_3N_4 to the CB, forming electron-hole pairs at each of VB and CB. As the aligned Fermi level (E_f) of Ag NPs is less negative than the CB of g-C_3N_4, the photogenerated electrons tended to transfer from CB of g-C_3N_4 to Ag NPs. Furthermore, the potential level of aligned Fermi level of Ag NPs was higher than the standard redox potential of $O_2/{}^{\bullet}O_2^-$ (−0.33 eV vs. NHE) (Leong et al., 2015b). Consequently, Ag NPs owned the reduction capability to reduce the O_2 absorbed on the surface to form ${}^{\bullet}O_2^-$ radicals *via* interfacial electrons transfer processes. However, the h^+ at VB of g-C_3N_4 cannot react with H_2O and OH^- to form ${}^{\bullet}OH$ radical caused by the potential energy of VB of g-C_3N_4 was more negative than the standard redox potential of $OH^-/{}^{\bullet}OH$ (+1.99 eV vs. NHE) and $H_2O/{}^{\bullet}OH$ (+2.38 eV vs. NHE) (Ni et al., 2016). Thus the h^+ directly involved in the degradation of BPA with the ${}^{\bullet}O_2^-$ radical, which matched well with the scavenger test results.

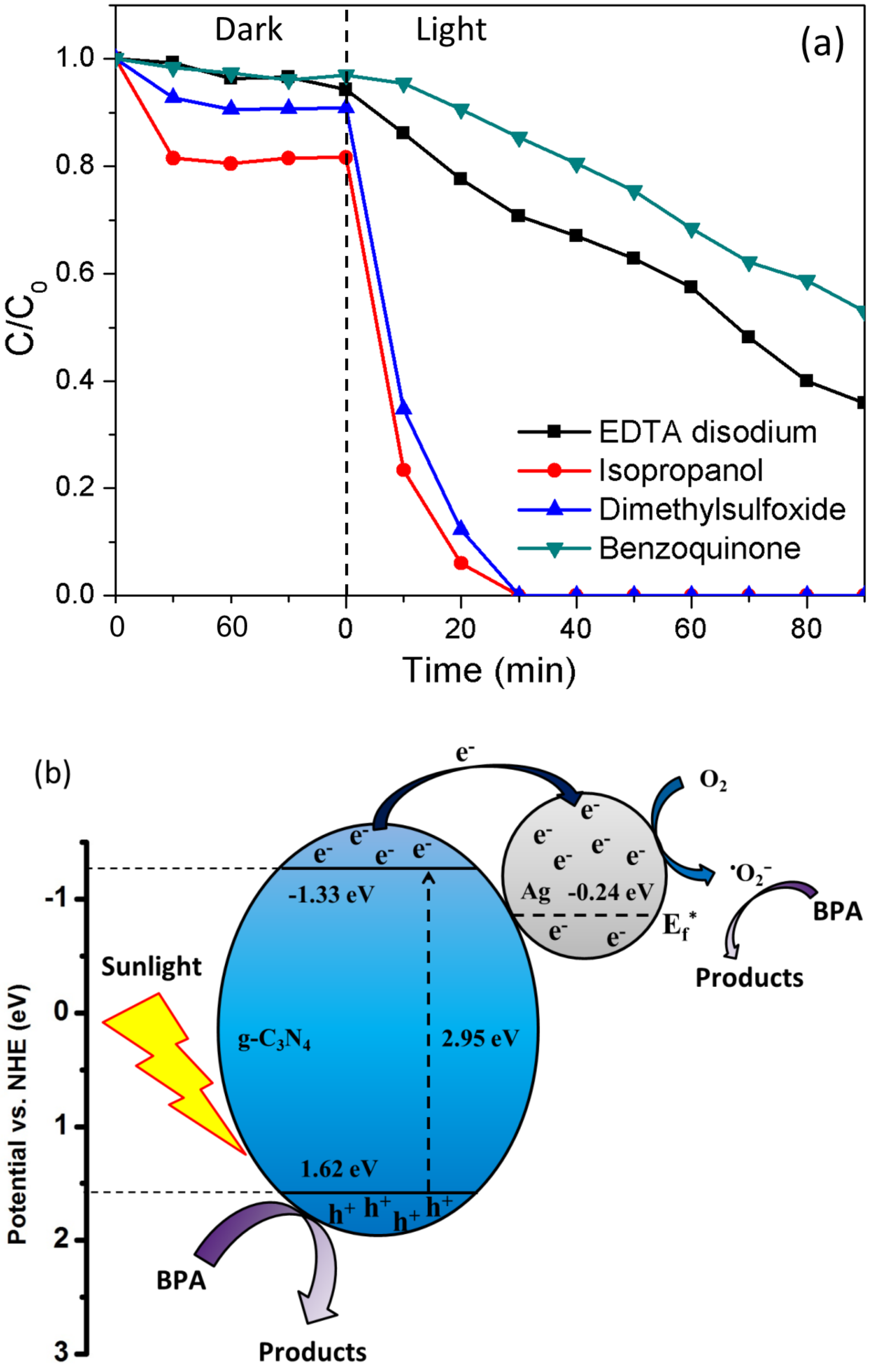

Figure 4.11: (a) Scavengers Test (b) Photocatalysis Mechanism of Ag/g-C_3N_4

Similarly, the experimental result from Figure 4.12(a) depicted that the h^+ and $^{\bullet}O_2^-$ radical were the main reactive species in the Au/g-C_3N_4 system. Compared with Ag/g-C_3N_4, its degradation mechanism and electron transfer route were different because of the LSPR effect owned by Au NPs. From the schematic diagram (Figure 4.12(b)), when the Au/g-C_3N_4 was irradiated to natural sunlight, the g-C_3N_4 was excited to produce electron-hole pairs. Meantime, electrons were excited from the below of Fermi level to the SP states of Au NPs upon LSPR-excitation, leaving the h^+ below the Fermi level (Xue et al., 2015b). Since the CB of g-C_3N_4 located lower than SP state of Au NPs, the electrons easily moved from Au NPs to the CB of g-C_3N_4 in the composite. This created two pathways for electrons injection and reduced the trapping capacity of Au NPs, thus its recombination rate of electron-hole pairs were higher than that of Ag/g-C_3N_4 and Pd/g-C_3N_4 as detailed in PL analysis. The electrons in CB of g-C_3N_4 and Au NPs reduced O_2 to form $^{\bullet}O_2^-$ radical as its potential level is higher than the standard redox potential of $O_2/^{\bullet}O_2^-$, while the h^+ left in Au NPs and g-C_3N_4 directly degraded BPA with the $^{\bullet}O_2^-$ radicals.

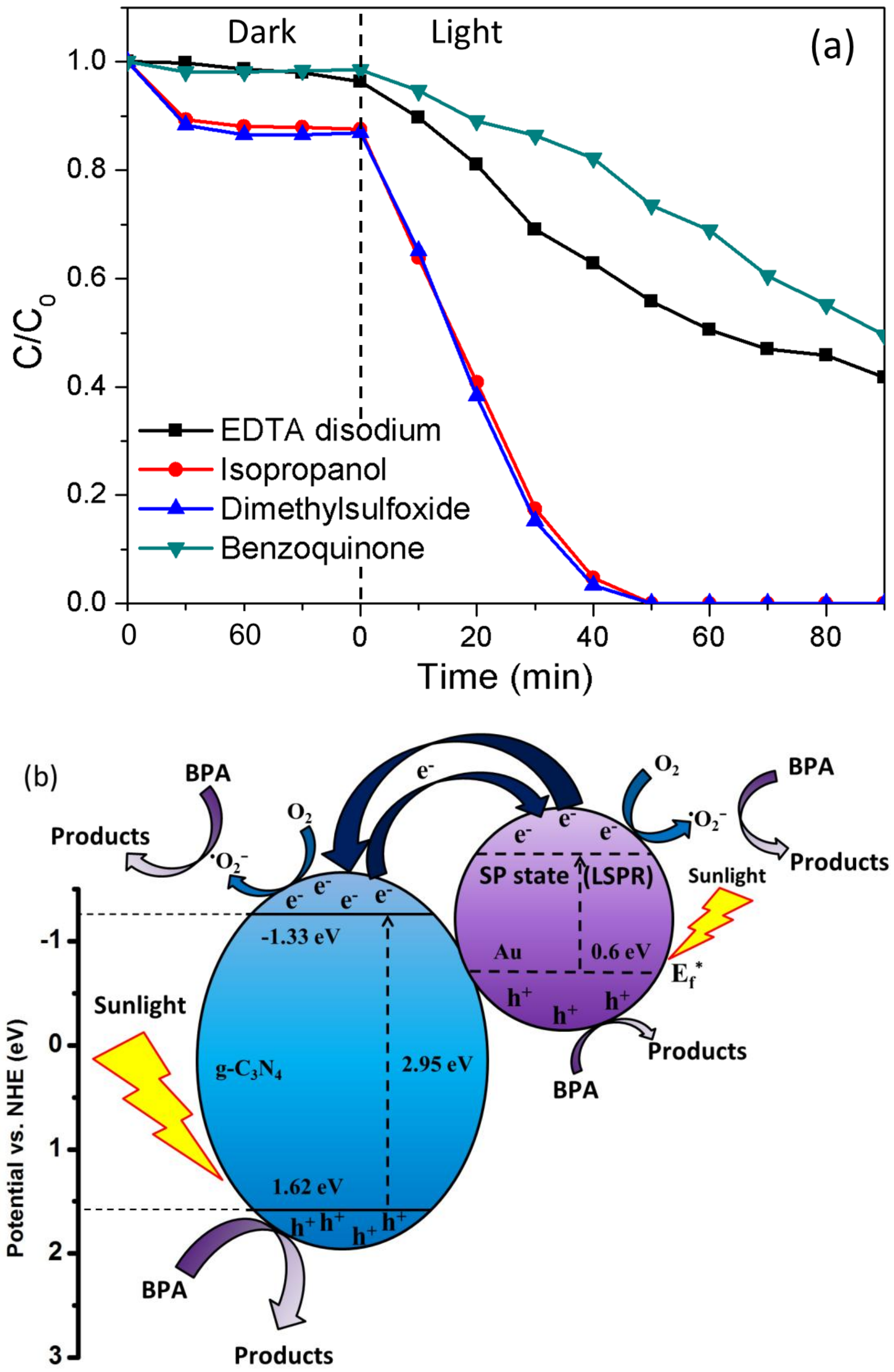

Figure 4.12: (a) Scavengers Test (b) Photocatalysis Mechanism of Au/g-C$_3$N$_4$

The reactive species of Pd/g-C_3N_4 were determined and shown in Figure 4.13(a). After adding EDTA-2Na^+ as a h^+ quencher to the solution, the degradation rate of BPA was 80%, indicating that h^+ was one of the minor reactive species during the BPA degradation process. Furthermore, the degradation rate of BPA was significantly decreased after adding BQ, showing that the $^{\bullet}O_2^-$ radical played a crucial role in the BPA oxidation process. These results clearly insinuate that the photocatalytic degradation of BPA over Pd/g-C_3N_4 was mainly driven by h^+ and $^{\bullet}O_2^-$ radical. The possible reaction mechanism is elucidating in Figure 4.13(b) according to the experimental results. Although the electrons transfer mechanism of Pd/g-C_3N_4 was almost similar with Ag/g-C_3N_4, the Fermi level of Pd NPs was more positive than Ag NPs. The Pd NPs owned higher work functions which gave rise to Schottky barrier and thus the greater Schottky barrier effect could store and shuttle the electrons from the CB of g-C_3N_4. This phenomenon helped to prevent the reverse electron flow from Pd NPs to g-C_3N_4, resulting in efficient electron-hole pairs separation. The Pd/g-C_3N_4 had the greatest Schottky barrier over the other composites but its degradation mechanism was limited by its low separation efficiency of electron-hole pairs. Overall, the photocatalytic reaction was mainly dependent on the size and loading amount of noble metal NPs since the trend of degradation efficiency was consistent with the PL intensity but not the visible light absorption properties.

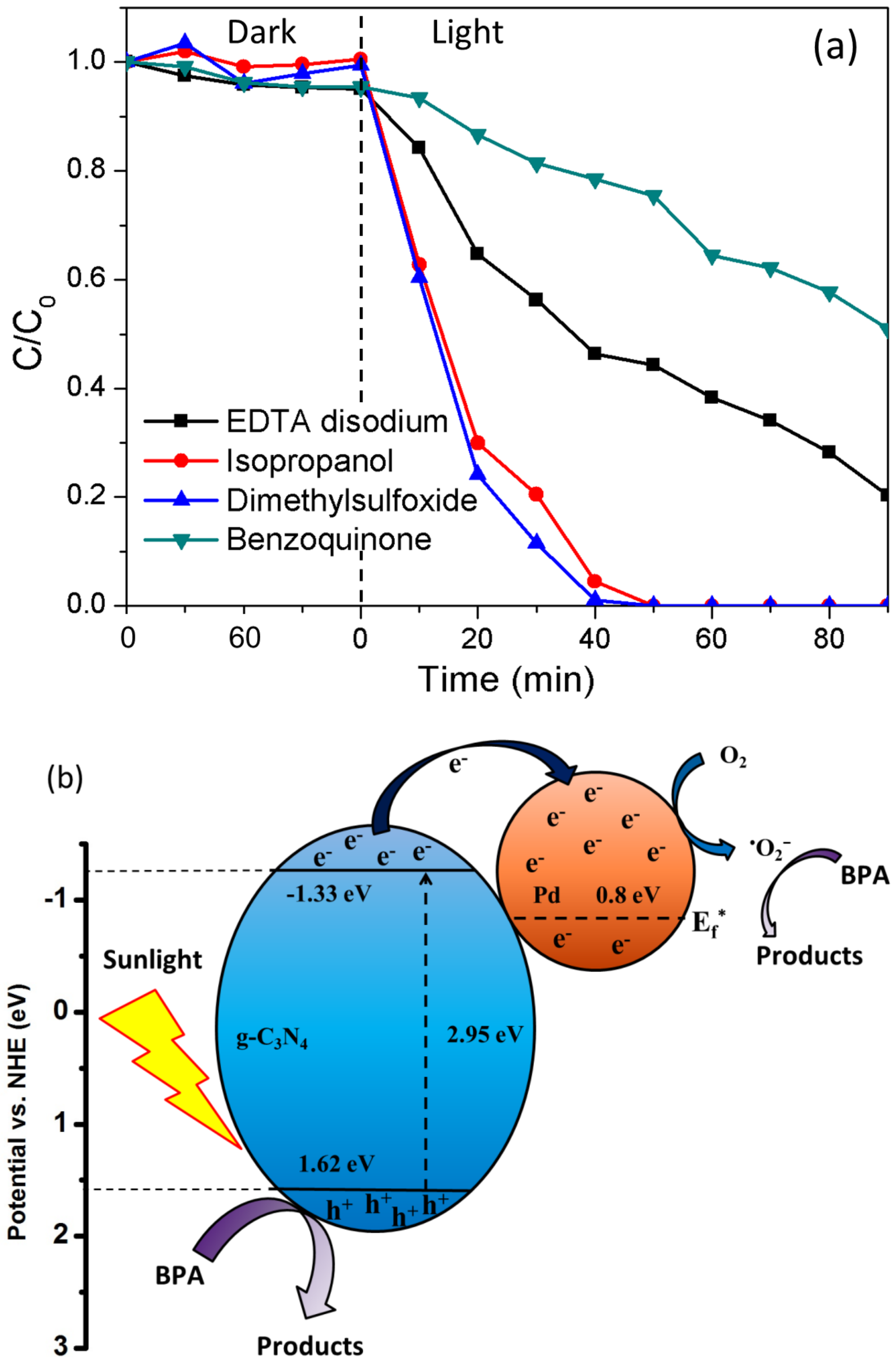

Figure 4.13: (a) Scavengers Test (b) Photocatalysis Mechanism of Pd/g-C_3N_4

A comparison study was also conducted between the present study and previous literature report. The results are shown in Table 4.3. In this present study, the M/g-C_3N_4 (M=Pd, Ag, Au) was able to degrade 100% of BPA within 80 min while Pd/g-C_3N_4 composite synthesized by Chang et al. (2013) studies need 360 min to degrade BPA completely. As reported by Zeng et al. (2017), the as-synthesized Pt/g-C_3N_4 exhibited photocatalytic degradation performance of 83% within 240 min which was lower and slower than this present study. It is concluded that, the present study had better photocatalytic degradation efficiency due to the optimum particle size of noble metal NPs. Compare with other low cost co-catalyst such as bismuth oxyhalides iodine (Bi_5O_7I), bismuth oxybromide (BiOBr) and carbon dots (CDs), the heterojunction photocatalyst g-C_3N_4/Bi_5O_7I reported by Liu et al. (2015) showed relatively low degradation efficiency which was 15%. While the combination of CDs and g-C_3N_4 showed promising results in degradation of organic pollutant. The CDs/g-C_3N_4 composites synthesized by Zhang et al. (2016) and Sim et al. (2018) shows 100% degradation efficiency within 200 and 90 min, respectively. These results motivate the use of CDs derived from green precursor as co-catalyst in second project to reduce the production cost of photocatalyst.

Table 4.3: Comparison Study of the Degradation of EDCs Using Other Photocatalysts

Composite	Organic Pollutant	Photocatalyst (mg)	Initial Concentration (mg/L)	Light Source	Duration (min)	Degradation Efficiency, %	Reference
Ag/g-C_3N_4	BPA	100	5	Sunlight	90	100.0	Present study
Au/g-C_3N_4	BPA	100	5	Sunlight	90	100.0	Present study
Pd/g-C_3N_4	BPA	100	5	Sunlight	90	100.0	Present study
Pt/g-C_3N_4	4-fluorophenol	100	10	Xe lamp	240	83.0	Zeng et al., 2017
Pd/g-C_3N_4	BPA	-	20	Xe lamp	360	100.0	Chang et al., 2013
g-C_3N_4/Bi_5O_7I	Phenol	50	0.94	Xe lamp	240	15.0	Liu et al., 2015
g-C_3N_4/BiOBr	BPA	20	10	Xe lamp	150	55.0	Xia et al., 2014
CDs/g-C_3N_4	Phenol	50	10	Xe lamp	200	100.0	Zhang et al., 2016
CDs/g-C_3N_4	BPA	100	5	Sunlight	90	100.0	Sim et al., 2018

4.2 Combining g-C_3N_4 with Carbon Dots

Considering the cost of noble metals despite of its promising performance, it provokes the idea to combine g-C_3N_4 with carbon dots (CDs) derived from water hyacinth for the photocatalytic degradation of 2,4-DCP under natural sunlight irradiation. A pre-experiment was carried out to evaluate the dosing range of CDs. Initially, the concentration of CDs was varied in the range of 0.6, 0.8 and 1.0 wt%. As shown in Figure 4.14, the degradation rate was almost the same among the composites which achieved 80% removal efficiency within 120 min while the degradation rate of pure g-C_3N_4 was 71.3%. The low dosage of CDs did not yield significant contribution to the improvement of degradation efficiency. From the results of pre-experiment, it was found that the optimum dosage trip at higher order and hence the aforementioned range was further moved to 20 and 40 wt% to study the significance of different weight percentage of CDs for the removal of 2,4-DCP. In this project, a scavenging test was also conducted to demonstrate the possible photocatalysis mechanisms. CDs are expected to act as a photosensitizer and electron trapper to extend the light harvesting region and the lifespan of electron-hole pairs. The incorporation of higher dosage CDs into g-C_3N_4 could improve the degradation efficiency towards the 2,4-DCP is hypothesized. In other to confirm the hypothesis, the CDs dosage was varied at range 0.6, 20 and 40 wt%.

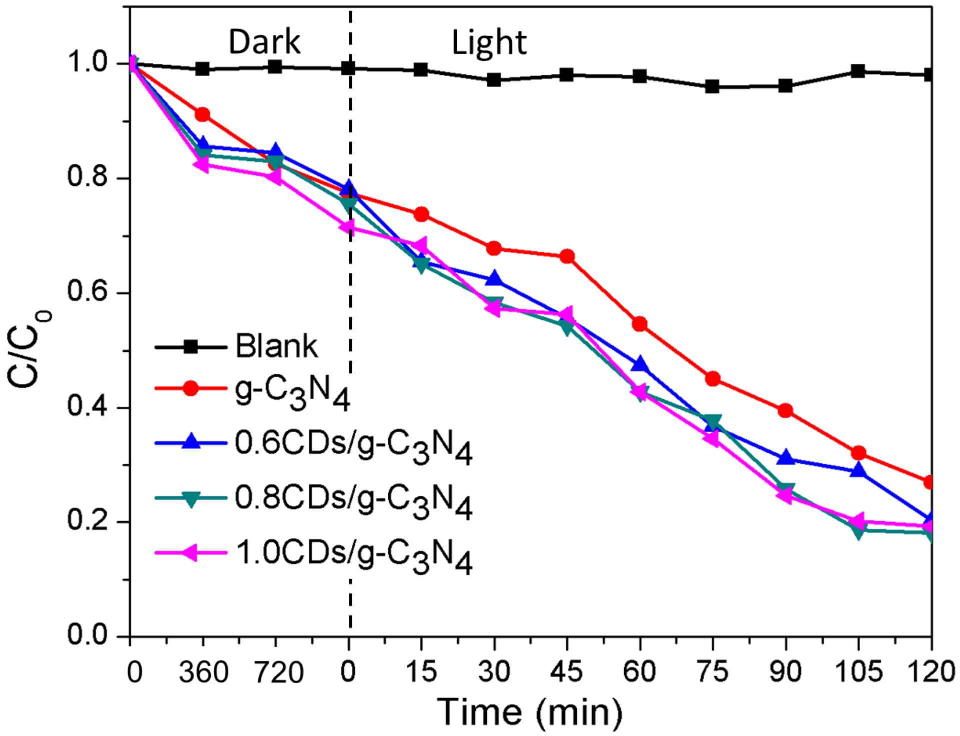

Figure 4.14: Photocatalytic Degradation of 2,4-DCP for Blank, g-C_3N_4, 0.6CDs/g-C_3N_4, 0.8CDs/g-C_3N_4 and 1.0CDs/g-C_3N_4

The morphological structure of g-C_3N_4 and CDs/g-C_3N_4 composites were determined by FESEM analysis. Figure 4.15(a) shows the agglomeration and irregular morphology with lamellar structure of g-C_3N_4 while the surface of CDs/g-C_3N_4 composites were more wrinkled and more porous with the increasing concentration of CDs as shown in Figure 4.15(b)-(d). A more packed and agglomerated morphological structure was observed after incorporating a lower concentration of CDs (0.6 wt%) into g-C_3N_4. This is due to the self-assembly process occurred during the hydrothermal treatment (Sim et al., 2018; Gao et al., 2012). When the concentration of CDs increased to higher range (20 and 40 wt%), the CDs/g-C_3N_4 composites displayed a loosen morphological structure. This result was consistent with our previous research reported that the increasing concentration of CDs can lower the clustering effect (Sim et al., 2018). The EDX was used to detect the elements of the

CDs/g-C_3N_4 composites. The existence of bulk g-C_3N_4 and CDs was confirmed by the detection of carbon (C), nitrogen (N) and oxygen (O) as shown in inset of Figure 4.15(b). The low concentration of O element was detected because of the oxygen reacted with g-C_3N_4 during the pyrolysis process. Figure 4.15(e) and (f) show the TEM and HRTEM image of 0.6CDs/g-C_3N_4, respectively. The small dark spots were observed which indicated that the CDs were uniformly distributed onto the surface of g-C_3N_4. Figure 4.15(f) further reveals the presence of CDs with the lattice fringes of 0.213 nm which correspond with to (1 0 0) in-plane lattice spacing of graphene (Li et al., 2016; Du et al., 2015; Zhang et al., 2015). From Figure 4.16, the average particle size of the CDs was found to be 3.1 nm. The particle size ranged from 1.2 nm to 4.9 nm, proving that the nanosized CDs were successfully prepared. Table 4.4 shows the BET surface area of as-prepared samples. The BET specific surface area of g-C_3N_4, 0.6CDs/g-C_3N_4, 20CDs/g-C_3N_4 and 40CDs/g-C_3N_4 were 77, 76, 65 and 159 m^2/g, respectively. The 40CDs/g-C_3N_4 composite shows the largest specific surface area among the samples. Theoretically it will enhance the photocatalytic activity since the large specific surface area in heterojunction could increase the number of active sites (Guo et al., 2016). This results correlated well with the FESEM results in which the clustering effect occurred at lower concentration of CDs while loosen structure was observed at higher concentration of CDs.

Table 4.4: BET Surface Area of the Prepared Samples

Sample	BET Surface Area (m^2/g)	Bandgap Energy (eV)
g-C_3N_4	77.42	2.95
0.6CDs/g-C_3N_4	76.45	2.94
20CDs/g-C_3N_4	65.07	2.92
40CDs/g-C_3N_4	168.98	2.92

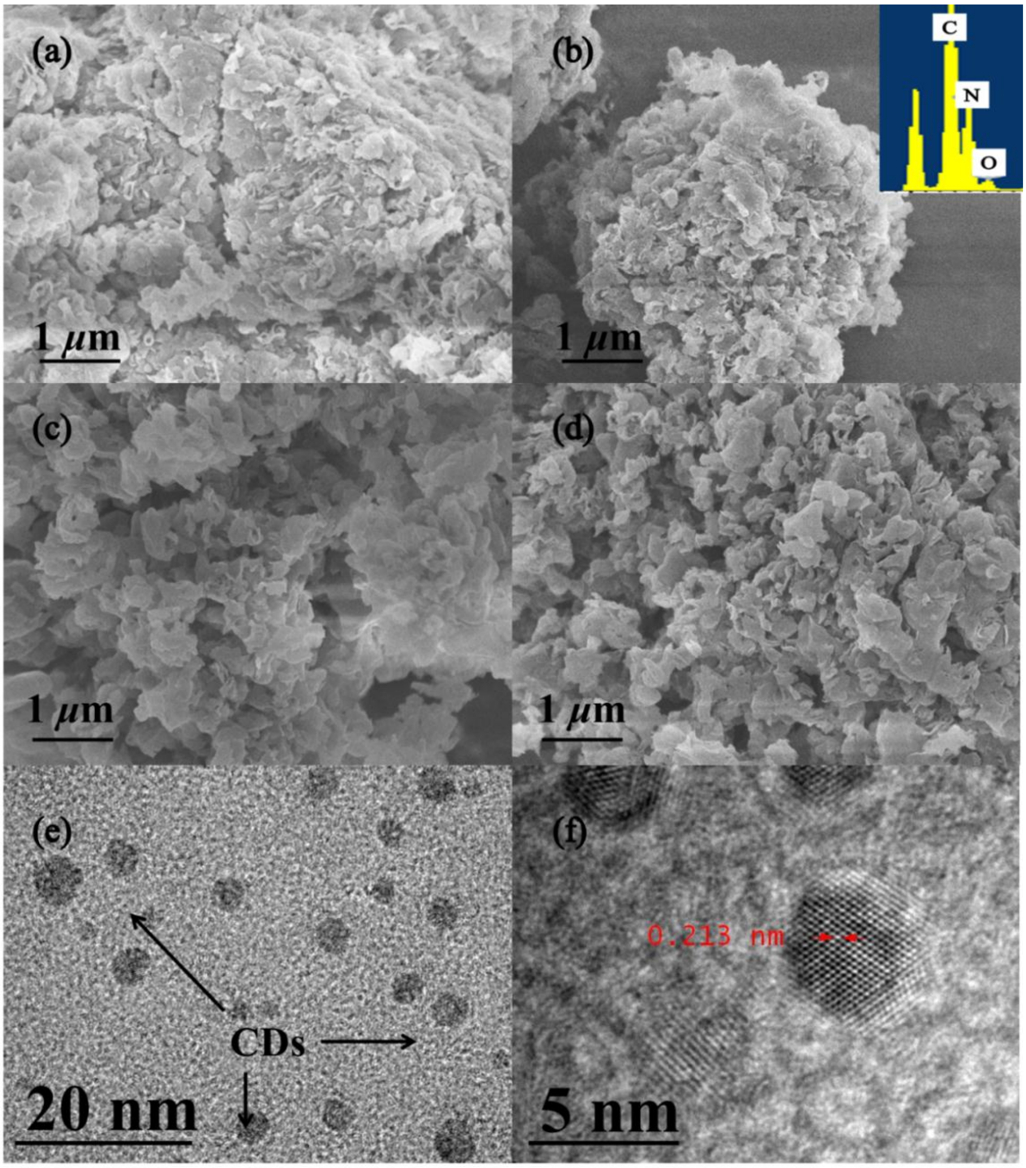

Figure 4.15: FESEM Images of (a) g-C_3N_4 (b) 0.6CD/g-C_3N_4 (c) 20CD/g-C_3N_4 and (d) 40CD/g-C_3N_4 Composites (e) TEM Image (f) HRTEM Image of 0.6CD/g-C_3N_4. The Inset of (b) Shows the Energy-Dispersive X-ray Spectroscopy (EDS) Results of 0.6CD/g-C_3N_4

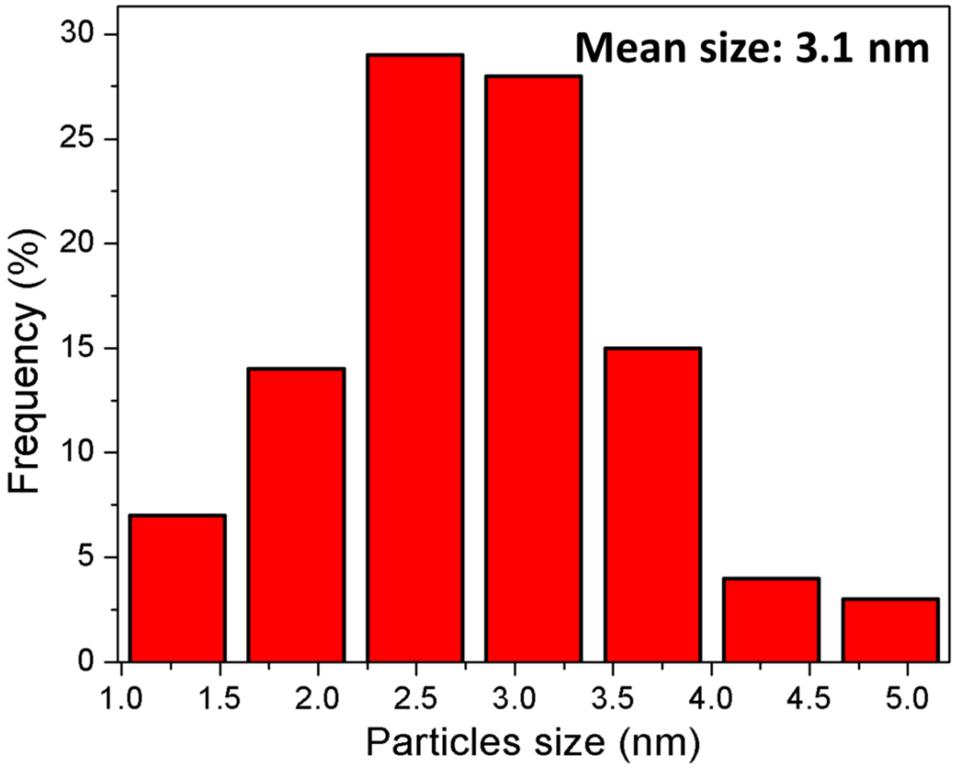

Figure 4.16: Particle Size Distribution of CDs

XRD patterns of CDs and all CDs/g-C_3N_4 composites were presented in Figure 4.17. The two obvious diffraction peaks were found in all composites indexed to the crystal structure of pristine g-C_3N_4. The strong peak at 27º indexed as (0 0 2) was ascribed to the interlayer stacking of aromatic segments with interplanar distance of 0.32 nm. The weak diffraction peak at 12.8° indexed as (1 0 0) corresponded to in-plane structural packing motif of tri-s-triazine (Lu et al., 2016). After incorporating 20 and 40 wt% of CDs into the g-C_3N_4, the diffraction peak shifted from 27.6º to 27.9º because the crystal lattice of g-C_3N_4 distorted with high loading of CDs. This indicates the CDs were successfully intercalated into the matrix instead of being dispersed on the surface of g-C_3N_4 (Fang et al., 2016). However, the low concentration of CDs in 0.6CDs/g-C_3N_4 did not exert notable alteration to the host structure. The intensity of both diffraction peaks at 12.8° and 27º decreased with the increasing loading amount of CDs. This reveals that the existence of CDs inhibited the polymerization of dicyandiamide and the stacking (crystallization) of g-C_3N_4 sheets (Fang et al., 2016). The diffraction peaks of CDs were not captured in all composites because the diffraction peak at around 27° was similar to the characteristic diffraction peak of graphite planes (0 0 2) (Das et al., 2017). The inset of Figure 4.16 shows a broad (0 0 2) diffraction peak of the CDs at 25° which was attributed to highly disordered carbon atoms and graphitic structure, conforming the amorphous character and graphite-like structure of the CDs (Zhu et al., 2013).

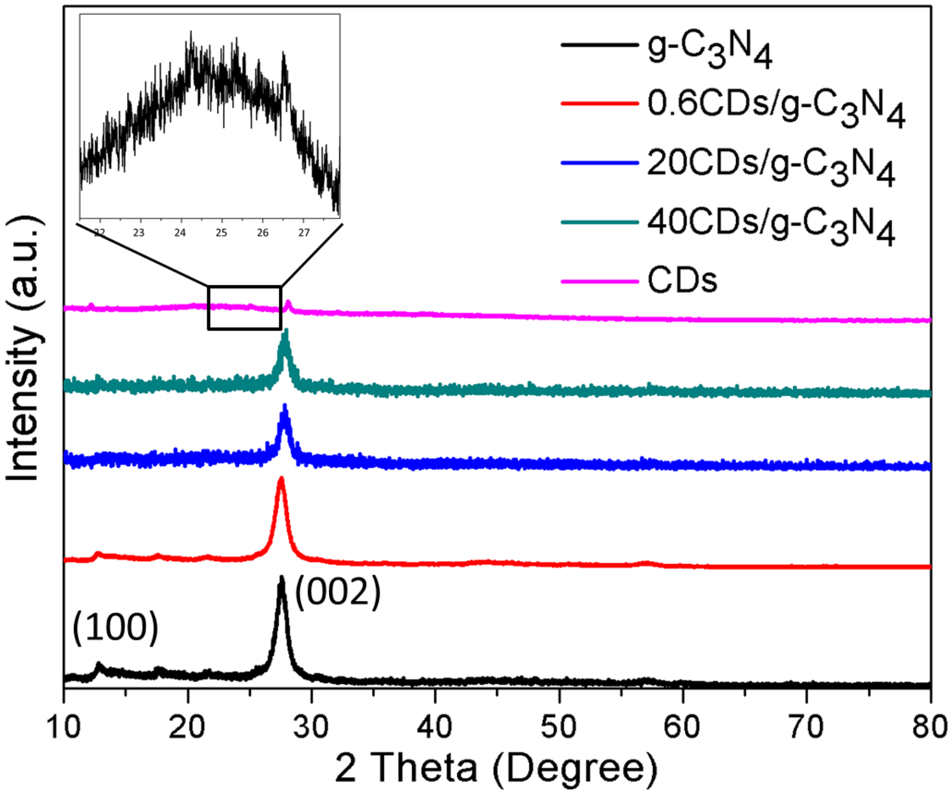

Figure 4.17: The XRD Patterns of CDs, g-C_3N_4, 0.6CD/g-C_3N_4, 20CD/g-C_3N_4 and 40CD/g-C_3N_4. The Inset Shows the Enlarged XRD Pattern of CDs

The functional groups in the CDs and composites were identified by using FTIR spectroscopy and shown in Figure 4.18. For the CDs, a broad peak observed at around 3400 cm^{-1} was accredited to the stretching vibration mode of O−H, while a small peak at 2932 cm^{-1} corresponded to the stretching vibration mode of C−H. The band at 1616 cm^{-1} corresponded to C=O stretching of carbonyl groups. Both of vibrational bands at 1052 and 1112 cm^{-1} were credited to the stretching vibrations of C−O−C. Comparable results were also achieved by other researchers (Sim et al., 2018; Sahu et al., 2012). For g-C_3N_4, several absorption peaks observed between the range of 1241 cm^{-1} and 1630 cm^{-1} were assigned to the stretching of sp^3 C−N, and sp^2 C=N that corresponded to the characteristic stretching modes of CN heterocycles (Jian et al., 2016). The sharp peak at 808 cm^{-1} was ascribed to the breathing mode of triazine units of g-C_3N_4 (Wang et al., 2017). The wide peaks in the range of 3000−3400 cm^{-1} were assigned to the stretching vibration modes of N−H and O−H of g-C_3N_4 (Guo et al., 2017). Similar CN heterocycles and triazine units of g-C_3N_4 absorption peak were detected for all CD/g-C_3N_4 composites as a result of the low CDs loading amount. The strong absorptions peak of g-C_3N_4 covered the weak absorptions of CDs.

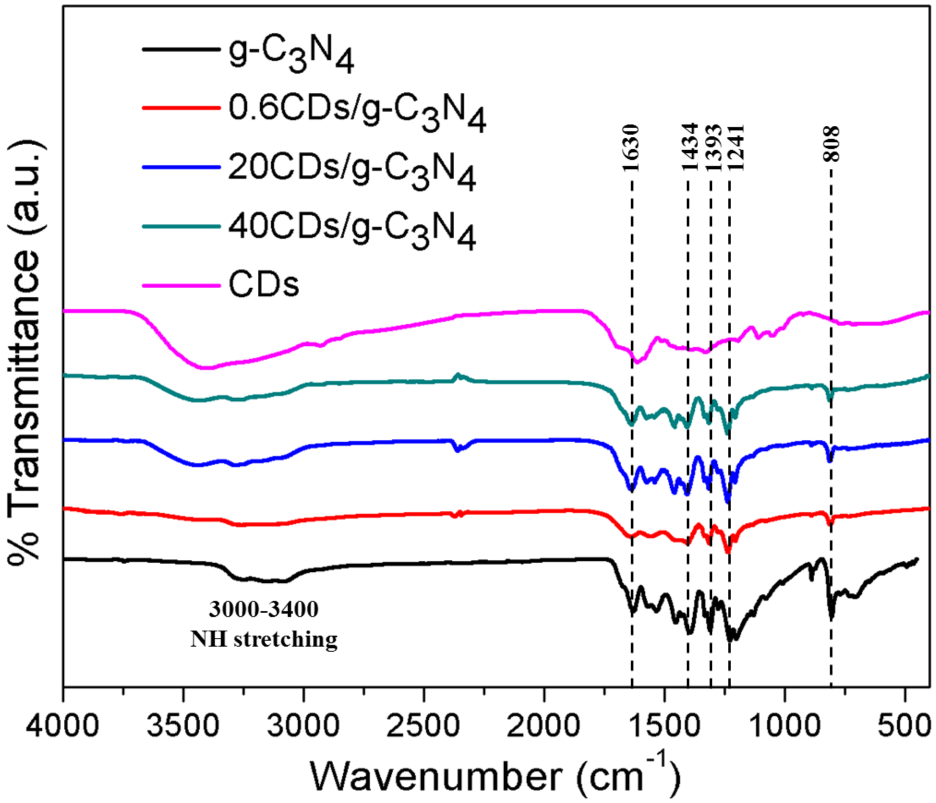

Figure 4.18: FTIR Spectra of g-C_3N_4, 0.6CD/g-C_3N_4, 20CD/g-C_3N_4 and 40CD/g-C_3N_4

The chemical state and chemical composition of 0.6CDs/g-C_3N_4 were studied by XPS. Figure 4.19 shows the narrow scan of XPS spectra and confirmed the existence of C, N and O in the composite. From Figure 4.19(a), the C1s peak was deconvoluted into three peaks at 284.77 eV, 287.97 eV and 288.83 eV which corresponded to graphitic carbon (C-C), amine (C=N) and sp^2 carbon (N-C=N) (Wang et al., 2017). For the N1s spectrum in Figure 4.19(b), the main peak observed at 398.51 eV was ascribed to CN=C coordination which originated from the sp^2-bonded N in triazine rings. Meanwhile the other two weak peaks detected at binding energy of 399.80 eV and 400.77 eV were ascribed to tertiary (N-$(C)_3$) and amino functional groups (C-N-H) (Guo et al., 2017). The only O 1s peak at 531.91 eV was ascribed to the absorbed water (Figure 4.19(c)) (Lu et al., 2016).

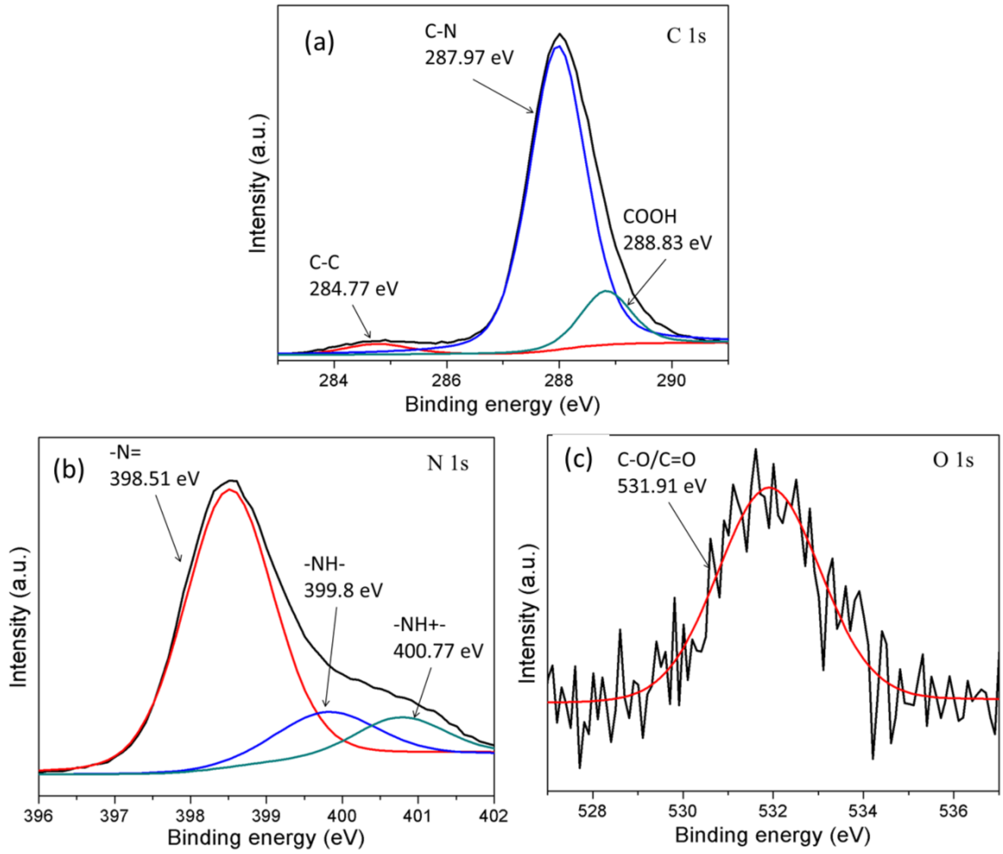

Figure 4.19: XPS Spectra of 0.6CDs/g-C_3N_4 (a) C1s (b) N1s and (c) O1s

The optical properties of water hyacinth (WH) derived CDs solution was investigated by UV-Vis absorption and photoluminescence spectrophotometer. Figure 4.20 demonstrations the UV–vis absorptions of aqueous CDs was in the range between 200 nm and 800 nm. The noticeable peak at 300 nm was attributed to the n-π* transitions of C=O and π-π* transition of C=C (Xu et al., 2015). The inset of Figure 4.20 shows the optical properties of synthesized CDs solution, a blue-green fluorescence was emitted under the UV light irradiation at 365 nm. The excitation-dependent PL spectra of WH derived CDs solution was shown in Figure 4.21. The ideal spectrum that induced the PL properties of CDs solution was studied by varying the excitation wavelength from 320 to 540 nm. The fluorescence emission of CDs exhibited a wide peak from the UV (380 nm) to visible spectrum (500 nm).

The CDs showed a strong emission peak when excited by the light with wavelength from 320 to 380 nm. The emission spectrum was red-shifted with decreasing intensity as the excitation wavelength amplified from 400 to 540 nm. The emission peak was not perceived when the excitation wavelength exceeded 540 nm. This means that the synthesized CDs did not acquire the upconverted photoluminescence (UCPL) properties that could convert the absorbed NIR light to shorter wavelength for the occurrence of electron excitation at low energy input. The foundation of the photoluminescence properties of CDs is not completely understood but they are normally influenced by the size distribution of CDs, structure of nanoparticles and different distribution of emissive traps sites (Chen et al., 2016). From the previous researches, there are limited report on CDs and graphene quantum dots (GQDs) that acquired UCPL properties. Some researchers claimed that the regularly cited UCPL properties might initiate from the standard fluorescence excited by the leaking component in the monochromater of the fluorescence spectrophotometer (Wen et al., 2014).

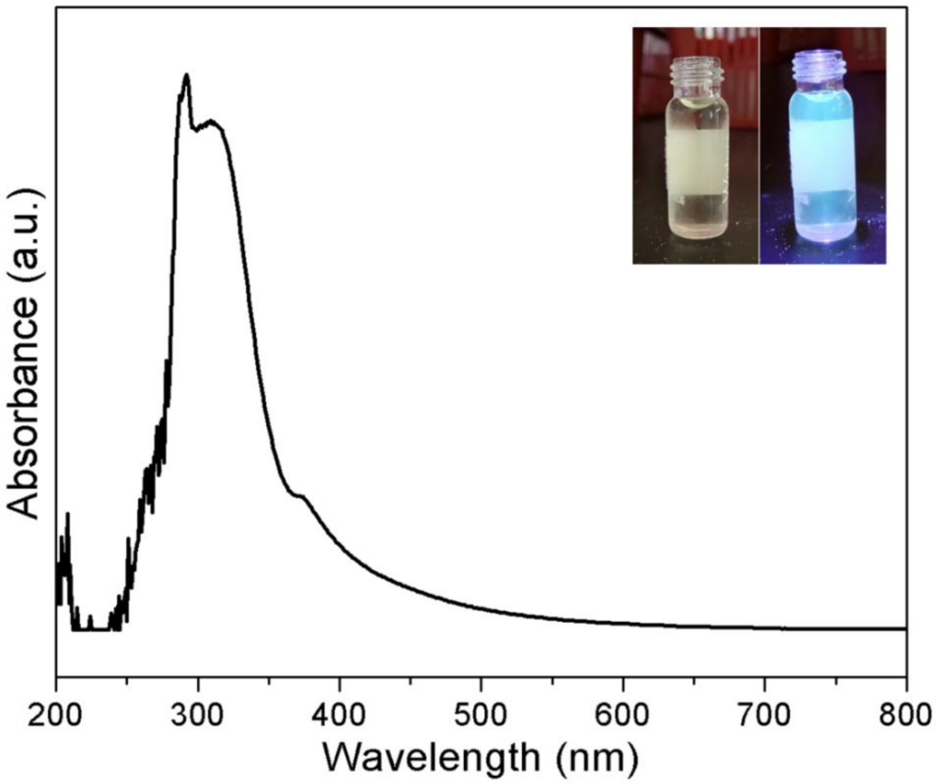

Figure 4.20: The Absorption Spectrum of Carbon Dots Solution. Inset Shows Fluorescence of CDs under Daylight (Left) and UV Light Irradiation at 365 nm (Right)

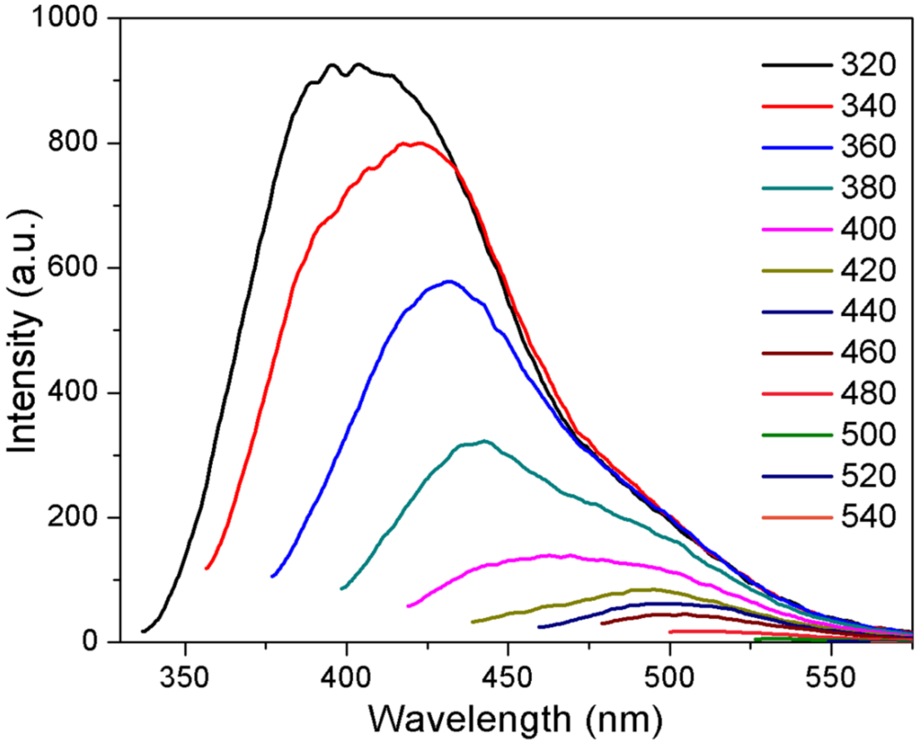

Figure 4.21: The Emission Wavelength of CDs Solution at Different Excitation Spectrum

The light absorption properties of the synthesized samples were determined by UV-vis DRS analysis. The absorption peaks of all CDs/g-C_3N_4 composites red shifted towards higher wavelength in visible and NIR region. When the concentration of CDs increased, the intensity of shoulder peak also increased and the absorption edge gradually red shifted towards longer wavelength. The shoulder peak was triggered by the light absorption of CDs and the red shift of absorption edge was attributable to the interfacial interaction between the CDs and g-C_3N_4 (Wang et al., 2017). Although it is proved that CDs were able to absorb NIR light, the photon energy of NIR light is too low to induce photoexcitation. Therefore, UCPL properties of CDs enabled the conversion of low energy NIR light to visible and UV light with higher energy to excite the electrons. Since the UCPL properties are not detected in CDs (Figure 4.21), the photoexcitation by NIR light cannot be realized in the composites. In this context, CDs played a vital role to sensitize g-C_3N_4 to harvest more visible light instead of NIR light to excite more electrons for the improvement of photocatalytic performance.

The band gap energy was obtained through the Tauc plot. It was determined by plotting $(F(R).\ h\nu)^{1/2}$ against hν, where Kubelka-Munck function F(R) is derived from following equation:

$$\mathrm{F(R)} = (1 - \mathrm{R})^2/2\mathrm{R} \qquad (4.6)$$

where hν is the photon energy and R is diffuse reflectance. Figure 4.23 shows the interception of the tangent of each curve to the photon energy (x-axis) to determine the band gap energy of the synthesized samples. The obtained band gap energy was corresponded to the optical shift in Figure 4.22, where the lower shift had a wider band gap while the higher shift toward the visible light region obtained a narrower band gap. As shown in Table 4.4 (pg. 86), the band gap energy of g-C_3N_4 (2.95 eV) decreased significantly from 2.95 eV to 2.92 eV after modifying with CDs at higher percentage.

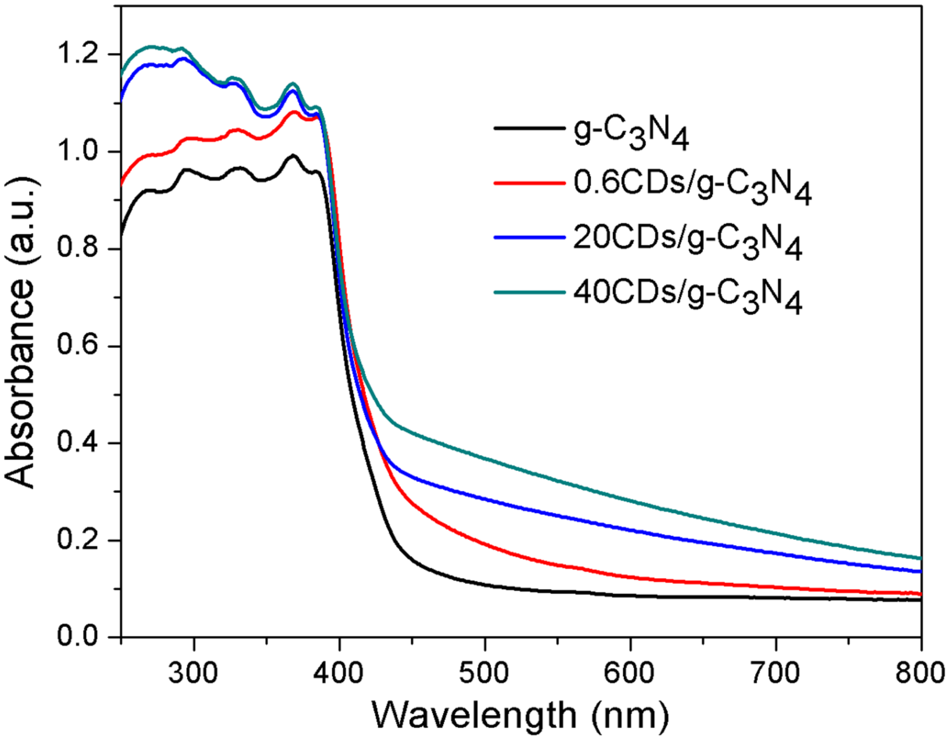

Figure 4.22: UV-visible Diffuse Reflectance Spectra of g-C_3N_4, 0.6CDs/g-C_3N_4, 20CDs/g-C_3N_4 and 40CDs/g-C_3N_4

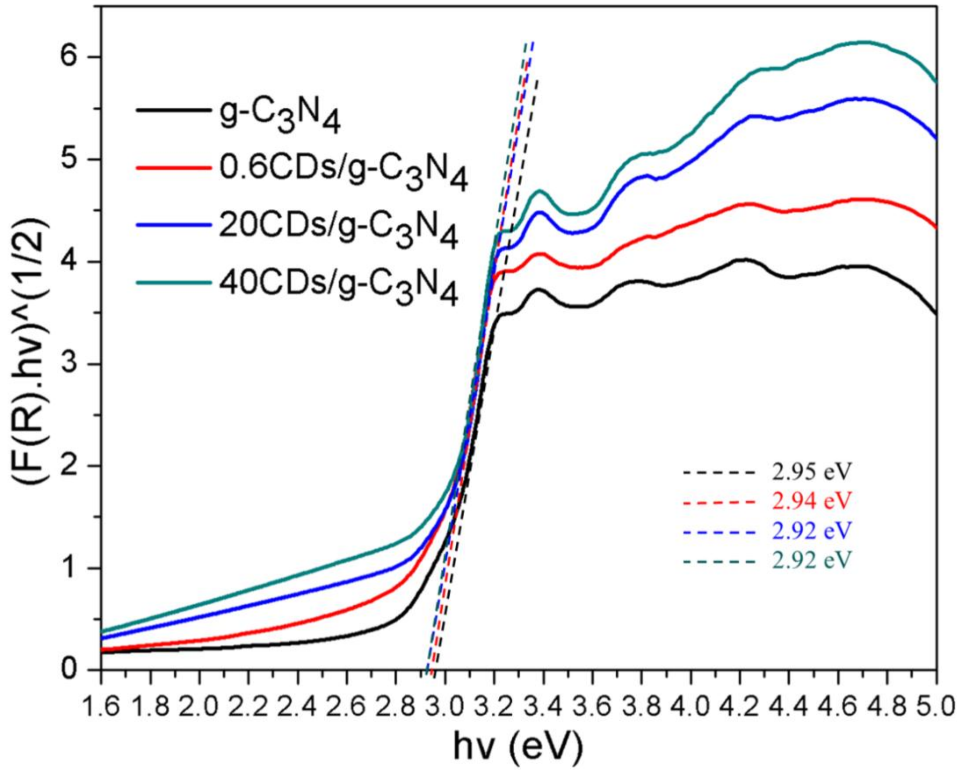

Figure 4.23: Tauc Plots of g-C_3N_4, 0.6CDs/g-C_3N_4, 20CDs/g-C_3N_4 and 40CDs/g-C_3N_4

Time-resolved PL (TRPL) spectra shown in Figure 4.24 were adopted to study the dynamic electron transfer process of the samples. In general, the longer lifetime is credited to an effective electron-hole pairs separation, while the shorter lifetime is attributed to the rapid recombination of the electron-hole pairs. Table 4.5 shows all the fitted parameters. The charge-carrier lifetimes of these composites increased in the following order: g-C_3N_4 < 40CDs/g-C_3N_4 < 0.6CDs/g-C_3N_4 < 20CDs/g-C_3N_4. Among the samples, 20CDs/g-C_3N_4 exhibited the longest charge-carrier lifetime with 4.897 ns while g-C_3N_4 possessed the shortest charge carrier lifetime of 1.724 ns. This reveals that the 20CDs/g-C_3N_4 achieved the highest electron-hole pairs separation efficiency compared to the others. When the CDs were incorporated into g-C_3N_4, CDs could function as the reservoir to trap the excited electron due to the surface junction between both semiconductors that could enhance the separation of electron-hole pairs. This could result in the enhancement of photocatalytic activity because more electrons and holes will involve in the redox reactions to produce strong oxidizing agents for the degradation of targeted pollutant. However, the highest dosage of CDs in 40CDs/g-C_3N_4 increased the electron-hole pairs recombination. The enlargement of CDs coverage formed the trap states at the interface between CDs and g-C_3N_4, and thus fewer electrons fill in the interfacial trap states. This could lead to the increase of trapping events and decelerate the electron transport (Sim et al., 2018; Maloney et al., 2016). A similar observation was reported by Fang and co-workers. They claimed that excessive dosage of CDs will act as recombination centers and lower down the electron-hole pairs separation efficiency (Fang et al., 2015).

Table 4.5: Fitted Parameters in TRPL Analysis

Sample	T_1	T_2	T_3	B_1	B_2	B_3	τ (ns)
g-C_3N_4	0.9159	3.1388	12.0499	0.006	0.001	0	1.724
0.6CDs/g-C_3N_4	0.3205	1.4498	5.4237	0.002	0.004	0.002	3.901
20CDs/g-C_3N_4	0.0434	1.8755	7.4585	0.01	0.003	0.001	4.897
40CDs/g-C_3N_4	0.0497	1.1089	5.3071	0.019	0.006	0.001	2.758

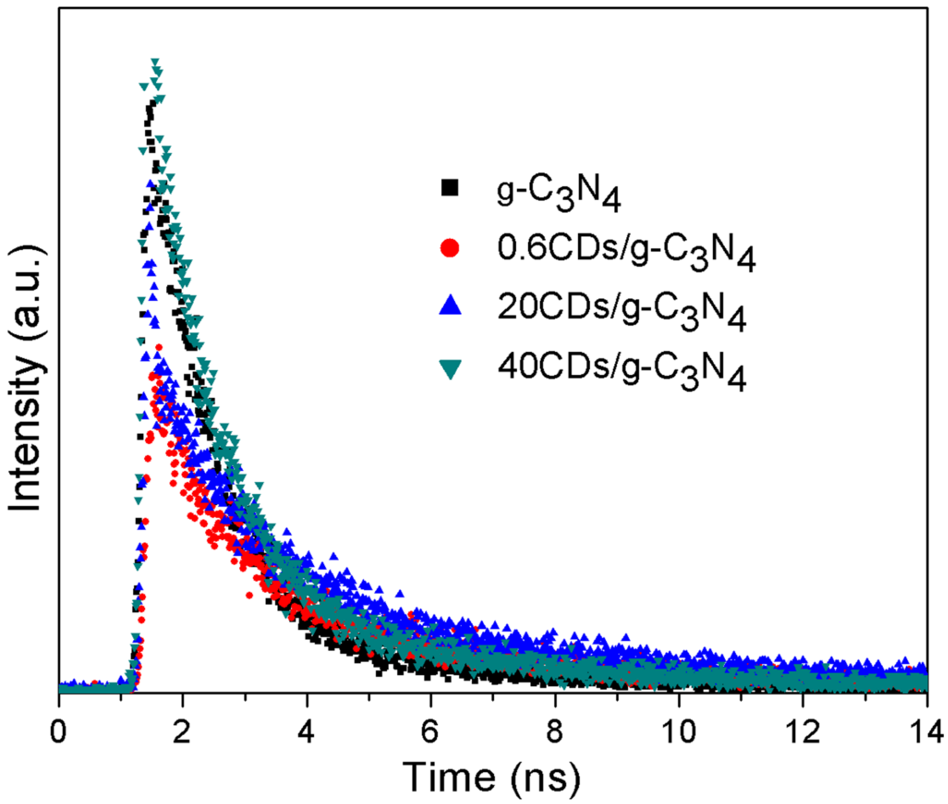

Figure 4.24: TRPL Spectrum of g-C_3N_4 and 0.6CDs/g-C_3N_4, 20CDs/g-C_3N_4 and 40CDs/g-C_3N_4

The photocatalytic performances of pure g-C_3N_4 and different wt% CDs/g-C_3N_4 composites were evaluated by degrading 2,4-DCP under natural sunlight irradiation. Prior to the photodegradation under sunlight, the 2,4-DCP solution was stirred in the dark condition for 18 h to form adsorption-desorption equilibrium. The 2,4-DCP concentration reduced approximately 20% for all samples when the adsorption-desorption equilibrium was established. The photodegradation rate was calculated using the following equation:

$$\text{Photodegradation rate} = \left(\frac{C_0 - C}{C_0}\right) \times 100\% \qquad (4.7)$$

where C_0 and C are the 2,4-DCP concentrations in the solution at time 0 and t min, respectively.

Table 4.6 summarizes the correlation between the physicochemical properties of photocatalyst and their degradation performance. There was no degradation occurred throughout the experiment in the blank sample as shown in Figure 4.25(a), indicating that the 2,4-DCP was a poor photosensitizing compound and the degradation was purely performed by the applied photocatalysts. The 2,4-DCP was almost fully degraded by 20CDs/g-C_3N_4 and 40CDs/g-C_3N_4 within 120 min with similar removal efficiency of 94%. While the removal efficiency of 0.6CDs/g-C_3N_4 and g-C_3N_4 was 79.63% and 71.30%, respectively (Table 4.6). The low band gap of pure g-C_3N_4 (2.95 eV) caused a moderately good photodegradation of BPA. The degradation efficiency increased ~14% from 0.6CDs/g-C_3N_4 to 20CDs/g-C_3N_4 composite, suggesting that high loading of CDs can boost the degradation efficiency. Figure 4.25(b) shows the rate constant, k value of g-C_3N_4, 0.6CDs/g-C_3N_4, 20CDs/g-C_3N_4 and 40CDs/g-C_3N_4 were 0.011, 0.013, 0.0194, and 0.0186 min^{-1} respectively. Among the samples, both of 20CDs/g-C_3N_4 and 40CDs/g-C_3N_4 achieved the highest degradation rate of 94% which was 1.76 times higher than that of g-C_3N_4. The superior degradation efficiency of 20CDs/g-C_3N_4 was predominantly due to the prolonged lifetime of electron-hole pairs in the composites which correlated well with the TRPL results (Table 4.5). The prolonged charge-carrier lifetime promoted more holes and electrons to react with water and oxygen to produce more hydroxyl and superoxide anion radicals for the degradation of 2,4-DCP. Although 40CDs/g-C_3N_4 showed shorter charge-carrier lifetime than 0.6CDs/g-C_3N_4 and 20CDs/g-C_3N_4, the degradation rate was higher than 0.6CDs/g-C_3N_4 and similar with 20CDs/g-C_3N_4. These results advocated that the excellent light harvesting ability and high surface area of 40CDs/g-C_3N_4 could overcome the limitation of short charge carrier lifetime and achieved similar degradation efficiency with 20CDs/g-C_3N_4. Thus it is concluded that both of the electron-hole pairs separation efficiency and extension of light absorption spectrum were equally important for the improvement of photocatalytic performance. Meanwhile the increased surface area of the composites could supply extra active sites for the degradation of 2,4-DCP. These factors played an essential role to improve the overall degradation efficiency.

Table 4.6: Correlation between Physicochemical Properties and Degradation Performance

Photocatalyst	**Physicochemical Properties**			
	BET Surface Area	**Visible Light Absorption**	**Charge Carriers Lifetime**	**2,4-DCP Degradation Efficiency (%)**
g-C_3N_4	moderate	lowest	shortest	71.30
0.6CDs/g-C_3N_4	moderate	low	moderate	79.63
20CDs/g-C_3N_4	small	moderate	long	93.77
40CDs/g-C_3N_4	large	high	short	94.00

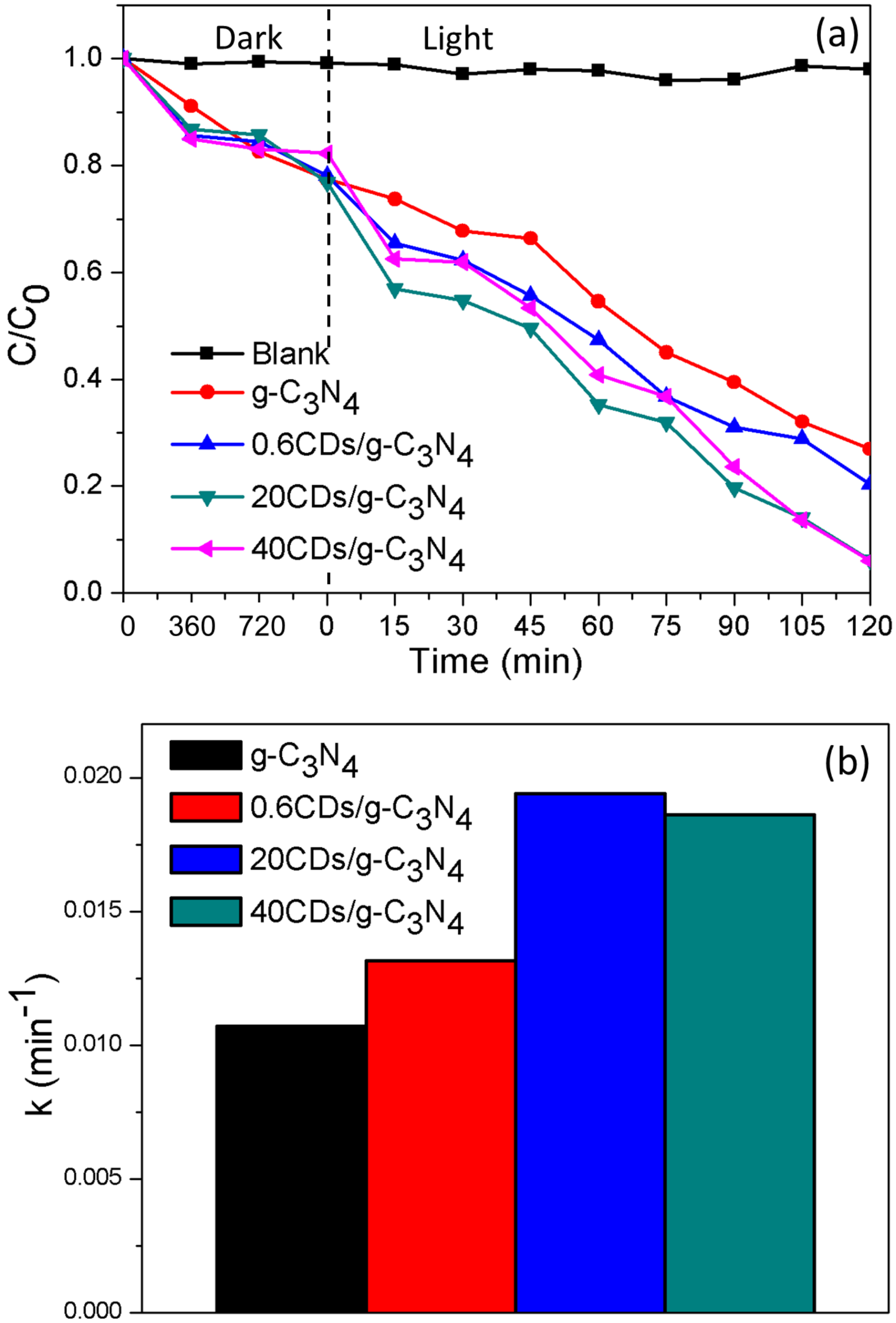

Figure 4.25: (a) Photocatalytic Degradation of 2,4-DCP (b) Apparent Rate Constant, k of g-C_3N_4 and 0.6CDs/g-C_3N_4, 20CDs/g-C_3N_4 and 40CDs/g-C_3N_4

20CDs/g-C_3N_4 composite was chosen to determine the active species in scavenging experiment due to their excellent performance with optimum amount of CDs. Several types of scavengers were used in this experiment such as ethylene diamine-tetraacetic acid disodium salt (EDTA-2Na^+), benzoquinone (BQ), isopropyl alcohol (IPA) and dimethyl sulfoxide (DMSO) which worked as holes (h^+), superoxide radicals ($^\bullet O_2^-$), hydroxyl radicals ($^\bullet OH$) and electron (e^-) catcher, respectively. Figure 4.26 displays the degradation rate in the order of DMSO > IPA > EDTA-2Na^+ > BQ. The low degradation efficiency indicated that the active species was being captured by scavenger and unable to perform degradation. Both of the e^- and $^\bullet OH$ were not the active species in the photodegradation of 2,4-DCP since the degradation in DMSO and IPA did not show significant changes. Upon the addition of BQ in the 2,4-DCP, the degradation rate was highly suppressed. This shows that $^\bullet O_2^-$ was one of the main active species involved in the photodegradation process. The addition of EDTA-2Na^+ slightly inhibited the degradation rate, indicating that the h^+ was the second active species.

The edge potential of the valence band (VB) and the conduction band (CB) of a photocatalyst at the point of zero charge were projected by using equations below:

$$E_{VB} = X - E_c + 0.5E_g \quad (4.8)$$

$$E_{CB} = E_{VB} - E_g \quad (4.9)$$

where E_{CB} and E_{VB} are the CB and VB edge potential respectively, E_g is the band gap energy of the semiconductor.; E_c is the energy of free electrons on the hydrogen scale (≈4.5 eV vs NHE) and X is the electronegativity of the semiconductor The X value of g-C_3N_4 is 4.64 eV (Leong et al., 2015) while the band gap energy of g-C_3N_4 is 2.95 eV (Table 4.4). The VB and CB of g-C_3N_4 were calculated to be 1.62 eV and −1.33 eV, respectively. Figure 4.27 illustrated the schematic diagram of degradation mechanism of CDs/g-C_3N_4 composite. When the g-C_3N_4 was irradiated under the natural sunlight, the electrons in the VB were excited to the CB of g-C_3N_4 to form electron-hole pairs. The holes (h^+) in the VB of g-C_3N_4 directly oxidized 2,4-DCP but could not react with water (H_2O) and hydroxide (OH^-) to form $^{\bullet}OH$ radical. This is due to the VB of g-C_3N_4 (+1.62 eV) was less positive than the standard redox potential of $OH^-/^{\bullet}OH$ (+1.99 eV vs. NHE) and $H_2O/^{\bullet}OH$ (+2.38 eV vs. NHE) (Ni et al., 2016). Simultaneously, when CDs was incorporated into g-C_3N_4, the CDs acted as electron acceptors to trap the excited electron (e^-) from CB of g-C_3N_4 due to their conducting texture and excellent charge storing ability (Figure 4.27(a)). This helps to stimulate the separation and prolonging the lifetime of electron-hole pairs. The electrons will further react with the dissolved oxygen to form superoxide ($^{\bullet}O_2^-$) anion radicals to oxidize the 2,4-DCP. Furthermore, the photosensitizing effect of CDs can convert the photon energy to excite electron to sensitize g-C_3N_4 and donate the electrons to the CB of g-C_3N_4 (Liu et al., 2016) (Figure 4.27(b)). Subsequently the visible light response range of the synthesized samples were used for the photocatalytic degradation of 2,4-DCP. Even though the CDs did not acquire UCPL properties, the π-conjugated of CDs function as a photosensitizer to sensitize g-C_3N_4 and introduce more photoexcited electrons to the CB of g-C_3N_4 (Li et al., 2016). However, as the result of 2,4-DCP degradation efficiency was well in line with the TRPL results, the photogenerated electron-hole pairs separation efficiency worked as the prevailing factor for the advancement of photocatalytic performance in CDs/g-C_3N_4 composites. Zhang et al. (2015) and Wang et al. (2013) reported that heterojunction interface between CDs and g-C_3N_4 efficiently promoted the rapid interfacial charge transfer and thus enhancing the electron-hole pairs separation. This occasioned in the generation of more electrons and holes to produce more active radicals like $^{\bullet}OH$ and $^{\bullet}O_2^-$ for the removal of targeted pollutant.

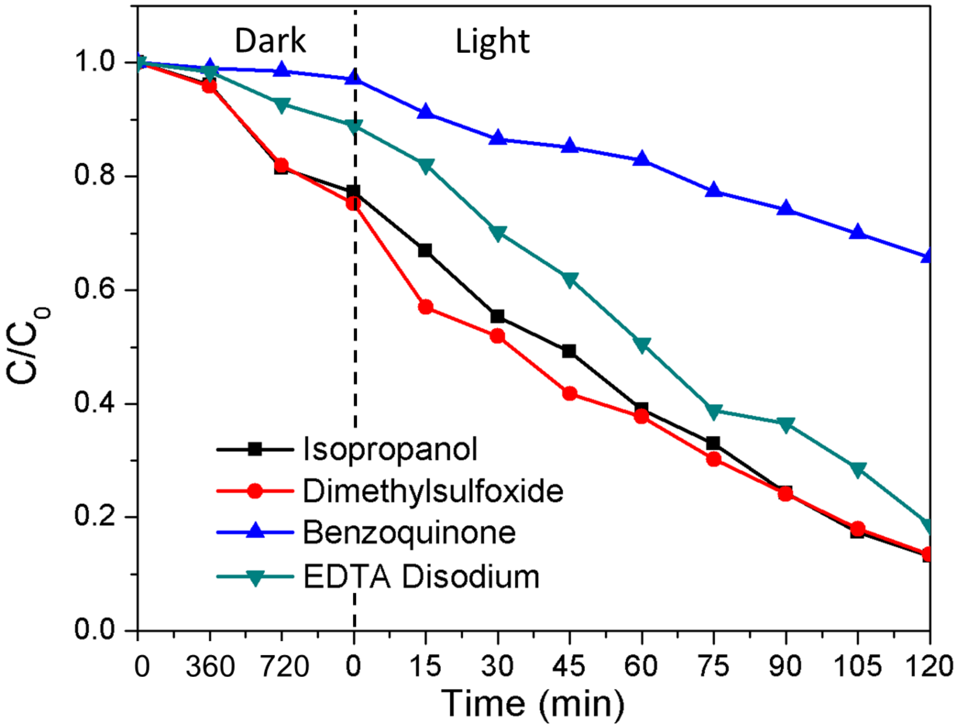

Figure 4.26: Scavengers Test Results of CDs/g-C_3N_4

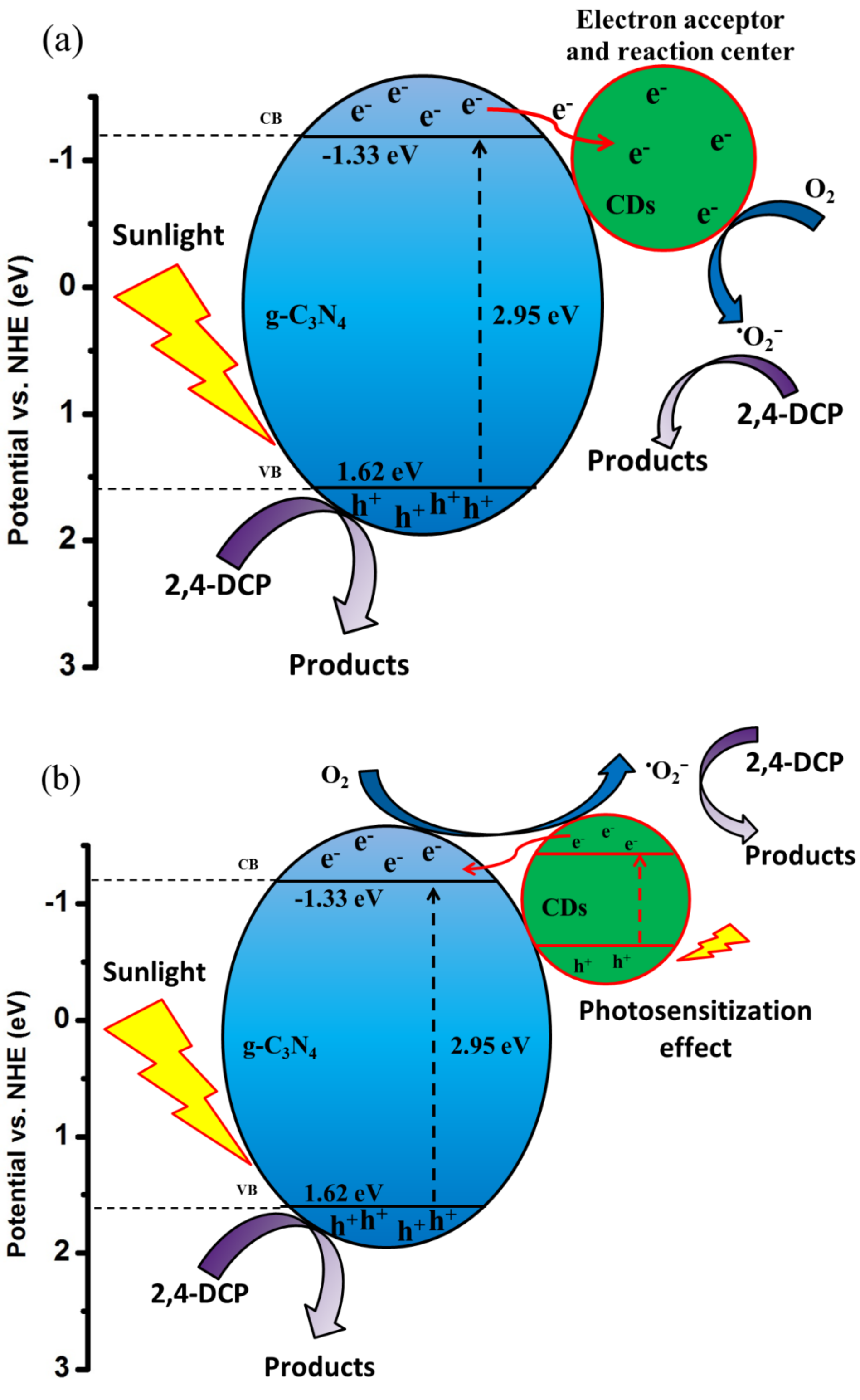

Figure 4.27: Photocatalysis Mechanism of CDs/g-C_3N_4 (a) As an Electron Acceptor and Reaction Center (b) Photosensitization Effect of CDs

In order to understand the NIR-driven ability of synthesized CDs/g-C_3N_4 composite, 40CDs/g-C_3N_4 was chosen to evaluate the photocatalytic performance under near infrared (NIR) illumination due to the outstanding absorption ability compared to other prepared composites. Figure 4.28 shows the results of NIR degradation test, which the degradation efficiency of 40CDs/g-C_3N_4 was 23% after 120 min under IR irradiation. The degradation efficiency is extremely low compared with the result under sunlight irradiation (94%). This result further reveals that the absence of UCPL properties in CDs was unable to convert the absorbed NIR wavelength to visible and UV wavelength and hence the removal of targeted pollutant under NIR irradiation was not significant.

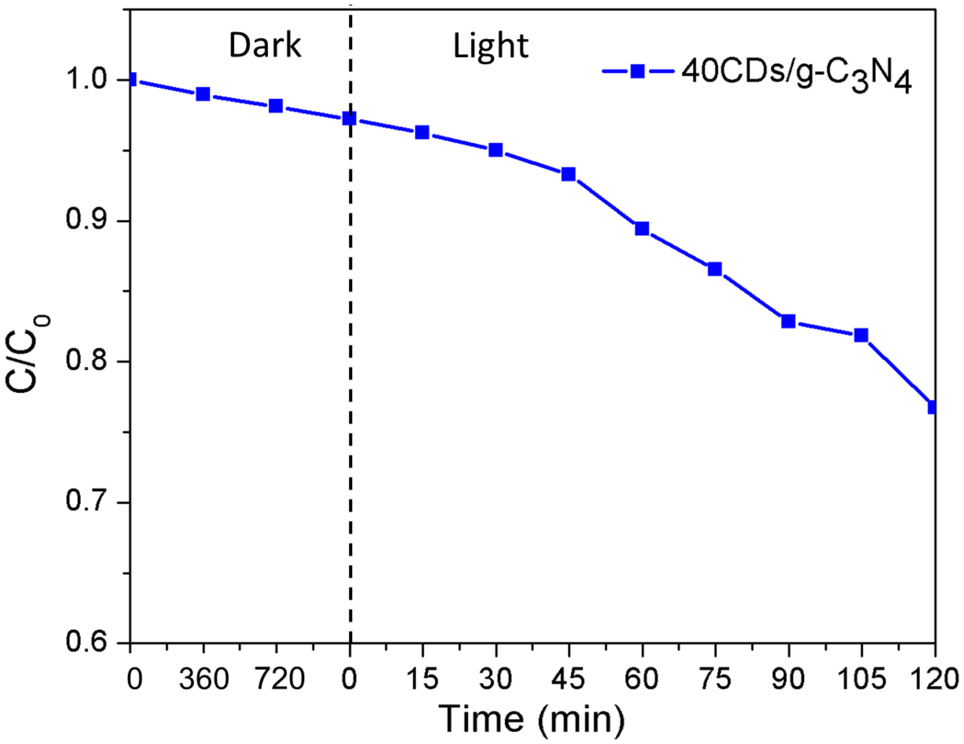

Figure 4.28: NIR Degradation Test Results of 40CDs/g-C_3N_4

Table 4.7 shows the comparison study results between the present study and previous literature report. In this present study, the CDs/g-C_3N_4 was able to degrade 94.0% of 2,4-DCP within 120 min while the CDs/g-C_3N_4 composite synthesized by Zhang et al. (2016) was managed to fully degrade phenol compound within 200 min. This suggests that phenol compound need longer duration for the complete degradation. Furthermore, most of the reported CDs composites such as CDs/g-C_3N_4, CDs/Bi_2WO_6 and CDs/BiOI fully degrade BPA within 120 min due to high photogenerated electron-hole pairs separation rate and extended light absorption range (Sim et al., 2018; Wang et al., 2018; Di et al., 2016). The CDs/g-C_3N_4 synthesized by Zhang et al. (2018) unveiled only 80.0% photocatalytic degradation performance within 120 min which was lower than other studies due to the less initial photocatalyst loading (20 mg), while the initial photocatalyst loading for others studies was 100 mg. Di and co-workers reported that nitrogen doped carbon dots (N-CDs) were capable to facilitate the superior activation of molecular oxygen, resulted in superior 4-chlorophenol (4-CP) removal efficiency in N-CDs/$BiPO_4$ composite (Di et al., 2017). Overall, the degradation results of the present study are comparable with previous works which reported the use of citric acid to produce CDs (Zhang et al., 2016; Di et al., 2016). The CDs was derived from plant wastes which is water hyacinth instead of chemicals, thus a sustainable and greener solution for environmental remediation is produced.

Table 4.7: Comparison Study of the Degradation of EDCs Using Other Photocatalysts

Composite	**Organic Pollutant**	**Photocatalyst (mg)**	**Initial Concentration (mg/L)**	**Duration (min)**	**Degradation Efficiency, %**	**Reference**
CDs/g-C_3N_4	2,4-DCP	100	5	120	94.0	Present Study
CDs/g-C_3N_4	Phenol	50	10	200	100.0	Zhang et al., 2016
CDs/g-C_3N_4	BPA	100	5	90	100.0	Sim et al., 2018
CDs/g-C_3N_4	BPA	20	10	120	80.0	Zhang et al., 2018
CDs/Bi_2WO_6	BPA	100	10	60	100.0	Wang et al., 2018
CDs/BiOI	BPA	100	10	120	100.0	Di et al., 2016
N-CDs/$BiPO_4$	4-CP	30	10	120	100.0	Di et al., 2017

4.3 Costing and Sustainability

In this section, the cost for the preparation of photocatalyst was calculated to consider whether the project is economical and practical. The electricity bill can be evaluated under the category of commercial tariff B as shown in Table 4.8 (1st project) and Table 4.10 (2nd project). The material costs are calculated in Table 4.9 (1st project) and Table 4.11 (2nd project). The electricity bill was calculated using equation:

Electricity bill = RM 0.435 * Consumption per unit kwh (4.11)

Table 4.8: Energy Consumption for Synthesis of Photocatalyst (1st project)

Equipment	Power (watt)	Duration (hours)	Total Consumption (wh)
Muffle furnace	1800	3	5400
Oven	1800	48	86400
Centrifuge	455	2	910
Magnetic Stirrer	42.5	1.0	42.5
Sonicator	100	0.5	50
		Sum	92802.5

Total Electricity usage = 92.8025 kwh * RM0.435 / kwh
= RM 40.37

Table 4.9: Material Used for Photocatalyst Preparation (1st project)

Materials	Price (RM)	Usage	Cost (RM)
Urea (500g)	16.00	50g	1.60
Ethylene glycol (400mL)	2.00	60mL	0.30
$HAuCl_4$ (1g)	685.00	0.3151g	215.84
$AgNO_3$ (25g)	730.00	0.1359g	3.97
$Na_2[PdCl_4]$ (1g)	765.00	0.2354g	180.08
Ethanol (2.5L)	28.00	100mL	1.12
		Sum	402.91

Total cost of production = Electric consumption + Materials cost
= RM 40.37 + RM 402.91
= RM 443.28

Table 4.10: Energy Consumption for Synthesis of Photocatalyst (2nd project)

Equipment	Power (watt)	Duration (hours)	Total Consumption (wh)
Muffle furnace	1800	3	5400
Oven	1800	42	75600
Centrifuge	455	1.2	546
Magnetic Stirrer	42.5	24.5	1041.25
		Sum	82587.25

Total Electricity usage = 82.58725 kwh * RM0.435 / kwh
= RM 35.93

Table 4.11: Material Used for Photocatalyst Preparation (2nd project)

Materials	Price (RM)	Usage	Cost (RM)
Urea (500g)	16.00	50g	1.60
Water Hyacinths Leaves	0.00	10g	0.00
		Sum	1.60

Total cost of production = Electric consumption + Materials cost
= RM 35.93 + RM 1.60
= RM 37.53

The base photocatalyst adopted in the research was synthesized from urea which is economic. From the calculation above, the production cost of 1st project (RM 443.28) was higher than 2nd project (RM 37.53) because of the high cost noble metals precursor. To reduce the energy consumption, the natural sunlight was utilized in synthesis process such as photodeposition noble metals onto the surface of g-C_3N_4 and drying the water hyacinth (WH) leaves. The 2nd project is more sustainable than 1st project because of the carbon dots (CDs) was synthesized using WH leaves as green precursors which could be obtained easily from natural resources such as pond, lake and river. This raw material can be replenished easily and thus it was considered as sustainable resources and environmentally-friendly products. The synthesis method consumed low energy, less chemical usage and fewer by-products were produced throughout the synthesis process. The photocatalytic process only acquired sunlight as the energy source to degrade the organic pollutant without using harmful oxidizing agent and UV light source. The solar energy is a renewable and free energy source which can replace the utilization of fluorescent and UV lamp. Photocatalyst can convert the organic pollutant i.e. BPA and 2,4-DCP into simple molecules such as water and carbon dioxide through redox reaction. Subsequently, the photocatalyst can reduce the harmful organic pollutant that is harmful to human and animal health, thus leading to a greener and sustainable future. On the other hand, the degradation efficiency of 1st project was higher than 2nd project. Although the pollutant was different, 1st project fully degraded the BPA within 70 min while 2nd project degraded 94% of the 2,4-DCP within 120 min. From the aspect of production cost, sustainable and environmentally-friendly, CDs/g-C_3N_4 composite (2nd project) was recommended for further research to explore their potential in real life application.

CHAPTER 5

CONCLUSIONS AND RECOMMENDATIONS

5.1 Conclusions

The primary objective of this dissertation was to modify and improve the electron-hole pairs separation efficiency of conventional g-C_3N_4 that is visible-light-active for water remediation. The aforementioned aims were successfully accomplished by assembling g-C_3N_4 with the support of noble metals and carbon dots (CDs). For the 1st project, Pd, Ag, and Au NPs in their respective particle size of 7.3, 7.5 and 8.6 nm were successfully deposited on the surface of g-C_3N_4 using natural sunlight as irradiation source. All noble metal doped g-C_3N_4 exhibited better photocatalytic performance than that of g-C_3N_4, completely degrading BPA from aqueous solution in 90 min under natural sunlight illumination. The enhancement of photocatalytic performance depended crucially on the contributing role of noble metal NPs acting as an electron acceptor in extending the lifespan of photogenerated electron-hole pairs. Ag NPs act as the most efficient electron sinks among the other noble metals due to its smaller particle size (7.5 nm) and the optimum weight percentage (9.07 wt%). This facilitated the rapid electron transfer to the trapping sites of Ag NPs and promoted excellent degradation efficiency of BPA with the reaction rate of 2.15 faster than other composites. The introduction of all noble metals obviously improved the visible light absorption properties of g-C_3N_4 in which Au NPs showed significant LSPR behavior. Au/g-C_3N_4 exhibited deprived performance because the excitation of Au NPs triggered by LSPR effect provided two pathways for electron transfer from Au NPs to g-C_3N_4 and vice versa which decreased the amount of trapped electrons in Au NPs. The h^+ and $^{\bullet}O_2^-$ radical were the main reactive species for all composites for the degradation of BPA. The present synthesis method contributes to the sustainable synthesis using solely natural sunlight from the synthesis to application route to produce efficient photocatalysts for the remediation of water pollution.

For the 2nd project, CDs were successfully derived from WH leaves via a green and versatile route and the CDs/g-C_3N_4 composites were successfully amalgamated *via* hydrothermal treatment. The particle size of CDs ranged from 1.2 nm to 4.9 nm and a blue-green fluorescence was emitted under the UV light irradiation at 365 nm. The synthesized CDs did not acquire the upconverted photoluminescence (UCPL) properties. After incorporating CDs into the g-C_3N_4, the light respond ranges of CDs/g-C_3N_4 composites shifted towards the visible region and the band gap energy of g-C_3N_4, 0.6CDs/g-C_3N_4, 20CDs/g-C_3N_4 and 40CDs/g-C_3N_4 were measured to be 2.95 eV, 2.94 eV, 2.92 eV and 2.92eV, respectively. Both of 20CDs/g-C_3N_4 and 40CDs/g-C_3N_4 recorded the highest photocatalytic performance in degrading 2,4-DCP, approximately 1.7 times higher than that of pure g-C_3N_4. The superior electron-hole pairs separation properties of 20CDs/g-C_3N_4 had boosted the photocatalytic performance. While the short charge carrier lifetime of 40CDs/g-C_3N_4 was overcome by its outstanding light harvesting ability and high surface area which helped to generate more electron-hole pairs and supplied more active sites for the adsorption of 2,4-DCP. Both of the electron-hole pairs separation efficiency and visible light harvesting properties were dominant factors contributing to the excellent photocatalytic performance. For the scavenger test, hole (h^+) and superoxide radical ($^{\bullet}O_2^-$) were acknowledged as the key active species in photocatalysis.

5.2 Recommendations

The following recommendations are taken into considerations for future research works.

i. Different types of organic pollutants e.g. 2-chlorophenol, 4-chlorophenol, Amoxicillin and dioxin could be used to test the photodegradation efficiency.
ii. A scale up study equipped with a suitable reactor could exhibit real time applications and industrially feasibility.
iii. Explore other green precursor such as paper, animal faeces, fruit wastes and etc. to search for a precursor which can produce CDs with UCPL properties.

REFERENCES

Andreozzi, R., Caprio, V., Insola, A. and Marotta, R., 1999. Advanced oxidation processes (AOP) for water purification and recovery. *Catalysis Today*, 53(1), pp. 51-59.

Bagheri, S. and Julkapli, N.M., 2016. Magnetite hybrid photocatalysis: advance environmental remediation. *Reviews in Inorganic Chemistry*, 36(3), pp. 135-151.

Bhaisare, M.L., Talib, A., Khan, M.S., Pandey, S. and Wu, H.F., 2015. Synthesis of fluorescent carbon dots via microwave carbonization of citric acid in presence of tetraoctylammonium ion, and their application to cellular bioimaging. *Microchimica Acta*, *182*(13-14), pp. 2173-2181.

Bhowmik, T., Kundu, M.K. and Barman, S., 2015. Ultra small gold nanoparticles–graphitic carbon nitride composite: an efficient catalyst for ultrafast reduction of 4-nitrophenol and removal of organic dyes from water. *RSC Advances*, 5(48), pp. 38760-38773.

Bottini, M., Balasubramanian, C., Dawson, M.I., Bergamaschi, A., Bellucci, S. and Mustelin, T., 2006. Isolation and characterization of fluorescent nanoparticles from pristine and oxidized electric arc-produced single-walled carbon nanotubes. *The Journal of Physical Chemistry B*, 110(2), pp. 831–836.

Broséus, R., Vincent, S., Aboulfadl, K., Daneshvar, A., Sauvé, S., Barbeau, B. and Prévost, M., 2009. Ozone oxidation of pharmaceuticals, endocrine disruptors and pesticides during drinking water treatment. *Water Research*, 43(18), pp. 4707-4717.

Bu, W., Zhang, L., Hua, Z., Chen, H. and Shi, J., 2007. Synthesis and characterization of uniform spindle-shaped microarchitectures self-assembled from aligned single-crystalline nanowires of lanthanum phosphates. *Crystal Growth and Design*, 7(11), pp. 2305-2309.

Cao, S., Low, J., Yu, J. and Jaroniec, M., 2015. Polymeric photocatalysts based on graphitic carbon nitride. *Advanced Materials*, 27(13), pp. 2150-2176.

Castro, H.P., Pereira, M.K., Ferreira, V.C., Hickmann, J.M. and Correia, R.R., 2017. Optical characterization of carbon quantum dots in colloidal suspensions. *Optical Materials Express*, 7(2), pp. 401-408.

Chang, C., Fu, Y., Hu, M., Wang, C., Shan, G. and Zhu, L., 2013. Photodegradation of bisphenol A by highly stable palladium-doped mesoporous graphite carbon nitride (Pd/mpg-C_3N_4) under simulated solar light irradiation. *Applied Catalysis B: Environmental*, 142, pp. 553-560.

Chang, S., Xie, A., Chen, S. and Xiang, J., 2014. Enhanced photoelectrocatalytic oxidation of small organic molecules by gold nanoparticles supported on carbon nitride. *Journal of Electroanalytical Chemistry*, 719, pp. 86-91.

Chen, C., 2014. *Visible light photocatalysts for synthesis of fine organic chemicals on supported nanostructures.* PhD thesis, Queensland University of Technology, Australia.

Chen, P.J., Linden, K.G., Hinton, D.E., Kashiwada, S., Rosenfeldt, E.J. and Kullman, S.W., 2006. Biological assessment of bisphenol A degradation in water following direct photolysis and UV advanced oxidation. *Chemosphere*, 65(7), pp. 1094-1102.

Chen, W., Hu, C., Yang, Y., Cui, J. and Liu, Y., 2016. Rapid synthesis of carbon dots by hydrothermal treatment of lignin. *Materials*, 9(3), pp. 184.

Chen, X., 2010. *Noble metal photocatalysts under visible light and UV light irradiation.* PhD thesis, Queensland University of Technology, Australia.

Cheng, N., Tian, J., Liu, Q., Ge, C., Sun, X., Qusti, A., Asiri, A. and Al-Youbi, A., 2013. Au-nanoparticle-loaded graphitic carbon nitride nanosheets: green photocatalytic synthesis and application toward the degradation of organic pollutants. *ACS Applied Materials and Interfaces*, 5(15), pp. 6815-6819.

Coleman, H.M., Chiang, K. and Amal, R., 2005. Effects of Ag and Pt on photocatalytic degradation of endocrine disrupting chemicals in water. *Chemical Engineering Journal*, 113, pp. 65-72.

Colmenares, J. C. and Luque, R., 2014. Heterogeneous photocatalytic nanomaterials: prospects and challenges in selective transformations of biomass-derived compounds. *Chemical Society Reviews*, 43(3), pp. 765-778.

Daghrir, R., Drogui, P. and Robert, D., 2013. Modified TiO_2 for environmental photocatalytic applications: a review. *Industrial & Engineering Chemistry Research*, 52(10), pp. 3581-3599.

Dai, H., Gao, X., Liu, E., Yang, Y., Hou, W., Kang, L., Fan, J. and Hu, X., 2013. Synthesis and characterization of graphitic carbon nitride sub-microspheres using microwave method under mild condition. *Diamond and Related Materials*, 38, pp. 109-117.

Das, P., Bose, M., Ganguly, S., Mondal, S., Das, A.K., Banerjee, S. and Das, N.C., 2017. Green approach to photoluminescent carbon dots for imaging of gram-negative bacteria Escherichia coli. *Nanotechnology*, 28(19), pp. 195501.

Di, J., Xia, J., Ji, M., Wang, B., Yin, S., Xu, H., Chen, Z. and Li, H., 2016. Carbon quantum dots induced ultrasmall BiOI nanosheets with assembled hollow structures for broad spectrum photocatalytic activity and mechanism insight. *Langmuir*, 32(8), pp. 2075-2084.

Di, J., Xia, J., Chen, X., Ji, M., Yin, S., Zhang, Q. and Li, H., 2017. Tunable oxygen activation induced by oxygen defects in nitrogen doped carbon quantum dots for sustainable boosting photocatalysis. *Carbon*, 114, pp. 601-607.

Dong, F., Wang, Z., Sun, Y., Ho, W.K. and Zhang, H., 2013. Engineering the nanoarchitecture and texture of polymeric carbon nitride semiconductor for enhanced visible light photocatalytic activity. *Journal of Colloid and Interface Science*, 401, pp. 70-79.

Dong, G., Zhang, Y., Pan, Q. and Qiu, J., 2014. A fantastic graphitic carbon nitride (g-C_3N_4) material: electronic structure, photocatalytic and photoelectronic properties. *Journal of Photochemistry and Photobiology C: Photochemistry Reviews*, 20, pp. 33-50.

Du, W., Xu, X., Hao, H., Liu, R., Zhang, D., Gao, F. and Lu, Q., 2015. Green synthesis of fluorescent carbon quantum dots and carbon spheres from pericarp. *Science China Chemistry*, 58(5), pp. 863-870.

Esplugas, S., Bila, D.M., Krause, L.G.T. and Dezotti, M., 2007. Ozonation and advanced oxidation technologies to remove endocrine disrupting chemicals (EDCs) and pharmaceuticals and personal care products (PPCPs) in water effluents. *Journal of Hazardous Materials*, 149(3), pp. 631-642.

Fadllan, A., Marwoto, P., Aji, M.P., Susanto and Iswari, R.S., 2017. Synthesis of carbon nanodots from waste paper with hydrothermal method. In *AIP Conference Proceedings*, January 2017, 1788(1), pp. 030069.

Fagan, R., McCormack, D.E., Hinder, S.J. and Pillai, S.C., 2016. Photocatalytic properties of g-C_3N_4–TiO_2 heterojunctions under UV and visible light conditions. *Materials*, 9(4), pp. 286.

Fang, S., Xia, Y., Lv, K., Li, Q., Sun, J. and Li, M., 2016. Effect of carbon-dots modification on the structure and photocatalytic activity of g-C_3N_4. *Applied Catalysis B: Environmental*, 185, pp. 225-232.

Fang, W., Deng, Y., Tang, L., Zeng, G., Zhou, Y., Xie, X., Wang, J., Wang, Y. and Wang, J., 2017. Synthesis of Pd/Au bimetallic nanoparticle-loaded ultrathin graphitic carbon nitride nanosheets for highly efficient catalytic reduction of p-nitrophenol. *Journal of Colloid and Interface Science*, 490, pp. 834-843.

Fang, Y., Guo, S., Li, D., Zhu, C., Ren, W., Dong, S. and Wang, E., 2011. Easy synthesis and imaging applications of cross-linked green fluorescent hollow carbon nanoparticles. *ACS Nano*, 6(1), pp. 400–409.

Fu, Y., Huang, T., Jia, B., Zhu, J. and Wang, X., 2017. Reduction of nitrophenols to aminophenols under concerted catalysis by Au/g-C_3N_4 contact system. *Applied Catalysis B: Environmental*, 202, pp. 430-437.

Fu, Y., Huang, T., Zhang, L., Zhu, J. and Wang, X., 2015. Ag/g-C_3N_4 catalyst with superior catalytic performance for the degradation of dyes: a borohydride-generated superoxide radical approach. *Nanoscale*, 7(32), pp. 13723-13733.

Fujishima, A. and Honda, K., 1972. Electrochemical photolysis of water at a semiconductor electrode. *Nature*, 238(5358), pp. 37.

Gao, G., Jiao, Y., Ma, F., Jiao, Y., Waclawik, E. and Du, A., 2015. Carbon nanodot decorated graphitic carbon nitride: new insights into the enhanced photocatalytic water splitting from ab initio studies. *Physical Chemistry Chemical Physics*, 17(46), pp. 31140-31144.

Gao, J., Zhou, Y., Li, Z., Yan, S., Wang, N. and Zou, Z., 2012. High-yield synthesis of millimetre-long, semiconducting carbon nitride nanotubes with intense photoluminescence emission and reproducible photoconductivity. *Nanoscale*, 4(12), pp. 3687-3692.

Gaya, U.I. and Abdullah, A.H., 2008. Review: heterogeneous photocatalytic degradation of organic contaminants over titanium dioxide: a review of fundamentals, progress and problems. *Journal of Photochemistry and Photobiology, C: Photochemistry Reviews*, 9, pp. 1-12.

Ge, L., Zuo, F., Liu, J., Ma, Q., Wang, C., Sun, D., Bartels, L. and Feng, P., 2012. Synthesis and efficient visible light photocatalytic hydrogen evolution of polymeric g-C_3N_4 coupled with CdS quantum dots. *The Journal of Physical Chemistry C*, 116(25), pp. 13708-13714.

Ge, L., Han, C. and Liu, J., 2011a. Novel visible light-induced g-C_3N_4/Bi_2WO_6 composite photocatalysts for efficient degradation of methyl orange. *Applied Catalysis B, Environmental*, 108, pp. 100-107.

Ge, L., Han, C., Liu, J. and Li, Y., 2011b. Enhanced visible light photocatalytic activity of novel polymeric g-C_3N_4 loaded with Ag nanoparticles. *Applied Catalysis A, General*, 409, pp. 215-222.

Gonzalez, H.I. (2015). *Photocatalytic H_2-production through photo-reforming of hydrocarbons: synthesis and photocatalytic appliacation of TiO_2 nanotubes.* Master thesis, Norwegian University of Science and Technology, Trondheim.

Grabowska, E., Marchelek, M., Klimczuk, T., Trykowski, G. and Zaleska-Medynska, A., 2016. Noble metal modified TiO_2 microspheres: surface properties and photocatalytic activity under UV–vis and visible light. *Journal of Molecular Catalysis A: Chemical*, *423*, pp.191-206.

Guan, W., Gu, W., Ye, L., Guo, C., Su, S., Xu, P. and Xue, M., 2014. Microwave-assisted polyol synthesis of carbon nitride dots from folic acid for cell imaging. *International Journal of Nanomedicine*, 9, pp. 5071.

Gultekin, I., Tezcanli-Guyer, G. and Ince, N.H., 2009. Degradation of 4-n-nonylphenol in water by 20 kHz ultrasound. *Journal of Advanced Oxidation Technologies*, 12(1), pp. 105-110.

Guo, C., Ge, M., Liu, L., Gao, G., Feng, Y. and Wang, Y., 2009. Directed synthesis of mesoporous TiO_2 microspheres: catalysts and their photocatalysis for bisphenol A degradation. *Environmental Science and Technology*, 44(1), pp. 419-425.

Guo, F., Shi, W., Guan, W., Huang, H. and Liu, Y., 2017. Carbon dots/g-C_3N_4/ZnO nanocomposite as efficient visible-light driven photocatalyst for tetracycline total degradation. *Separation and Purification Technology*, 173, pp. 295-303.

Guo, Y., Zhang, L., Cao, F. and Leng, Y., 2016. Thermal treatment of hair for the synthesis of sustainable carbon quantum dots and the applications for sensing Hg^{2+}. *Scientific Reports*, 6, pp. 35795.

Gupta, V.K., Jain, R., Mittal, A., Mathur, M. and Sikarwar, S., 2007. Photochemical degradation of the hazardous dye Safranin-T using TiO_2 catalyst. *Journal of Colloid and Interface Science*, 309(2), pp. 464-469.

Han, C., Wu, L., Ge, L., Li, Y. and Zhao, Z., 2015. AuPd bimetallic nanoparticles decorated graphitic carbon nitride for highly efficient reduction of water to H_2 under visible light irradiation. *Carbon*, 92, pp. 31-40.

He, J., 2015. *Preparation and photocatalysis of graphite carbon nitride based photocatalysts.* Master thesis, Curtin University, Australia.

He, P.J., Zheng, Z., Zhang, H., Shao, L.M. and Tang, Q.Y., 2009. PAEs and BPA removal in landfill leachate with Fenton process and its relationship with leachate DOM composition. *Science of the Total Environment*, 407(17), pp. 4928-4933.

Hilles, A.H., Amr, S.S.A., Aziz, H.A. and Bashir, M.J., 2019. Advanced Oxidation Processes for Water and Wastewater Treatment: An Introduction. *In Advanced Oxidation Processes (AOPs) in Water and Wastewater Treatment.* IGI Global, pp. 46-69.

Hma Salah, N., 2015. Surface plasmon resonance sensing and characterisation of nano-colloids for nanotoxicology applications. PhD thesis, University of Plymouth, England.

Hu, C., Liu, Y., Yang, Y., Cui, J., Huang, Z., Wang, Y., Yang, L., Wang, H., Xiao, Y. and Rong, J., 2013. One-step preparation of nitrogen-doped graphene quantum dots from oxidized debris of graphene oxide. *Journal of Materials Chemistry B*, 1(1), pp. 39-42.

Huang, D., Li, Z., Zeng, G., Zhou, C., Xue, W., Gong, X., Yan, X., Chen, S., Wang, W. and Cheng, M., 2018. Megamerger in photocatalytic field: 2D g-C_3N_4 nanosheets serve as support of 0D nanomaterials for improving photocatalytic performance. *Applied Catalysis B: Environmental*, 240, pp. 153-173.

Imai, S., Shiraishi, A., Gamo, K., Watanabe, I., Okuhata, H., Miyasaka, H., Ikeda, K., Bamba, T. and Hirata, K., 2007. Removal of phenolic endocrine disruptors by Portulaca oleracea. *Journal of Bioscience and Bioengineering*, 103, pp. 420-426.

Jana, J., Ganguly, M. and Pal, T., 2016. Enlightening surface plasmon resonance effect of metal nanoparticles for practical spectroscopic application. *RSC Advances*, 6(89), pp. 86174-86211.

Jelinek, R., 2017. Carbon-dot synthesis. In: *Carbon quantum dots Synthesis, Properties and Applications*. New York, USA, Springer Publishing Company, pp. 5-27.

Jian, X., Liu, X., Yang, H.M., Li, J.G., Song, X.L., Dai, H.Y. and Liang, Z.H., 2016. Construction of carbon quantum dots/proton-functionalized graphitic carbon nitride nanocomposite via electrostatic self-assembly strategy and its application. *Applied Surface Science*, 370, pp. 514-521.

Jiang, H., Chen, F., Lagally, M.G. and Denes, F.S., 2009. New strategy for synthesis and functionalization of carbon nanoparticles, *Langmuir*. 26(3), pp. 1991–1995.

Jiang, Z., Ouyang, Q., Peng, B., Zhang, Y. and Zan, L., 2014. Ag size-dependent visible-light-responsive photoactivity of Ag–TiO_2 nanostructure based on surface plasmon resonance. *Journal of Materials Chemistry A*, 2(46), pp. 19861-19866.

Jin, J., Liang, Q., Ding, C., Li, Z. and Xu, S., 2017. Simultaneous synthesis-immobilization of Ag nanoparticles functionalized 2D g-C_3N_4 nanosheets with improved photocatalytic activity. *Journal of Alloys and Compounds*, 691, pp. 763-771.

Jo, W.K. and Tayade, R.J., 2014. Recent developments in photocatalytic dye degradation upon irradiation with energy-efficient light emitting diodes. *Chinese Journal of Catalysis*, 35(11), pp. 1781-1792.

Kamaz, M.A.A., 2017. *Removal of endocrine disrupting compounds using membrane bioreactor*. Doctoral dissertation, University of Arkansas, Arkansas.

Kasibabu, B.S.B., D'souza, S.L., Jha, S., Singhal, R.K., Basu, H. and Kailasa, S.K., 2015. One-step synthesis of fluorescent carbon dots for imaging bacterial and fungal cells. *Analytical Methods*, 7(6), pp. 2373-2378.

Keller, R.P., Lodge, D.M., Lewis, M.A. and Shogren, J.F. eds., 2009. *Bioeconomics of invasive species: integrating ecology, economics, policy, and management*. Oxford University Press.

Kenens, B., Chamtouri, M., Aubert, R., Miyakawa, K., Hayasaka, Y., Naiki, H., Watanabe, H., Inose, T., Fujita, Y., Lu, G. and Masuhara, A., 2016. Solvent-induced improvement of Au photo-deposition and resulting photo-catalytic efficiency of Au/TiO_2. *RSC Advances*, 6(100), pp. 97464-97468.

Konda, S.K., Amiri, M. and Chen, A., 2016. Photoassisted deposition of palladium nanoparticles on carbon nitride for efficient oxygen reduction. *The Journal of Physical Chemistry C*, 120(27), pp. 14467-14473.

Kushwaha, S.P.S., 2012. Remote sensing of invasive alien plant species. *Invasive Alien Plants: An Ecological Appraisal for the Indian Subcontinent (Ed. JR Bhatt, JS Singh, SP Singh, RS Tripathi and RK Kohli).* CABI International, United Kingdom, pp. 131-138.

Kvítek, O., Siegel, J., Hnatowicz, V. and Švorčík, V., 2013. Noble metal nanostructures influence of structure and environment on their optical properties. *Journal of Nanomaterials*, 2013, pp. 111.

Lam, S.M., Sin, J.C. and Mohamed, A.R., 2016. Review: a review on photocatalytic application of g-C_3N_4/semiconductor (CNS) nanocomposites towards the erasure of dyeing wastewater. *Materials Science in Semiconductor Processing*, 47, pp. 62-84.

Lang, J., Liu, M., Su, Y., Yan, L. and Wang, X., 2015. Fabrication of the heterostructured $CsTaWO_6$/Au/g-C_3N_4 hybrid photocatalyst with enhanced performance of photocatalytic hydrogen production from water. *Applied Surface Science*, 358, pp. 252-260.

Lang, X., Chen, X. and Zhao, J., 2014. Heterogeneous visible light photocatalysis for selective organic transformations. *Chemical Society Reviews*, 43(1), pp. 473-486.

Leong, K.H., Chu, H.Y., Ibrahim, S. and Saravanan, P., 2015a. Palladium nanoparticles anchored to anatase TiO_2 for enhanced surface plasmon resonance-stimulated, visible-light-driven photocatalytic activity. *Beilstein Journal of Nanotechnology*, 6(1), pp. 428-437.

Leong, K.H., Liu, S.L., Sim, L.C., Saravanan, P., Jang, M. and Ibrahim, S., 2015b. Surface reconstruction of titania with g-C_3N_4 and Ag for promoting efficient electrons migration and enhanced visible light photocatalysis. *Applied Surface Science*, 358, pp. 370-376.

Leong, K.H., Gan, B.L., Ibrahim, S. and Saravanan, P., 2014. Synthesis of surface plasmon resonance (SPR) triggered Ag/TiO_2 photocatalyst for degradation of endocrine disturbing compounds. *Applied Surface Science*, 319, pp. 128-135.

Li, H., He, X., Kang, Z., Huang, H., Liu, Y., Liu, J., Lian, S., Tsang, C.H.A., Yang, X. and Lee, S.T., 2010. Water-soluble fluorescent carbon quantum dots and photocatalyst design. *Angewandte Chemie International Edition*, 49(26), pp. 4430-4434.

Li, H., He, X., Liu, Y., Huang, H., Lian, S., Lee, S.T. and Kang, Z., 2011. One-step ultrasonic synthesis of water-soluble carbon nanoparticles with excellent photoluminescent properties. *Carbon*, 49(2), pp. 605–609.

Li, J. and Wu, N., 2015. Semiconductor-based photocatalysts and photoelectrochemical cells for solar fuel generation: a review. *Catalysis Science and Technology*, 5(3), pp. 1360-1384.

Li, K., Su, F.Y. and Zhang, W.D., 2016. Modification of g-C_3N_4 nanosheets by carbon quantum dots for highly efficient photocatalytic generation of hydrogen. *Applied Surface Science*, 375, pp. 110-117.

Li, X., Zhang, S., Kulinich, S.A., Liu, Y. and Zeng, H., 2014. Engineering surface states of carbon dots to achieve controllable luminescence for solid-luminescent composites and sensitive Be^{2+} detection. *Scientific Reports*, 4, pp. 4976.

Li, Z., Wang, J., Zhu, K., Ma, F. and Meng, A., 2015. Ag/g-C_3N_4 composite nanosheets: synthesis and enhanced visible photocatalytic activities. *Materials Letters*, 145, pp. 167-170.

Liang, S., Xia, Y., Zhu, S., Zheng, S., He, Y., Bi, J., Liu, M. and Wu, L., 2015. Au and Pt co-loaded g-C_3N_4 nanosheets for enhanced photocatalytic hydrogen production under visible light irradiation. *Applied Surface Science*, 358, pp. 304-312.

Linsebigler, A.L., Lu, G. and Yates Jr, J.T., 1995. Photocatalysis on TiO_2 surfaces: principles, mechanisms, and selected results. *Chemical Reviews*, 95(3), pp. 735-758.

Liu, C., Huang, H., Du, X., Zhang, T., Tian, N., Guo, Y. and Zhang, Y., 2015. In situ co-crystallization for fabrication of g-C_3N_4/Bi_5O_7I heterojunction for enhanced visible-light photocatalysis. *The Journal of Physical Chemistry C*, 119(30), pp. 17156-17165.

Liu, G., Niu, P., Sun, C., Smith, S.C., Chen, Z., Lu, G.Q. and Cheng, H.M., 2010. Unique electronic structure induced high photoreactivity of sulfur-doped graphitic C_3N_4. *Journal of the American Chemical Society*, 132(33), pp. 11642-11648.

Liu, H., Li, Z., Sun, Y., Geng, X., Hu, Y., Meng, H., Ge, J. and Qu, L., 2018. Synthesis of luminescent carbon dots with ultrahigh quantum yield and inherent folate receptor-positive cancer cell targetability. *Scientific Reports*, 8(1), pp. 1086.

Liu, J., Zhang, T., Wang, Z., Dawson, G. and Chen, W., 2011. Simple pyrolysis of urea into graphitic carbon nitride with recyclable adsorption and photocatalytic activity. *Journal of Materials Chemistry*, 21(38), pp. 14398-14401.

Liu, Q., Chen, T., Guo, Y., Zhang, Z. and Fang, X., 2016. Ultrathin g-C_3N_4 nanosheets coupled with carbon nanodots as 2D/0D composites for efficient photocatalytic H_2 evolution. *Applied Catalysis B: Environmental*, 193, pp. 248-258.

Liu, S., Sun, H., O'Donnell, K., Ang, H., Tade, M. and Wang, S., 2016. Metal-free melem/g-C_3N_4 hybrid photocatalysts for water treatment. *Journal of Colloid and Interface Science*, 464, pp. 10-17.

Liu, S., Tian, J., Wang, L., Zhang, Y., Qin, X., Luo, Y., Asiri, A.M., Al‐Youbi, A.O. and Sun, X., 2012. Hydrothermal treatment of grass: a low-cost, green route to nitrogen-doped, carbon-rich, photoluminescent polymer nanodots as an effective fluorescent sensing platform for label-free detection of Cu (II) ions. *Advanced Materials*, 24(15), pp. 2037-2041.

Lu, J., Yang, J.X., Wang, J., Lim, A., Wang, S. and Loh, K.P., 2009. One-pot synthesis of fluorescent carbon nanoribbons, nanoparticles, and graphene by the exfoliation of graphite in ionic liquids. *ACS Nano*, 3(8), pp. 2367-2375.

Lu, W., Xu, T., Wang, Y., Hu, H., Li, N., Jiang, X. and Chen, W., 2016. Synergistic photocatalytic properties and mechanism of g-C_3N_4 coupled with zinc phthalocyanine catalyst under visible light irradiation. *Applied Catalysis B: Environmental*, 180, pp. 20-28.

Lü, X., Shen, J., Wu, Z., Wang, J. and Xie, J., 2014. Deposition of Ag nanoparticles on g-C_3N_4 nanosheet by N, N-dimethylformamide: soft synthesis and enhanced photocatalytic activity. *Journal of Materials Research*, 29(18), pp. 2170-2178.

Lu, Z., Song, W., Ouyang, C., Wang, H., Zeng, D. and Xie, C., 2017. Enhanced visible-light photocatalytic performance of highly-dispersed Pt/g-C_3N_4 nanocomposites by one-step solvothermal treatment. *RSC Advances*, 7(53), pp. 33552-33557.

Maeda, K., Wang, X., Nishihara, Y., Lu, D., Antonietti, M. and Domen, K., 2009. Photocatalytic activities of graphitic carbon nitride powder for water reduction and oxidation under visible light. *The Journal of Physical Chemistry C*, 113(12), pp. 4940-4947.

Maier, S.A., 2007. *Plasmonics: fundamentals and applications*. Springer Science & Business Media.

Malekshoar, G., 2016. *Enhanced solar photocatalytic hydrogen generation and water treatment using heteroStructure photocatalysts.* PhD thesis, The University of Western Ontario, Canada.

Malekzad, H., Zangabad, P.S., Mohammadi, H., Sadroddini, M., Jafari, Z., Mahlooji, N., Abbaspour, S., Gholami, S., Ghanbarpoor, M., Pashazadeh, R. and Beyzavi, A., 2018. Noble metal nanostructures in optical biosensors: basics, and their introduction to anti-doping detection. *TrAC Trends in Analytical Chemistry*. 100, pp. 116-135.

Maloney, F.S., Poudyal, U., Chen, W. and Wang, W., 2016. Influence of quantum dot concentration on carrier transport in ZnO:TiO_2 nano-hybrid photoanodes for quantum dot-sensitized solar cells. *Nanomaterials*, 6(11), pp. 191.

Mamba, G. and Mishra, A.K., 2016. Graphitic carbon nitride (g-C_3N_4) nanocomposites: a new and exciting generation of visible light driven photocatalysts for environmental pollution remediation. *Applied Catalysis B: Environmental*, 198, pp. 347-377.

Mehta, V.N., Jha, S., Basu, H., Singhal, R.K. and Kailasa, S.K., 2015. One-step hydrothermal approach to fabricate carbon dots from apple juice for imaging of mycobacterium and fungal cells. *Sensors and Actuators B: Chemical*, 213, pp. 434-443.

Meng, Y., Shen, J., Chen, D. and Xin, G., 2011. Photodegradation performance of methylene blue aqueous solution on Ag/g-C_3N_4 catalyst. *Rare Metals*, 30(1), pp. 276-279.

Mohapatra, S.K., Kondamudi, N., Banerjee, S. and Misra, M., 2008. Functionalization of self-organized TiO_2 nanotubes with Pd nanoparticles for photocatalytic decomposition of dyes under solar light illumination. *Langmuir*, 24(19), pp. 11276-11281.

Murdoch, M., Waterhouse, G.I.N., Nadeem, M.A., Metson, J.B., Keane, M.A., Howe, R.F., Llorca, J. and Idriss, H., 2011. The effect of gold loading and particle size on photocatalytic hydrogen production from ethanol over Au/TiO_2 nanoparticles. *Nature Chemistry*, 3(6), pp. 489-492.

Ni, Z., Dong, F., Huang, H. and Zhang, Y., 2016. New insights into how Pd nanoparticles influence the photocatalytic oxidation and reduction ability of g-C_3N_4 nanosheets. *Catalysis Science and Technology*, 6(16), pp. 6448-6458.

Ong, W.J., Tan, L.L., Chai, S.P. and Yong, S.T., 2015. Heterojunction engineering of graphitic carbon nitride (g-C_3N_4) via Pt loading with improved daylight-induced photocatalytic reduction of carbon dioxide to methane. *Dalton Transactions*, 44(3), pp. 1249-1257.

Ong, W.J., Tan, L.L., Ng, Y.H., Yong, S.T. and Chai, S.P., 2016. Graphitic carbon nitride (g-C_3N_4)-based photocatalysts for artificial photosynthesis and environmental remediation: are we a step closer to achieving sustainability? *Chemical Reviews*, 116(12), pp. 7159-7329.

Oza, G., Oza, K., Pandey, S., Shinde, S., Mewada, A., Thakur, M., Sharon, M. and Sharon, M., 2015. A green route towards highly photoluminescent and cytocompatible carbon dot synthesis and its separation using sucrose density gradient centrifugation. *Journal of Fluorescence*, 25(1), pp. 9-14.

Park, S.Y., Lee, C.Y., An, H.R., Kim, H., Lee, Y.C., Park, E.C., Chun, H.S., Yang, H.Y., Choi, S.H., Kim, H.S. and Kang, K.S., 2017. Advanced carbon dots via plasma-induced surface functionalization for fluorescent and bio-medical applications. *Nanoscale*, 9(26), pp. 9210-9217.

Patnaik, S., Sahoo, D.P. and Parida, K., 2018. An overview on Ag modified g-C_3N_4 based nanostructured materials for energy and environmental applications. *Renewable and Sustainable Energy Reviews*, 82, pp. 1297-1312.

Pawar, R., Kang, S., Lee, C. and Ahn, S., 2015a. Gold nanoparticle modified graphitic carbon nitride/multi-walled carbon nanotube (g-C_3N_4/CNTs/Au) hybrid photocatalysts for effective water splitting and degradation. *RSC Advances*, 5(31), pp. 24281-24292.

Pawar, R.C., Pyo, Y., Ahn, S.H. and Lee, C.S., 2015b. Photoelectrochemical properties and photodegradation of organic pollutants using hematite hybrids modified by gold nanoparticles and graphitic carbon nitride. *Applied Catalysis B: Environmental*, 176, pp. 654-666.

Peng, D., Wang, H., Yu, K., Chang, Y., Ma, X. and Dong, S., 2016. Photochemical preparation of the ternary composite CdS/Au/g-C_3N_4 with enhanced visible light photocatalytic performance and its microstructure. *RSC Advances*, 6(81), pp. 77760-77767.

Peng, S., McMahon, J.M., Schatz, G.C., Gray, S.K. and Sun, Y., 2010. Reversing the size-dependence of surface plasmon resonances. *Proceedings of the National Academy of Sciences*, 107(33), pp. 14530-14534.

Prasannan, A. and Imae, T., 2013. One-pot synthesis of fluorescent carbon dots from orange waste peels. *Industrial and Engineering Chemistry Research*, 52(44), pp. 15673-15678.

Qian, X., Yue, D., Tian, Z., Reng, M., Zhu, Y., Kan, M., Zhang, T. and Zhao, Y., 2016. Carbon quantum dots decorated Bi_2WO_6 nanocomposite with enhanced photocatalytic oxidation activity for VOCs. *Applied Catalysis B: Environmental*, 193, pp. 16-21.

Qin, J., Huo, J., Zhang, P., Zeng, J., Wang, T. and Zeng, H., 2016. Improving the photocatalytic hydrogen production of Ag/g-C_3N_4 nanocomposites by dye-sensitization under visible light irradiation. *Nanoscale*, 8(4), pp. 2249-2259.

Qu, D., Zheng, M., Zhang, L., Zhao, H., Xie, Z., Jing, X., Haddad, R.E., Fan, H. and Sun, Z., 2014. Formation mechanism and optimization of highly luminescent N-doped graphene quantum dots. *Scientific Reports*, 4, pp. 5294.

Rosenfeldt, E.J. and Linden, K.G., 2004. Degradation of endocrine disrupting chemicals bisphenol A, ethinyl estradiol, and estradiol during UV photolysis and advanced oxidation processes. *Environmental Science and Technology*, 38(20), pp. 5476-5483.

Roy, P., Chen, P.C., Periasamy, A.P., Chen, Y.N. and Chang, H.T., 2015. Photoluminescent carbon nanodots: synthesis, physicochemical properties and analytical applications. *Materials Today*, 18(8), pp. 447-458.

Sabhi, S. and Kiwi, J., 2001. Degradation of 2,4-dichlorophenol by immobilized iron catalysts. *Water Research*, 35(8), pp. 1994-2002.

Sachdev, A. and Gopinath, P., 2015. Green synthesis of multifunctional carbon dots from coriander leaves and their potential application as antioxidants, sensors and bioimaging agents. *Analyst*, 140(12), pp. 4260-4269.

Sahu, S., Behera, B., Maiti, T.K. and Mohapatra, S., 2012. Simple one-step synthesis of highly luminescent carbon dots from orange juice: application as excellent bio-imaging agents. *Chemical Communications*, 48(70), pp. 8835-8837.

Samanta, S., Martha, S. and Parida, K., 2014. Facile synthesis of Au/g-C_3N_4 nanocomposites: an inorganic/organic hybrid plasmonic photocatalyst with enhanced hydrogen gas evolution under visible-light irradiation. *Chemical Catalysis Catalytical Chemistry*, 6(5), pp. 1453-1462.

Schaber, P.M., Colson, J., Higgins, S., Thielen, D., Anspach, B. and Brauer, J., 2004. Thermal decomposition (pyrolysis) of urea in an open reaction vessel. *Thermochimica Acta*, 424(1-2), pp. 131-142.

Sim, L.C., Wong, J.L., Hak, C.H., Tai, J.Y., Leong, K.H. and Saravanan, P., 2018. Sugarcane juice derived carbon dot–graphitic carbon nitride composites for bisphenol A degradation under sunlight irradiation. *Beilstein Journal of Nanotechnology*, 9(1), pp. 353-363.

Sin, J.C., Lam, S.M., Mohamed, A.R. and Lee, K.T., 2012. Degrading endocrine disrupting chemicals from wastewater by TiO_2 photocatalysis: a review. *International Journal of Photoenergy*, pp. 1-23.

Snyder, S.A., Westerhoff, P., Yoon, Y. and Sedlak, D.L., 2003. Pharmaceuticals, personal care products, and endocrine disruptors in water: implications for the water industry. *Environmental Engineering Science*, 20(5), pp. 449-469.

Song, S.H., Jang, M., Yoon, H., Cho, Y.H., Jeon, S. and Kim, B.H., 2016. Size and pH dependent photoluminescence of graphene quantum dots with low oxygen content. *RSC Advances*, 6(100), pp. 97990-97994.

Soto, A.M. and Sonnenschein, C., 2010. Environmental causes of cancer: endocrine disruptors as carcinogens. *Nature Reviews Endocrinology*, 6(7), pp. 363.

Stan, C.S., Albu, C., Coroaba, A., Popa, M. and Sutiman, D., 2015. One step synthesis of fluorescent carbon dots through pyrolysis of N-hydroxysuccinimide. *Journal of Materials Chemistry C*, 3(4), pp. 789-795.

Su, X., Vinu, A., Aldeyab, S.S. and Zhong, L., 2015. Highly uniform Pd nanoparticles supported on g-C_3N_4 for efficiently catalytic suzuki–miyaura reactions. *Catalysis Letters*, 145(7), pp. 1388-1395.

Sun, L., Chen, P. and Lin, L., 2016. Enhanced molecular spectroscopy via localized surface plasmon resonance. In *Applications of Molecular Spectroscopy to Current Research in the Chemical and Biological Sciences*. InTech.

Sun, Y.P., Zhou, B., Lin, Y., Wang, W., Fernando, K.S., Pathak, P., Meziani, M.J., Harruff, B.A., Wang, X., Wang, H. and Luo, P.G., 2006. Quantum-sized carbon dots for bright and colorful photoluminescence. *Journal of the American Chemical Society,* 128(24), pp. 7756–7757.

Sun, Y., Ha, W., Chen, J., Qi, H. and Shi, Y., 2016. Advances and applications of graphitic carbon nitride as sorbent in analytical chemistry for sample pretreatment: a review. *Trends in Analytical Chemistry*, 84, Part A, pp. 12-21.

Thambiraj, S. and Shankaran, R., 2016. Green synthesis of highly fluorescent carbon quantum dots from sugarcane bagasse pulp. *Applied Surface Science*, 390, pp. 435-443.

Tonda, S., Kumar, S. and Shanker, V., 2016. Surface plasmon resonance-induced photocatalysis by Au nanoparticles decorated mesoporous g-C_3N_4 nanosheets under direct sunlight irradiation. *Materials Research Bulletin*, 75, pp. 51-58.

Tyagi, A., Tripathi, K.M., Singh, N., Choudhary, S. and Gupta, R.K., 2016. Green synthesis of carbon quantum dots from lemon peel waste: applications in sensing and photocatalysis. *RSC Advances*, 6(76), pp. 72423-72432.

Villamagna, A.M. and Murphy, B.R., 2010. Ecological and socio-economic impacts of invasive water hyacinth (Eichhornia crassipes): a review. *Freshwater Biology*, 55(2), pp. 282-298.

Wang, F., Chen, P., Feng, Y., Xie, Z., Liu, Y., Su, Y., Zhang, Q., Wang, Y., Yao, K., Lv, W. and Liu, G., 2017. Facile synthesis of N-doped carbon dots/g-C_3N_4 photocatalyst with enhanced visible-light photocatalytic activity for the degradation of indomethacin. *Applied Catalysis B: Environmental*, 207, pp. 103-113.

Wang, J. and Chu, L., 2016. Irradiation treatment of pharmaceutical and personal care products (PPCPs) in water and wastewater: an overview. *Radiation Physics and Chemistry*, 125, pp. 56-64.

Wang, J., Tang, L., Zeng, G., Deng, Y., Dong, H., Liu, Y., Wang, L., Peng, B., Zhang, C. and Chen, F., 2018. 0D/2D interface engineering of carbon quantum dots modified Bi_2WO_6 ultrathin nanosheets with enhanced photoactivity for full spectrum light utilization and mechanism insight. *Applied Catalysis B: Environmental*, 222, pp. 115-123.

Wang, J.L. and Xu, L.J., 2012. Advanced oxidation processes for wastewater treatment: formation of hydroxyl radical and application. *Critical Reviews in Environmental Science and Technology*, 42(3), pp. 251-325.

Wang, Q., Liu, X., Zhang, L. and Lv, Y., 2012. Microwave-assisted synthesis of carbon nanodots through an eggshell membrane and their fluorescent application. *Analyst*, 137(22), pp. 5392-5397.

Wang, X., Cheng, J., Yu, H. and Yu, J., 2017. A facile hydrothermal synthesis of carbon dots modified g-C_3N_4 for enhanced photocatalytic H_2-evolution performance. *Dalton Transactions*, 46(19), pp. 6417-6424.

Wang, Y., Wang, Q., Zhan, X., Wang, F., Safdar, M. and He, J., 2013. Visible light driven type II heterostructures and their enhanced photocatalysis properties: a review. *Nanoscale*, 5(18), pp. 8326-8339.

Wen, X., Yu, P., Toh, Y.R., Ma, X. and Tang, J., 2014. On the upconversion fluorescence in carbon nanodots and graphene quantum dots. *Chemical Communications*, 50(36), pp. 4703-4706.

Willets, K.A. and Van Duyne, R.P., 2007. Localized surface plasmon resonance spectroscopy and sensing. *Annual Review of Physical Chemistry*, 58, pp. 267-297.

Xia, J., Di, J., Yin, S., Li, H., Xu, H., Xu, L., Shu, H. and He, M., 2014. Solvothermal synthesis and enhanced visible-light photocatalytic decontamination of bisphenol A (BPA) by g-C_3N_4/BiOBr heterojunctions. *Materials Science in Semiconductor Processing*, 24, pp. 96-103.

Xiao, X., Wei, J., Yang, Y., Xiong, R., Pan, C. and Shi, J., 2016. Photoreactivity and mechanism of g-C_3N_4 and Ag Co-modified Bi_2WO_6 microsphere under visible light irradiation. *ACS Sustainable Chemistry and Engineering*, 4(6), pp. 3017-3023.

Xie, L., Ai, Z., Zhang, M., Sun, R. and Zhao, W., 2016. Enhanced hydrogen evolution in the presence of plasmonic Au-photo-sensitized g-C_3N_4 with an extended absorption spectrum from 460 to 640 nm. *PloS one*, 11(8), pp. e0161397.

Xu, H., Yang, X., Li, G., Zhao, C. and Liao, X., 2015. Green synthesis of fluorescent carbon dots for selective detection of tartrazine in food samples. *Journal of Agricultural and Food Chemistry*, 63(30), pp. 6707-6714.

Xu, J., Li, Y., Peng, S., Lu, G. and Li, S., 2013. Eosin Y-sensitized graphitic carbon nitride fabricated by heating urea for visible light photocatalytic hydrogen evolution: the effect of the pyrolysis temperature of urea. *Physical Chemistry Chemical Physics*, 15(20), pp. 7657-7665.

Xu, X., Ray, R., Gu, Y., Ploehn, H.J., Gearheart, L., Raker, K. and Scrivens, W.A., 2004. Electrophoretic analysis and purification of fluorescent single-walled carbon nanotube fragments. *Journal of the American Chemical Society*, 126(40), pp. 12736-12737.

Xue, J., Ma, S., Zhou, Y. and Wang, Q., 2015a. Au-loaded porous graphitic C_3N_4/graphene layered composite as a ternary plasmonic photocatalyst and its visible-light photocatalytic performance. *RSC Advances*, 5(107), pp. 88249-88257.

Xue, J., Ma, S., Zhou, Y., Zhang, Z. and He, M., 2015b. Facile photochemical synthesis of Au/Pt/g-C_3N_4 with plasmon-enhanced photocatalytic activity for antibiotic degradation. *ACS Applied Materials and Interfaces*, 7(18), pp. 9630-9637.

Yan, H., Chen, Y. and Xu, S., 2012. Synthesis of graphitic carbon nitride by directly heating sulfuric acid treated melamine for enhanced photocatalytic H_2 production from water under visible light. *International Journal of Hydrogen Energy*, 37(1), pp. 125-133.

Yan, S.C., Li, Z.S. and Zou, Z.G., 2009. Photodegradation performance of g-C_3N_4 fabricated by directly heating melamine. *Langmuir*, 25(17), pp. 10397-10401.

Yan, Z., Shu, J., Yu, Y., Zhang, Z., Liu, Z. and Chen, J., 2015. Preparation of carbon quantum dots based on starch and their spectral properties. Luminescence, 30(4), pp. 388-392.

Yang, Y., Guo, Y., Liu, F., Yuan, X., Guo, Y., Zhang, S., Guo, W. and Huo, M., 2013. Preparation and enhanced visible-light photocatalytic activity of silver deposited graphitic carbon nitride plasmonic photocatalyst. *Applied Catalysis B: Environmental*, 142, pp. 828-837.

Yao, S., Hu, Y. and Li, G., 2014. A one-step sonoelectrochemical preparation method of pure blue fluorescent carbon nanoparticles under a high intensity electric field. *Carbon*, 66, pp. 77–83.

Yeung, B.H., Wan, H.T., Law, A.Y. and Wong, C.K., 2011. Endocrine disrupting chemicals: Multiple effects on testicular signaling and spermatogenesis. *Spermatogenesis*, 1(3), pp. 231-239.

Yu, J., Wang, K., Xiao, W. and Cheng, B., 2014. Photocatalytic reduction of CO_2 into hydrocarbon solar fuels over g-C_3N_4–Pt nanocomposite photocatalysts. *Physical Chemistry Chemical Physics*, 16(23), pp. 11492-11501.

Yu, X., Liu, J., Yu, Y., Zuo, S. and Li, B., 2014. Preparation and visible light photocatalytic activity of carbon quantum dots/TiO_2 nanosheet composites. *Carbon*, 68, pp. 718-724.

Yuan, B., Wei, J., Hu, T., Yao, H., Jiang, Z., Fang, Z. and Chu, Z., 2015. Simple synthesis of g-C_3N_4/rGO hybrid catalyst for the photocatalytic degradation of rhodamine B. *Chinese Journal of Catalysis*, 36(7), pp. 1009-1016.

Zeng, Z., Li, K., Wei, K., Dai, Y., Yan, L., Guo, H. and Luo, X., 2017. Fabrication of highly dispersed platinum-deposited porous g-C_3N_4 by a simple in situ photoreduction strategy and their excellent visible light photocatalytic activity toward aqueous 4-fluorophenol degradation. *Chinese Journal of Catalysis*, 38(1), pp. 29-38.

Zhang, G., Ji, Q., Wu, Z., Wang, G., Liu, H., Qu, J. and Li, J., 2018. Facile “spot-heating” synthesis of carbon dots/carbon nitride for solar hydrogen evolution synchronously with contaminant decomposition. *Advanced Functional Materials*, 28(14), pp. 1706462.

Zhang, G., Zhang, J., Zhang, M. and Wang, X., 2012. Polycondensation of thiourea into carbon nitride semiconductors as visible light photocatalysts. *Journal of Materials Chemistry*, 22(16), pp. 8083-8091.

Zhang, H., Zhao, L., Geng, F., Guo, L.H., Wan, B. and Yang, Y., 2016. Carbon dots decorated graphitic carbon nitride as an efficient metal-free photocatalyst for phenol degradation. *Applied Catalysis B: Environmental*, 180, pp. 656-662.

Zhang, L., Tse, M.S. and Tan, O.K., 2014. Facile in situ synthesis of visible light-active Pt/C−TiO_2 nanoparticles for environmental remediation. *Journal of Environmental Chemical Engineering*, *2*(2), pp. 1214-1220.

Zhang, S., Sun, X., Ma, X., Chen, J., Lei, Y. and Wu, Y., 2016, October. Fluorescent carbon nanoparticles for sensitive and selective detection of palladium (Pd^{2+}). In *SENSORS, 2016*, IEEE, pp. 1-3.

Zhang, W., Zhou, L. and Deng, H., 2016. Ag modified g-C_3N_4 composites with enhanced visible-light photocatalytic activity for diclofenac degradation. *Journal of Molecular Catalysis A: Chemical*, 423, pp. 270-276.

Zhang, Z., Sun, W. and Wu, P., 2015. Highly photoluminescent carbon dots derived from egg white: facile and green synthesis, photoluminescence properties, and multiple applications. *ACS Sustainable Chemistry and Engineering*, 3(7), pp. 1412-1418.

Zhao, W., Xie, L., Zhang, M., Ai, Z., Xi, H., Li, Y., Shi, Q. and Chen, J., 2016. Enhanced photocatalytic activity of all-solid-state g-C_3N_4/Au/P25 Z-scheme system for visible-light-driven H_2 evolution. *International Journal of Hydrogen Energy*, 41, pp. 6277-6287.

Zhou, S., Liu, Y., Li, J., Wang, Y., Jiang, G., Zhao, Z., Wang, D., Duan, A., Liu, J. and Wei, Y., 2014. Facile in situ synthesis of graphitic carbon nitride (g-C_3N_4)-N-TiO_2 heterojunction as an efficient photocatalyst for the selective photoreduction of CO_2 to CO. *Applied Catalysis B: Environmental*, 158, pp. 20-29.

Zhu, C., Zhai, J. and Dong, S., 2012. Bifunctional fluorescent carbon nanodots: green synthesis via soy milk and application as metal-free electrocatalysts for oxygen reduction. *Chemical Communications*, 48(75), pp. 9367-9369.

Zhu, S., Meng, Q., Wang, L., Zhang, J., Song, Y., Jin, H., Zhang, K., Sun, H., Wang, H. and Yang, B., 2013. Highly photoluminescent carbon dots for multicolor patterning, sensors, and bioimaging. *Angewandte Chemie*, 125(14), pp. 4045-4049.

Zhuo, Y., Miao, H., Zhong, D., Zhu, S. and Yang, X., 2015. One-step synthesis of high quantum-yield and excitation-independent emission carbon dots for cell imaging. *Materials Letters*, 139, pp. 197–200.

LIST OF PUBLICATIONS BASED ON THIS RESEARCH WORK

In Refereed International Journals:

1. Hak CH, Sim LC, Leong KH, Lim PF, Chin YH, Saravanan P (2018) M/g-C_3N_4 (M= Ag, Au, and Pd) composite: synthesis via sunlight photodeposition and application towards the degradation of bisphenol A. *Environ Sci Pollut Res* 1-12. (Impact factor: 2.800).